

A Dynamical Nephrovascular Model of Renal Autoregulation

by

Ioannis Sgouralis

Department of Mathematics
Duke University

Date: _____

Approved:

Anita T. Layton, Supervisor

Frederik H. Nijhout

Stephanos Venakides

Thomas P. Witelski

Dissertation submitted in partial fulfillment of the requirements for the degree of
Doctor of Philosophy in the Department of Mathematics
in the Graduate School of Duke University
2014

ABSTRACT

A Dynamical Nephrovascular Model of Renal Autoregulation

by

Ioannis Sgouralis

Department of Mathematics
Duke University

Date: _____

Approved:

Anita T. Layton, Supervisor

Frederik H. Nijhout

Stephanos Venakides

Thomas P. Witelski

An abstract of a dissertation submitted in partial fulfillment of the requirements for
the degree of Doctor of Philosophy in the Department of Mathematics
in the Graduate School of Duke University
2014

Copyright © 2014 by Ioannis Sgouralis
All rights reserved except the rights granted by the
Creative Commons Attribution-Noncommercial Licence

Abstract

The main functions of the kidney take place in the nephrons. For their proper operation, nephrons need to be supplied with a stable blood flow that remains constant despite fluctuations of arterial pressure. Such stability is provided by the afferent arterioles, which are unique vessels in the kidney capable of adjusting diameter. By doing so, afferent arterioles regulate blood delivery downstream, where the nephrons are located. The afferent arterioles respond to signals initiated by two mechanisms: the myogenic response which operates to absorb pressure perturbations within the vasculature, and tubuloglomerular feedback which operates to stabilize salt reabsorption.

In this thesis, a mathematical model of the renal nephrovasculature that represents both mechanisms in a dynamical context is developed. For this purpose, detailed representations of the myogenic mechanism of vascular smooth muscles and the tubular processes are developed and combined in a single comprehensive model. The resulting model is formulated with a large number of ordinary differential equations that represent the intracellular processes of arteriolar smooth muscles, coupled with a number of partial differential equations, mainly of the advection–diffusion–reaction type, that represent blood flow, glomerular filtration and the tubular processes. Due to its unique activation characteristics, the myogenic response is formulated with a set of delay differential equations.

The model is utilized to assess a variety of physiological phenomena: the con-

duction of vasomotor responses along the afferent arteriole, autoregulation under physiologic as well as pathophysiologic conditions, and renal oxygenation. A first attempt to model the impact of diabetes mellitus on renal hemodynamics is also made. Further, an application with clinical significance is presented. Namely, renal oxygenation is estimated under conditions that simulate those observed during cardiopulmonary surgery. Results indicate the development of renal hypoxia, which suggests an important pathway for the development of acute kidney injury.

στη μνήμη του Αδάμου

Contents

Abstract	iv
List of Tables	xii
List of Figures	xiii
List of Abbreviations and Symbols	xv
Acknowledgements	xvi
Introduction	1
1 Introduction to Mathematical Modeling of Renal Physiology	6
1.1 Renal physiology	6
1.1.1 The nephron	7
1.1.2 Autoregulation	8
1.1.3 The afferent arteriole	9
1.1.4 Vascular smooth muscles	10
1.2 A modeling framework of smooth muscle myogenic mechanism	12
1.2.1 Membrane electrophysiology	13
1.2.2 Free cytosolic calcium regulation	15
1.2.3 Cross-bridge cycling	16
1.2.4 Muscle mechanics	17
1.2.5 Discussion	18

2	Autoregulation and Conduction of Vasomotor Responses	20
2.1	Introduction	20
2.2	Mathematical model	21
2.2.1	Multi-cell afferent arteriole model	21
2.2.2	Luminal fluid model	26
2.3	Results	27
2.3.1	Autoregulatory response of the model vessel	27
2.3.2	Responses to a step perturbation	28
2.3.3	Responses to sinusoidal oscillations in inflow pressure	30
2.3.4	Asymmetric upstream and downstream propagation	32
2.3.5	Parameter sensitivity studies	38
2.4	Discussion	39
2.4.1	Conduction of vasomotor response	40
2.4.2	Comparison with previous models	42
2.4.3	Model limitations and future extensions	44
2.5	Appendix: Model equations and parameters	45
2.5.1	Ion transport and membrane potential	45
2.5.2	Myosin phosphorylation	47
2.5.3	Vessel mechanics	48
2.5.4	Parameters	50
3	Control and Modulation of Fluid Flow	53
3.1	Introduction	53
3.2	Mathematical Model	55
3.2.1	Afferent arteriole submodel	55
3.2.2	Glomerular filtration submodel	61

3.2.3	Renal tubule submodel	62
3.2.4	Parameters and numerical method	64
3.3	Results	66
3.3.1	Base-case spatiotemporal behavior	66
3.3.2	Autoregulatory response to steady pressure perturbations	70
3.3.3	Response to step-pressure changes	72
3.3.4	Spectral response to sinusoidal pressure perturbations	74
3.3.5	Spectral response to sinusoidal electrical perturbations	80
3.4	Discussion	82
4	Assessment of Renal Autoregulation	86
4.1	Introduction	86
4.2	Mathematical model	87
4.2.1	Afferent arteriole submodel	88
4.2.2	Glomerulus submodel	93
4.2.3	Tubule submodel	94
4.2.4	Parameters	97
4.3	Results	98
4.3.1	Base-case predictions	98
4.3.2	Assessment of autoregulation	99
4.3.3	Response to rapid pressure increase	103
4.3.4	Rate-dependent response to pressure-ramp perturbations	106
4.3.5	Hemodynamics in diabetes	109
4.3.6	Sensitivity studies	112
4.4	Discussion	114
4.4.1	Comparison with previous modeling studies	119

4.4.2	Renal hemodynamics in diabetes mellitus	120
5	Assessment of Renal Oxygenation in Cardiopulmonary Bypass	124
5.1	Introduction	124
5.2	Methods	125
5.2.1	Representative nephrovascular unit	126
5.2.2	Renal oxygen transport	131
5.3	Results	135
5.3.1	Model validation	136
5.3.2	Assessment durring CPB	136
5.3.3	CPB oxygenation sensitivity studies	139
5.4	Discussion	141
5.4.1	Development of hypoxia	141
5.4.2	Model limitations	142
6	Conclusions and future directions	143
6.1	Conclusions	143
6.2	Future directions	144
6.2.1	Construction of nephrovascular network	145
6.2.2	Representation of modulating effects	145
6.2.3	Detailed representation of vascular blood flow	145
A	Complete set of smooth muscle model equations	147
A.1	Electrophysiology	147
A.2	Autoregulatory mechanisms	149
A.2.1	Myogenic response	149
A.2.2	Tubuloglomerular feedback	149
A.3	Cytosolic Ca ²⁺ regulation	150

A.4	Cross-bridge cycling	150
A.5	Muscle mechanics	150
A.6	Glossary and parameter values	151
A.6.1	Variables	151
A.6.2	Parameters	152
B	Complete set of nephrovascular model equations	154
B.1	Vasculature	154
B.1.1	Blood flow	155
B.1.2	Afferent arteriole	155
B.1.3	Efferent arteriole	156
B.1.4	Structural resistances and hematocrit dependence	157
B.2	Glomerulus	157
B.3	Nephron tubule	158
B.3.1	Tubular water transport	159
B.3.2	Tubular radius	160
B.3.3	Tubular pressure	160
B.3.4	Tubular Cl^- transport	161
B.4	Glossary and parameter values	162
B.4.1	Variables	162
B.4.2	Parameters	164
C	Complete set of temperature dependent equations	166
	Bibliography	168
	Biography	184

List of Tables

2.1	Vasoresponse propagation length constants (boundary conditions). . .	38
2.2	Vasoresponse propagation length constants (coupling constants). . . .	39
2.3	Afferent arteriole geometric dimensions.	51
2.4	Smooth muscle cell electrochemical parameters.	51
2.5	Arteriolar cell parameters.	51
2.6	Smooth muscle cell mechanical parameters (I).	52
2.7	Smooth muscle cell mechanical parameters (II).	52
3.1	Parameters defining the myogenic spline.	59
3.2	Model parameters.	66
3.3	Time-averaged base-case predictions.	67
4.1	Autoregulatory current parameters.	121
4.2	Model parameters.	122
4.3	Muscle mechanics parameters.	122
4.4	Tubular parameter profiles.	123
4.5	Baseline results obtained for steady perfusion pressure 100 mmHg. . .	123
5.1	Oxygen delivery parameter values.	134
5.2	Parameter values for the simulated CPB scenarios.	136
5.3	Comparison of normothermic and hypothermic scenarios.	136
5.4	Comparison of model predictions with experimental data.	137
5.5	Summary of renal function durring CPB.	137

List of Figures

1.1	Schematic representation on smooth muscle myogenic mechanism. . .	13
1.2	Smooth muscle membrane equivalent electrical circuit.	15
1.3	Model smooth muscle geometry and mechanics.	17
1.4	Smooth muscle dynamics.	18
1.5	Smooth muscle response to steady myogenic current.	19
2.1	Schematic representation of model afferent arteriole.	22
2.2	Luminal diameter and pressure with or without myogenic response. .	27
2.3	Model responses to a step increase or decrease in AA inflow pressure.	29
2.4	Oscillations of diameter and pressure under sinusoidal perturbation. .	31
2.5	Model responses to an electrical stimulation.	33
2.6	Vasoconstrictive response induced by electrical stimulation.	35
2.7	Luminal diameters at various transmural pressures.	36
3.1	Schematic diagram of the model nephron.	56
3.2	Base-case temporal predictions.	68
3.3	Spatial profiles of solution.	69
3.4	Autoregulatory responses to sustained steady pressure perturbations.	71
3.5	Model responses to step-pressure changes.	73
3.6	Proximal tubule pressure responses to pressure perturbations.	75
3.7	Contour of power spectral density of proximal tubule pressure.	77
3.8	Proximal tubule pressure with myogenic response disabled.	78

3.9	Oscillations at selected locations driven by external forcing.	79
3.10	Proximal tubule pressure responses to electrical perturbations.	85
4.1	Schematic diagram of the combined nephrovascular model.	87
4.2	Autoregulatory currents.	97
4.3	Baseline spatial profiles of parameters and steady-state solution.	98
4.4	Time-course of baseline solution at selected locations.	100
4.5	Base-case spatial profiles of solution.	101
4.6	Time-averaged SNGFR and vascular resistance.	102
4.7	Pressure profiles for selected perfusion pressures.	103
4.8	Model response to pressure up-step.	105
4.9	Model response to slow and fast pressure ramps.	107
4.10	Autoregulatory responses to slow and fast pressure ramps.	108
4.11	Glomerular hyperfiltration in diabetes.	109
4.12	Autoregulatory plateaus of simulated diabetes.	111
4.13	Normal and diabetic responses to rapid pressure fluctuations.	113
4.14	Sensitivity of autoregulation effectiveness to myogenic current.	115
4.15	Sensitivity of TGF autoregulation to pressure natriuresis response.	116
5.1	Single nephron autoregulatory plateaus for pulsatile flow.	126
5.2	Blood viscosity dependence on hematocrit.	128
5.3	Sodium reabsorption during CPB.	138
5.4	Oxygen delivery and consumption rates during CPB.	139
5.5	Renal oxygenation during CPB.	140
5.6	Renal oxygenation sensitivity during normothermic CPB.	141
B.1	Simplified representation of the combined model.	155

List of Abbreviations and Symbols

Abbreviations

AA	Afferent arteriole.
EA	Efferent arteriole.
GL	Glomerulus, or glomerular capillaries.
TB	Renal tubule.
MD	Macula densa.
LB	Loop bend.
SM	Smooth muscle.
MR	Myogenic response.
TGF	Tubuloglomerular feedback.
CPB	Cardiopulmonary bypass.

Symbols

P	Hydrostatic fluid pressure.
Q	Volumetric fluid flow rate.
R	Vascular or tubular luminal radius.
Ω	Vascular or tubular resistance.
C	Protein or Cl^- concentration.
x, y, z	Position along AA, GL, and TB, respectively.
t	Time.

Acknowledgements

I wish above all to thank my Ph.D. advisor Professor *Anita T. Layton*, who introduced me to physiological modeling, and continuously supported, encouraged, and motivated my work this way giving me the opportunity to fully develop my scientific potential.

I wish to thank my Ph.D. mentor Professor *Stephanos Venakides* for his academic and personal guidance through the early stages of my graduate life.

I wish to thank Professor *Roger Evans* of Monash University and Professor *Bruce Gardiner* of the University of Western Australia for drawing my attention to the area of renal oxygen transport and their generous assistance with the final part of my thesis work.

I thank *Robert Moss*, who has been always willing to go into long discussions concerning the modeling and experimental aspects of Renal Physiology.

I also owe special thanks to Professor *Will Cupples* of Simon Fraser University for his valuable insights and comments on my work throughout the last years.

Finally, I thank the American Physiological Society and Springer Publications for permitting the reproduction of previously published material included in this dissertation, which first appeared in the American Journal of Physiology and the Bulletin of Mathematical Biology.

This thesis would not have been possible without the financial aid of the National Institute of Health for which I am grateful.

Introduction

The mammalian kidneys function to remove from the body the metabolic waste and to maintain the balance of water and electrolytes. Through the regulation of body water combined with regulation of sodium, kidneys are involved in the control of blood volume, which provides an important controlling mechanism of blood pressure. Renal dysfunction is often associated with serious health issues such as diabetes and hypertension.

The main functions of the kidney are carried out by the nephrons. For their proper operation, nephrons need to be supplied with a stable blood flow that remains constant despite fluctuations of arterial pressure. Such stability is provided by the *afferent arterioles*, which are unique vessels in the renal microcirculation capable of adjusting diameter. By doing so, afferent arterioles regulate blood delivery downstream, where the nephrons are located.

The afferent arterioles respond to signals initiated by two mechanisms: the *myogenic response* which operates to absorb pressure perturbations within the pre-glomerular vasculature, and *tubuloglomerular feedback* which operates to stabilize salt reabsorption by the distal nephron. Both mechanisms function independently in each individual nephron but share the same afferent arteriole as a common effector. The different signals that activate these mechanisms give rise to complex interactions that may have synergistic or antagonistic effects.

Goal of this work is the development of a mathematical model of renal autoreg-

ulation that allows the assessment of renal hemodynamics under physiologic and pathophysiologic conditions. For this purpose, the necessary cellular, vascular, and nephronic processes have been represented to form a model afferent arteriole and renal tubule. In view of recent findings concerning the unique activation kinetics of the renal myogenic response [169, 13], which render it more sensitive to peak than mean pressure, the model have been formulated in a dynamical context that allows the accurate incorporation of such behavior.

The resulting model is characteristic of the mammalian nephrovascular units. Due to the availability of experimental measurements, the model is formulated for the rat kidney. In particular, the parameter values have been chosen to match the superficial nephrons found in the rat renal cortex.

The proposed model has been developed in a series of papers [145, 146, 147]. It is based on prior modeling work that concerns independently the operation of: (i) the intercellular myogenic mechanism of smooth muscles [60], (ii) the myogenic response of renal vascular smooth muscles [27], (iii) glomerular filtration [41], and (iv) renal tubule [90]. Specifically, the representation of the autoregulatory mechanisms have been influenced by the models of tubuloglomerular feedback and myogenic response developed in [94] and [106], respectively. The representation of the vascular mechanics of the arteriolar walls, utilized in the latter form of the developed model, have been adopted with modifications from [21, 3, 20].

The proposed nephrovascular model is currently the only available mathematical model of renal autoregulation that combines: (i) detailed representation of the myogenic mechanism of afferent arteriole vascular smooth muscles, (ii) myogenic response induced by steady and oscillatory pressure variations, (iii) tubuloglomerular feedback with realistic afferent arteriolar effector, (iv) glomerular filtration, and (v) detailed representation of tubular fluid flow and salt reabsorption.

The model represents the fundamental processes responsible for renal autoregula-

tion at the level of a single nephrovascular unit. The represented processes operate in the seconds-to-minutes time scale. Naturally, these requirements limits the model's applicability, which does not capture phenomena arising from the interaction of coupled nephrovascular units or the modulation caused by vasoactive factors such as the renin-angiotensin system, nitric oxide, the sympathetic nerve activity, and others.

To maintain the computational cost associated with the numerical solution of the model's equations in tractable level, certain modeling simplifications have been adopted. Among the most notable are: a simplified representation of luminal blood flow provided by the Hagen-Poiseuille equation, a simplified representation of cross-bridge cycling, an approximation of tubular sodium transport by Michaelis-Menten kinetics, and an simplified representation of the distal nephron.

A brief description of the chapters contained in the thesis is provided below.

- Chapter 1 describes the physiological background of renal autoregulation. Special attention is paid to the intercellular processes enabling smooth muscle contraction. Due to its importance on the subsequent chapters, a computational framework of the contractile mechanism of vascular smooth muscles is also presented.
- Chapter 2 presents the earliest form of the proposed nephrovascular model. The afferent arteriole is represented by a chain of coupled vascular smooth muscles. The form of the model presented at this point does not include either a glomerulus or a renal tubule, and therefore accounts only for autoregulation provided by the myogenic response alone. The main conclusions illuminate the origins of the asymmetric propagation of vasomotor responses that has been observed experimentally. Such propagation is speculated to influence whole kidney's activity. Its explicit role remains elusive.
- Chapter 3 extends the model by the addition of the glomerulus and the re-

nal tubule. Tubuloglomerular feedback is not represented at this stage. The focus of the chapter is on the transformation of pressure perturbations along the various segments of the renal nephrovasculature. The main conclusions of the chapter underline the role of heterodyning (i.e. the generation of new frequencies by the mixing of distinct oscillating waveforms) in increasing the spectral complexity in the low frequency range of the oscillations reaching the renal tubule. Such heterodyning is generated between the spontaneous electrical activity of the afferent arteriole vascular smooth muscles and external forcing.

- Chapter 4 extends the model of the previous chapter by the incorporation of tubuloglomerular feedback. Thus, a complete representation of the autoregulatory processes is achieved. With the resulting model the relative contributions of the autoregulatory mechanisms are investigated under a variety of physiologic and pathophysiologic conditions. The latter includes a first approach of modeling the impact of diabetes mellitus on the renal nephrovasculature and an estimation of its consequences on nephron's operation and glomerular protection.
- Chapter 5 utilizes the model developed in the previous chapter to assess the renal function under the conditions commonly found during cardiopulmonary bypass surgery. For this purpose, the effects of heart beat, hypotension, hemodilution, and hypothermia have been considered. The model is augmented with the representation of renal oxygenation. Results indicate the development of renal hypoxia, especially during the hypothermic and the rewarming phases of the surgery, which suggests an important pathway for the development of acute kidney injury, a prevalent clinical complication of such surgical procedures.

Parts of the computational framework described in Chapter 1 is adopted from

[27]. The work described in Chapters 2, 3, 4 has been previously presented in [145, 146, 147], respectively. Chapter 5 is comprised by work that firstly appears in this thesis.

Introduction to Mathematical Modeling of Renal Physiology

1.1 Renal physiology

The kidneys are parts of the urinary system of mammals. Their main function is to remove metabolic waste products from the bloodstream, and to maintain the balance of body water and electrolytes. Through the regulation of body water combined with regulation of sodium concentration, kidneys are involved in the control of blood volume, which provides an important controlling mechanism of blood pressure.

Viewed externally each mammalian kidney has a bean-shaped form. Its hilum is penetrated by the renal artery, the renal vein, a variety of nerves, and the ureter. Internally the kidney is separated in an outer and an inner region, the cortex and medulla, respectively [88, 87]. Both regions consist by nephrons, ducts, and vessels.

In the kidney's microcirculation, blood enters through the renal artery, divides successively into segmental arteries, interlobar arteries, arcuate arteries, and the interlobular arteries. Each interlobular artery branches off into a small number of afferent arterioles. In turn, each afferent arteriole delivers blood to a single glomerulus.

Inside the glomerulus, the entering blood divides in a large number of capillaries, and before exiting converges to a single efferent arteriole. Each efferent arteriole further divides to form either the peritubular capillaries or the vasa recta. Blood leaving the peritubular capillaries or the vasa recta rejoins to form successively venules, small veins, interlobular veins, arcuate veins, interlobar veins, and finally returns to systemic circulation through the renal vein [88, 127, 25, 9].

1.1.1 *The nephron*

The nephrons are the functional units of kidney. They are responsible for the filtration–secretion–reabsorption processes necessary for the production of urine. Anatomically, each nephron consists of two parts: the renal corpuscle, and the renal tubule.

The *renal corpuscle* is formed by the network of glomerular capillaries and the surrounding Bowman’s capsule. Blood plasma is filtered through the capillaries and collected in Bowman’s capsule from where it is delivered into the proximal part of renal tubule [159].

Beginning at the glomerulus, the *renal tubule* consists of the following successive segments: proximal tubule (which is further divided in the convolved and straight segments), loop of Henle (which is further divided in the descending and the ascending limbs), and the distal tubule. The distal tubule drains into the collecting duct, which is connected via a sequence of minor and major calyces to the bladder [88]. Each tubular part is associated with a different stage of the excretion–secretion proses of the urine formation which is not further discussed in this thesis.

The early distal tubule approaches its parent glomerulus and passes between the afferent and efferent arterioles forming the juxtaglomerular apparatus [9]. The juxtaglomerular apparatus consists of the terminal segment of the supplying afferent arteriole, the initial segment of the supplied efferent arterioles, and the macula densa cells which are part of the distal tubule’s wall.

Urine is formed in the renal tubule through the combination of the following processes: (i) *filtration* which is the production of a protein free solution similar to blood plasma that consists the first form of the tubular fluid, (ii) *secretion* which is the extrusion of materials from the cytosol of the cells forming the tubular wall and their addition to the tubular fluid, and (iii) *reabsorption* which is the removal of material from the tubular fluid to the surrounding interstitial fluid and then back to the bloodstream.

Filtration is solely held in the glomerulus, and provides the first stage of urine formation. During the stage of filtration, water and blood solutes pass through the glomerular capillaries to the space enclosed by Bowman's capsule where it is collected and delivered to the proximal tubule. The total volume of filtrate formed by the kidney per unit time defines the glomerular filtration rate (GFR). As in all capillary beds, GFR is determined by the hydrostatic blood pressure in the capillary lumen, the hydrostatic pressure in the surrounding space (Bowman's space), and the colloid osmotic pressure of the plasma proteins [159, 110, 41, 14, 15, 83, 4, 78].

1.1.2 Autoregulation

Normal nephron function requires GFR to remain within a narrow window despite changes in arterial pressure which is achieved by a variety of mechanisms. Mean arterial pressures in the range 80–180 mmHg define the autoregulatory range, where renal blood flow and GFR has been found to remain nearly constant [73, 82, 37, 148]. Further, besides stabilizing blood flow and GFR, renal autoregulation also includes mechanisms aiming to protect the glomerular capillaries from barotrauma caused by increased blood pressure [13, 169, 107, 105, 106].

Autoregulation is achieved by a variety of mechanisms acting in parallel that independently set the pre- and, in a slower time scale and lesser degree, the post-glomerular vascular resistances. The major such mechanisms are tubuloglomerular

feedback and the myogenic response [73, 82, 37].

Tubuloglomerular feedback operates through the sequence: Increased arterial pressure raises renal blood flow and glomerular capillary blood pressure. These changes cause GFR, and thus sodium delivery to the distal tubule, to rise. Increased distal delivery is sensed by the macula densa cells which activate mechanisms that increase pre- and decrease post-glomerular resistance by constricting and dilating the afferent and efferent arterioles respectively, therefore reducing blood flow, glomerular blood pressure, and GFR [73, 82, 37].

The *myogenic response* describes the observed contraction/dilation of smooth muscle cells in response to dilating/contracting loads. In the case of vascular smooth muscles, increased blood pressure induces vasoconstriction, which overcomes the passive dilation of the vascular wall and reduces the diameter below the one at lower pressure. This causes a rise in vascular resistance at higher pressure and allows for autoregulation of blood flow downstream. The myogenic response is observed in most vascular beds [21, 38], however it is particularly pronounced in the kidney [120, 73].

1.1.3 *The afferent arteriole*

The main role of the afferent arterioles is to supply the glomerulus with blood. As part of the renal vasculature, afferent arterioles are responsible for most of the blood flow regulation which achieve by dilating or constricting in response to signals initiated by the autoregulatory mechanisms [73, 82, 37].

Renal afferent arterioles, as most of the small arteries and arterioles found in the mammalian body, exhibit spontaneous rhythmic vasomotion [73, 24, 170, 34, 166]. The driving stimulus of vasomotion is believed to be oscillations of the same frequency intrinsically appearing on the electrical activity of the smooth muscles consisting the vascular walls [114].

In the myogenic response expressed by the afferent arterioles, hydrostatic blood

pressure is sensed possibly as stress generated by the pressure difference across the vascular wall, and triggers adjustments in lumen diameter that change vascular resistance and therefore affecting blood flow [82, 39]. In response to an increase/decrease in blood pressure, myogenic response operates in two phases: initially, a small passive increase/decrease in diameter is observed, which is followed by a significant decrease/increase in diameter until it reaches a stationary level [82, 39].

As most vascular segments, each afferent arteriole consists of an exterior layer of smooth muscle cells, and an interior layer of longitudinally oriented endothelial cells that come in direct contact with the bloodstream. Smooth muscles are long, approximately cylindrical, cells that surround the endothelium enclosing the vascular lumen in a spiral fashion [101]. The strength of the vascular wall is provided by the smooth muscles, which are myogenically active, in contrast with the endothelium which's role is secondary and restricted to the production of various vasomodulators like nitric oxide and others [82, 37].

1.1.4 *Vascular smooth muscles*

Vascular smooth muscles are responsible for the development of the myogenic tone of the vascular beds. The basic cellular characteristics of smooth muscles concerning its contractility are described below.

The *cell membrane* consists the physical boundary of the cell separating the cytoplasm from the interstitium. Forming a barrier to the passage of ions (most notably Ca^{2+} , K^+), cell membrane allows the muscle to maintain concentrations in its interior at different levels from those in the exterior. Cytoplasm consists of the cytosol which occupies about half the volume of the whole cell, and the various cytoplasmic organelles.

The concentration of free Ca^{2+} in the cytosol is the major determinant of smooth muscle contractility. The stress developed by the smooth muscle results from the in-

teractions of the myosin and actin proteins, according to the sequence: An increase in free Ca^{2+} results in the activation of myosin light chain kinase (MLCK) which phosphorylates the myosin light chains, resulting in an increase in myosin ATPase activity and, consequently the formation of cross-bridges. Muscle contraction results from the development of stress by the sliding of the actin over the myosin filaments, driven by the formed cross-bridges. On the other hand, a decrease in free calcium results in the inactivation of MLCK, which inactivates the myosin light chains, allowing the myosin phosphatase to dephosphorylate myosin which in turn leads in weakening of the developed stress, and therefore muscle relaxation [117, 39, 77].

During smooth muscle contraction, free Ca^{2+} increases as a result of influx from the surrounding interstitium or release from the sarcoplasmic reticulum. During relaxation, free Ca^{2+} decreases, which takes place by efflux from the cell membrane, or by uptake from the intercellular stores [48].

Influx of Ca^{2+} through the cell membrane occurs mainly via ion channels, and secondarily via exchangers. Both transporter systems do not require consumption of energy since ions move down the electrochemical gradient. Channel mediated influx occurs through Ca^{2+} selective channels or non-selective cation channels, that can be voltage sensitive or voltage insensitive.

The unequal concentrations of ions in the cytosol and the interstitium give rise to the development of electrical voltage difference across the cell membrane. The *membrane potential* is defined as the difference:

$$v_m = v_{int} - v_{ext}$$

where v_{int} and v_{ext} are the electrical potentials in the interior and exterior of the membrane. The common convention is the extracellular space to be grounded, so v_m equals v_{int} .

The maintenance of v_m involves the transport of ions across the membrane. The

ionic transport induces transmembrane electrical currents. The common convention is inward currents to amount for the entering of positive charged ions to the cell, which rises v_m causing depolarization, and outward currents to amount for the entering of negative charged ions to the cell, which lowers v_m causing hyperpolarization. The membrane potential at which the associated net ion flow is zero defines the resting potential.

The cell membrane itself is an insulator, so being surrounded on both sides by conducting fluid (cytoplasm and interstitium) endows it with capacitative properties. Smooth muscle membrane capacity is proportional to the cell membrane area, with proportionality constant $1 \mu\text{F}/\text{cm}^2$.

Local application of vasoconstrictors or vasodilators onto the surface of arterioles induces both local and conducted responses implying the existence of intercellular communication mechanisms [154, 115]. Intercellular communication is provided by *gap-junctions* which are non-selective ion channels developed between adjacent cells [17]. Their function is to form a direct connection of the cytosol of the cells allowing the free pass of ions and other substances among them. Gap-junctions are developed between similar cells (homo-cellular coupling), or between cells of different type (hetero-cellular coupling). In the renal afferent arteriole both types are found: smooth muscle–to–smooth muscle and smooth muscle–to–endothelium.

1.2 A modeling framework of smooth muscle myogenic mechanism

The myogenic mechanism of the smooth muscles that form the afferent arteriole walls is the fundamental component of every modeling approach presented in this thesis. Due to its importance, a brief description is given below. Aim of this section is to provide a comprehensive framework upon which the rest of the work is built. The described framework relies on the model developed in [27], which in turn is an extension of the model firstly developed in [60]. For a detailed presentation the

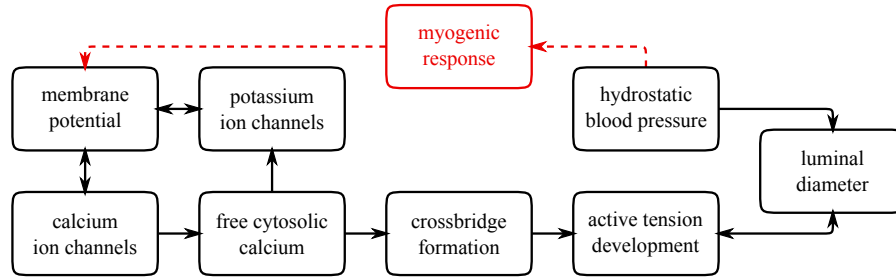


FIGURE 1.1: Schematic representation on smooth muscle myogenic mechanism.

reader is referred therein or to the subsequent chapters of the thesis.

The *model smooth muscle* combines submodels of membrane electrophysiology, cytosolic Ca^{2+} regulation, cross-bridges cycling, and wall mechanics. A schematic diagram of the represented intercellular processes is shown on figure 1.1.

Briefly, membrane potential controls the opening of Ca^{2+} membrane channels, that in turn determine the free cytosolic Ca^{2+} by controlling its influx. Cytosolic Ca^{2+} determines the formation of cross-bridges. Vascular radius is determined by the balance of tension developed actively by the muscle, which depends on the amount of formed cross-bridges, and the opposing tension developed by transmural pressure.

The model also represents the *myogenic response* which is incorporated based on the assumption that pressure changes induce the development of a transmembrane current (see below) with specific characteristics. In this section, any effort to model the asymmetric transient vasomotor responses is postponed for the subsequent chapters. To simplify the presentation, the current representing the myogenic response signal is assumed prescribed to time independent values only.

1.2.1 Membrane electrophysiology

The membrane model shares many similarities with the Morris-Lecar muscle model [123], which in turn is a simplified version of the Hodgkin-Huxley model [68] that was initially developed to describe the excitability of neuron cells.

The model membrane incorporates three types of ion currents: I_{Ca} due to influx of Ca^{2+} , I_K due to efflux of K^+ , I_L due to leak of other ions such as Na^+ , Cl^- , and an unspecified current I_{MR} that mediates the operation of the myogenic response. Specifically, I_{Ca} is v_m -gated, I_K is $[Ca^{2+}]$ - and v_m -gated, while I_L is non gated. The ion currents assume the ohmic forms:

$$I_{Ca} = g_{Ca}m(v_m - v_{Ca}), \quad I_K = g_Kn(v_m - v_K), \quad I_L = g_L(v_m - v_L)$$

where g_{Ca} , g_K , g_L and v_{Ca} , v_K , v_L are the maximum cell conductances and resting potentials for the associated currents. The gating variables m , n take values in the range 0–1 representing the fraction of open to the total available channels for the associated currents. In the absence of spontaneous electrical activity (resting state), the gating variables have the sigmoidal forms:

$$m_\infty = \frac{1}{2} \left(1 + \tanh \frac{v_m - v_1}{v_2} \right), \quad n_\infty = \frac{1}{2} \left(1 + \tanh \frac{v_m - v_3}{v_4} \right)$$

Due to the fast kinetics of the Ca^{2+} gating, the models assumes $m = m_\infty$, while n follows n_∞ according to:

$$\frac{dn}{dt} = \phi_n \cosh \frac{v_m - v_3}{2v_4} (n_\infty - n)$$

The dependence of n upon cytosolic Ca^{2+} , is captured by setting:

$$v_3 = -\frac{v_5}{2} \tanh \left(\frac{[Ca^{2+}] - Ca_3}{Ca_4} \right) + v_6$$

The equivalent electrical circuit of the model muscle membrane is shown on figure 1.2. Application of Kirchhoff's laws implies:

$$C_m \frac{dv_m}{dt} = -I_K - I_{Ca} - I_L + I_{MR}$$

where C_m is the membrane capacitance.

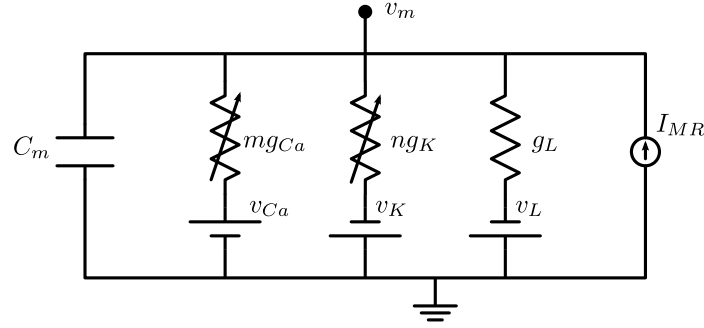
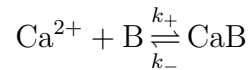


FIGURE 1.2: Smooth muscle membrane equivalent electrical circuit. Following the common convention, extracellular space is assumed grounded.

The model assumes that the myogenic response is mediated by the opening of non-selective cation channels which induce I_{MR} . In general, the model assumes that I_{MR} is an increasing function of blood pressure. So smooth muscle membrane depolarizes with increasing pressure and vice versa. Fine details on the explicit pressure dependence and the kinetics of I_{MR} are given in the subsequent chapters.

1.2.2 Free cytosolic calcium regulation

Let CaB and Ca^{2+} denote the bound and unbound states of Ca^{2+} ions found in the muscle's cytosol. An approximation, [60], of the buffering process is described by the reaction:



where all buffers are contained in B . Due to the significantly faster kinetics of the above reaction to the other intercellular processes, the reaction is assumed in equilibrium:

$$[\text{CaB}] = \frac{[\text{Ca}^{2+}]\text{B}_T}{K_d + [\text{Ca}^{2+}]}$$

where $K_d = k_-/k_+$, and $\text{B}_T = [\text{B}] + [\text{CaB}]$ is the total cytosolic buffer concentration. Let $[\text{Ca}^{2+}]_T = [\text{Ca}^{2+}] + [\text{CaB}]$ denotes the total cytosolic Ca^{2+} concentration.

Conservation of mass implies:

$$\frac{d[\text{Ca}^{2+}]_T}{dt} = J_{in} + J_{out}$$

where J_{in} and J_{out} are the Ca^{2+} influx and efflux, respectively. We assume that J_{in} is attributed solely to I_{Ca} , hence:

$$J_{in} = -\alpha I_{Ca}$$

where the constant $\alpha = 1/(z_{Ca}\beta V_{SM}F)$ relates current with concentration. In detail, V_{SM} is the total volume of the model smooth muscle, β the fraction of V_{SM} occupied by the cytosol, $z_{Ca} = 2$ the valence of Ca^{2+} , and F the Faraday constant. The negative sign is used since $I_{Ca} < 0$, by convention. The efflux is described by a first order decay:

$$J_{out} = -k_{Ca}[\text{Ca}^{2+}]$$

Combining with the equilibrium approximation, we get:

$$\frac{d[\text{Ca}^{2+}]}{dt} = (J_{in} - J_{out}) \frac{(K_d + [\text{Ca}^{2+}])^2}{(K_d + [\text{Ca}^{2+}])^2 + K_d B_T}$$

1.2.3 Cross-bridge cycling

Myosin light chain phosphorylation is modeled as a direct function of $[\text{Ca}^{2+}]$ having the sigmoidal form:

$$\psi = \frac{[\text{Ca}^{2+}]^3}{[\text{Ca}^{2+}]_m^3 + [\text{Ca}^{2+}]^3}$$

with ψ denoting the ratio of phosphorylated myosin light chain to the total available. The amount of formed cross-bridges is represented by ω which denotes the ratio of formed cross-bridges to the total available. As in [60], the kinetics of ω are described by the phenomenological equation:

$$\frac{d\omega}{dt} = k_\psi \left(\frac{\psi}{\psi_m + \psi} - \omega \right)$$

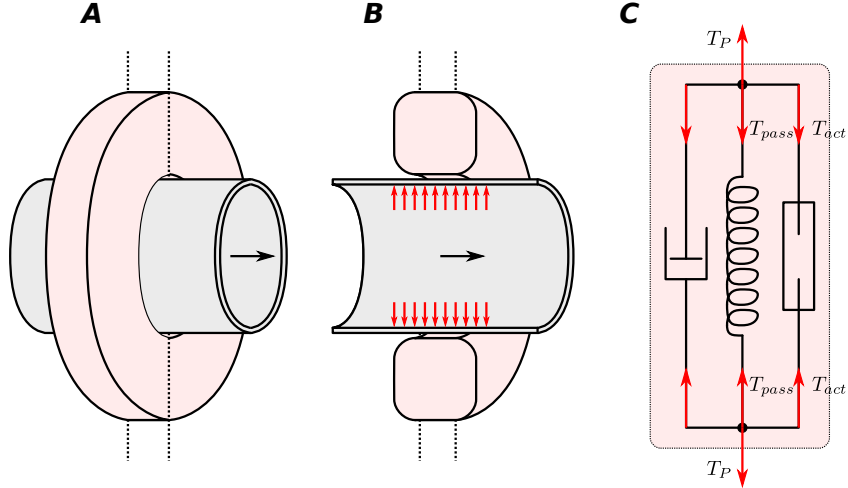


FIGURE 1.3: Model smooth muscle geometry and internal mechanics. *A*, smooth muscle and vascular lumen. *B*, muscle's cross-section. *C*, muscle's mechanics. Arrows indicate direction of blood flow (black) and tensions (red).

1.2.4 Muscle mechanics

To represent muscle mechanics, a similar approach to [21, 3, 20] is adopted. In particular, vasomotion is driven by the balance between pressure-induced tension, T_P that causes vasodilation, and wall tension, T_{wall} that causes vasoconstriction. Figure 1.3 shows a schematic representation of the model muscle's geometry and internal mechanical representation. Wall tension consists of a passive and an active components:

$$T_{wall} = T_{pass} + T_{act}$$

The active component of wall tension is directly proportional to the amount of formed cross-bridges ω , while the passive one is a function only of luminal radius.

Tension arising from transmural pressure is given by the Laplace law:

$$T_P = (P - P_{ext})r$$

where P and P_{ext} denote the hydrostatic pressures interior and exterior to the vascular wall.

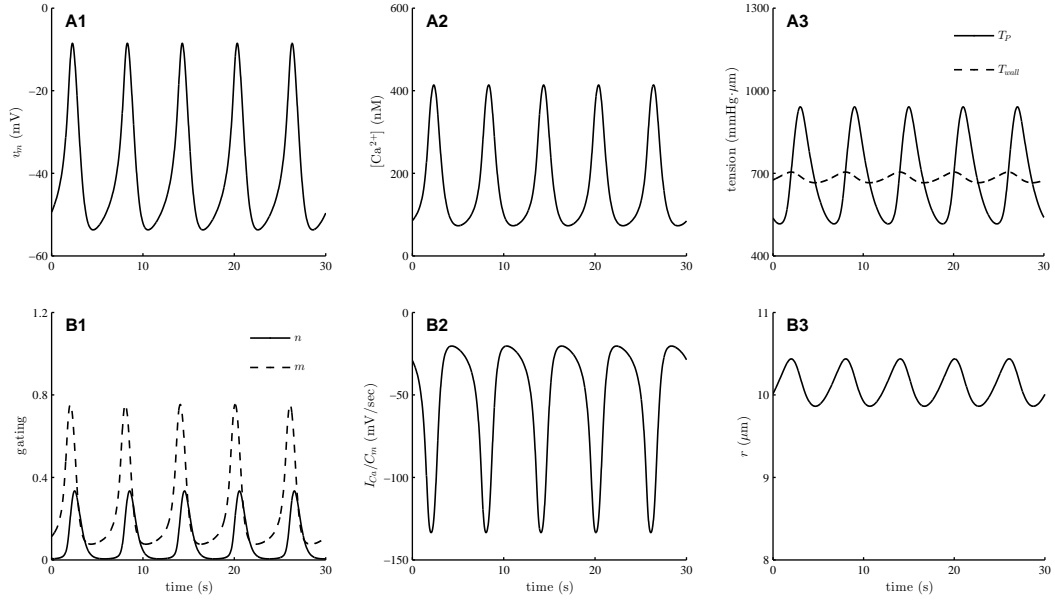


FIGURE 1.4: Smooth muscle dynamics. A1, membrane potential; B1, Ca^{2+} and K^+ channels gating; A2, free cytosolic Ca^{2+} ; B2, transmembrane Ca^{2+} current; A3, muscle tensions; B3, muscle luminal radius. Spontaneous oscillations arise from the interaction of membrane potential with K^+ gating and are transmitted to muscle radius.

Luminal radius r is determined by the balance of tensions developed across the muscle's wall:

$$\frac{dr}{dt} = \frac{1}{\tau_c} (T_P - T_{wall})$$

The time constant τ_c is characteristic of the internal muscle's viscosity [3].

1.2.5 Discussion

In the chapters that follow, the framework described above is adopted with appropriate modifications when necessary. For example, for the construction of the vascular model in Chapter 2, it is required the formation of a linear ensemble of smooth muscles. In this case, appropriate currents that model smooth muscle-to-smooth muscle and smooth muscle-to-endothelium communication are added.

Using the most common choice of parameter values (for example see [27, 60]

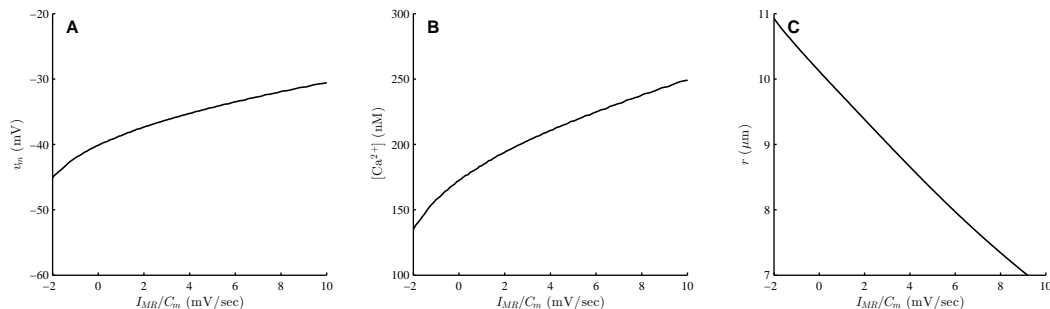


FIGURE 1.5: Smooth muscle response to steady myogenic current I_{MR} . A, time average membrane potential; B, time average free cytosolic Ca^{2+} ; C, time average luminal radius. Large I_{MR} leads to membrane depolarization, increase of cytosolic Ca^{2+} , and muscle contraction. Low I_{MR} , thought the opposite effects, leads to muscle dilation.

or any of the subsequent chapters) and a prescribed myogenic current $I_{MR} = 0$, the model predicts spontaneous oscillations near 165 mHz, see figure 1.4. Such oscillations originate in the limit cycle developed between v_m and n , for details see [60]. Oscillations of v_m , are transmitted through m , to fluctuations of I_{Ca} . In turn, I_{Ca} fluctuations are transmitted through J_{in} to $[Ca^{2+}]$, which in turn drives cross-bridge cycling ω , and active tension T_{act} . Finally, T_{act} transmits the oscillations to luminal radius r (spontaneous vasomotion).

The application of $I_{MR} > 0$ leads to membrane depolarization, which leads to influx of Ca^{2+} through the enhancement of the opening of the associated channels, which in turn leads to increase of cytosolic Ca^{2+} , cross-bridge formation, active wall tension, and thus vasoconstriction. Similarly, the application of $I_{MR} < 0$ leads to membrane hyperpolarization with the opposite effects which lead to vasodilation. Figure 1.5 shows time averages of membrane potential, free cytosolic Ca^{2+} , and luminal radius for a range of prescribed I_{MR} .

Autoregulation and Conduction of Vasomotor Responses

2.1 Introduction

Electrical stimulation or micropipette application of appropriate vasoactive substances onto the surface of arterioles induces not only a local vasomotor response, but also a conducted vasomotor response which propagates upstream and downstream along the vessel. Conducted vasomotor responses are believed to be important in the coordination of the microvascular tone.

Steinhausen et al. [155] analyzed the propagation of vasomotor responses, induced by local electrical stimulation, in split hydronephrotic rat kidneys. Their results indicate that the responses decay with increasing distance from the stimulation site, and that the decay is significantly faster upstream than downstream. An explanation for the asymmetric decay rates, which was elusive, is a motivation for the present study.

In a previous study [27], we developed a detailed mathematical model of the myogenic response of a small segment of the afferent arteriole (AA) wall, including

the endothelium and the surrounding smooth muscle cells. That model was used to examine the response of the AA segment to changes in mean and pulsatile pressure. Simulation results of that model are consistent with the hypothesis that the AA myogenic response plays an important role in protecting the glomerular capillaries against elevated systolic pressures.

The goal of this study is to develop a multi-cell model of the AA by connecting a series of AA smooth muscle cells and endothelial cells via gap junction coupling, and to use the model to study the myogenic response of the AA, and its response to local electrical stimulation. The AA model is intended to be used as an essential component in models of integrated renal hemodynamic regulation.

2.2 Mathematical model

2.2.1 Multi-cell afferent arteriole model

The model is an extension of our previous AA cell model [27] and represents a segment of an AA of length L ($L \sim 300\mu\text{m}$), consisting of a series of $N_{\text{cell}} = 101$ smooth muscle cell models [27], coupled via their gap junctions and via an endothelial cell layer. (An odd number of smooth muscle cell models were represented so that there is a middle cell that can be stimulated to study any asymmetry in the conduction of vasoconstrictive response.) The model AA segment is connected in-series to a fixed resistor, denoted R_{end} . The inflow pressure ($P_0(t)$ at $x = 0$) and the pressure at the end of the fixed resistor P_{end} (at $x = 2L$) are assumed to be known *a priori*. A schematic diagram is shown in Fig. 2.1. When the inflow pressure P_0 is varied, or when a vasoconstrictive or vasodilative response is induced, the pressure at the end of the AA segment, which is denoted $P(L, t)$ and which we refer to as the “outflow pressure,” may also vary. We set P_{end} to 0 mmHg and R_{end} to equal the time-averaged value of the total resistance of the unstimulated AA with $P_0 = 100$ mmHg, so that when the inflow pressure $P_0 = 100$ mmHg, the outflow pressure $P(L) \approx 50$ mmHg.

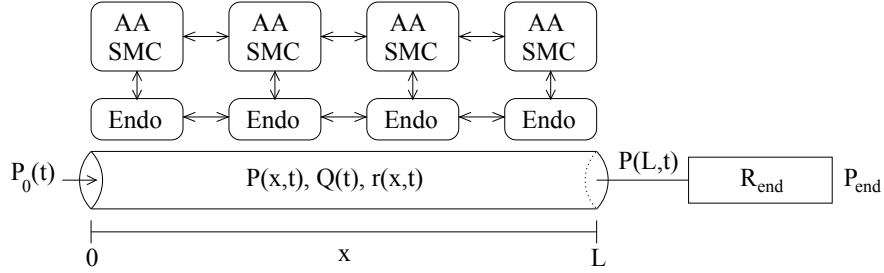


FIGURE 2.1: Schematic representation of model afferent arteriole (AA). Hydrodynamic pressure $P_0(t)$ drives flow, $Q(t)$, into AA entrance ($x = 0$) at time t . The model AA is connected to a fixed resistor, R_{end} , at the end of which pressure is fixed at P_{end} . Variations in luminal pressure $P(x, t)$ induce myogenic response in AA smooth muscle cells and change luminal radius $r(x, t)$. AA smooth muscle cells (SMC) and endothelial cells (Endo) are coupled by gap junctions.

Each AA smooth muscle cell model incorporates the ionic transports, cell membrane potential, muscle contraction of the AA smooth muscle cells, and the mechanics of a thick-walled cylinder. The model represents the interaction of Ca^{2+} and K^+ fluxes mediated by voltage-gated and voltage-calcium-gated channels, respectively, which gives rise to the periodicity of those transports. This results in a time-periodic cytoplasmic calcium concentration, myosin light chains phosphorylation, and cross-bridges formation with the attending muscle stress. The vessel's transmural pressure determines a hoop stress. The resultant hoop, elastic, and muscle stresses determine the rate of change of the vessel's diameter: vasomotion. In addition, the model incorporates the myogenic response mechanism that is based on the hypothesis that the activity of non-selective cation channels is shifted by changes in transmural pressure, such that vessel diameter decreases with increasing pressure and vice versa. A detailed description of the equations for the AA smooth muscle cell model and the model parameters can be found in the appendix at the end of the chapter and in Ref. [27]. Below we describe a few key equations, including those that are modified from the previous model [27].

The rate of change of free cytosolic calcium concentration in the i -th smooth

muscle cell, denoted Ca^i , is given by

$$\frac{d\text{Ca}^i}{dt} = (-\alpha g_{\text{Ca}} m_\infty (v^i - v_{\text{Ca}}) - k_{\text{Ca}} \text{Ca}^i) \left(\frac{(K_d + \text{Ca}^i)^2}{(K_d + \text{Ca}^i)^2 + K_d B_T} \right),$$

where $\alpha = 1/(z_{\text{Ca}} \beta V_{\text{cell}} F)$, $z_{\text{Ca}} = 2$ is the valence of the calcium ion, β is the fraction of cell volume occupied by the cytosol, V_{cell} is the cell volume, F is the Faraday constant, m_∞ is the voltage-dependent equilibrium distribution of open calcium channel states, g_{Ca} is the maximum whole-cell membrane conductance for the calcium current, k_{Ca} is the first-order rate constant for cytosolic calcium extrusion, K_d is the ratio of the forward and backward reaction rates of the calcium-buffer system, and B_T is the total buffer concentration.

Neighboring AA smooth muscle cell models communicate via their gap junctions. The rate of change of the membrane potential of the i -th cell, v^i , is the sum of transmembrane currents:

$$C \frac{dv^i}{dt} = -I_L^i - I_K^i - I_{\text{Ca}}^i + I_{\text{gap}}^i + I_{\text{SMC-endo}}^i + I_{\text{myo}}^i, \quad (2.1)$$

where C denotes the cell capacitance. The transmembrane leak, potassium, calcium, inter-smooth muscle cell gap junction, and smooth muscle-endothelial cell gap junction currents, denoted I_L^i , I_K^i , I_{Ca}^i , I_{gap}^i and $I_{\text{SMC-endo}}^i$ respectively, are given by $I_L^i = g_L (v^i - v_L)$, $I_K^i = g_K n (v^i - v_K)$, $I_{\text{Ca}}^i = g_{\text{Ca}} m_\infty (v^i - v_{\text{Ca}})$, $I_{\text{gap}}^i = g_{\text{gap}} (v^{i-1} - 2v^i + v^{i+1})$, and $I_{\text{SMC-endo}}^i = g_{\text{SMC-endo}} (v_e^i - v^i)$, respectively, where g_L , g_K , and g_{Ca} are associated with the respective whole-cell membrane conductances, v_L , v_K , and v_{Ca} denote the respective Nernst reversal potentials, v_e^i denotes the membrane potential of the endothelial cell, and g_{gap} and $g_{\text{SMC-endo}}$ are the coupling strengths. I_{myo}^i denotes the current arising from the myogenic response, which is described below.

Myogenic response

Our model's mechanism for the myogenic response is based on the hypothesis that changes in hydrostatic pressure P induce changes in the activity of non-selective cation channels. The resulting changes in membrane potential then affect calcium influx through changes in the activity of the voltage-gated calcium channels [40]. This is represented by the pressure-dependent current I_{myo}^i in Eq. (2.1) (given in pA), which is described by

$$\frac{dI_{\text{myo}}^i(t)}{dt} = \begin{cases} -(75 \cdot \text{s}^{-1})(I_{\text{myo}}^i(t) - \bar{I}_{\text{myo}}^i), & \text{if } \frac{dP^i(t-\tau_m)}{dt} \geq 0, \\ -(1.25 \cdot \text{s}^{-1})(I_{\text{myo}}^i(t) - \bar{I}_{\text{myo}}^i), & \text{if } \frac{dP^i(t-\tau_m)}{dt} < 0, \end{cases} \quad (2.2)$$

where the target current \bar{I}_{myo}^i is given by (in pA)

$$\begin{aligned} \bar{I}_{\text{myo}}^i(t) = \max \left(9.75 \times 10^{-2}, 2.51 \times 10^{-7} (P^i(t - \tau_m) - P_*^i)^3 + \right. \\ \left. + 2.73 \times 10^{-5} (P^i(t - \tau_m) - P_*^i)^2 \right. \\ \left. + 0.96 \times 10^{-3} (P^i(t - \tau_m) - P_*^i) \right) \end{aligned} \quad (2.3)$$

where P^i denotes the transmural pressure (in mmHg), and P_*^i denotes reference transmural pressure, which is the pressure that the i -th cell normally feels. The different rate constants in Eq. (2.2) corresponding to pressure increase or decrease yield a faster vasoconstriction response compared to vasodilation. Because fluid pressure decreases along the model AA, the AA cells respond to different external environment. Thus, we adjust P_*^i based on the cells' location within the AA, and set P_*^i to be a linearly decreasing function of its center position $(i - \frac{1}{2})\Delta x$, where Δx is the length of one AA subsegment, taken to be $3 \mu\text{m}$. More specifically, we set $P_*^i = 100 \text{ mmHg} - ((i - \frac{1}{2})\Delta x / L) \times 50 \text{ mmHg}$. In the absence of pressure variations, $I_{\text{myo}}^i = 0$.

The AA wall movement is driven by the balance of wall tension, which depends on P^i , and the elastic and contractile forces [27]. Because P^i decreases along the AA,

wall tension decreases; to ensure force balance, we scale the elastic and contractile forces by a factor ξ^i that decreases linearly along the AA, from $\xi^i = 1$ at $x = 0$ to $\xi^i = 0.5$ at $x = L$ (see Eq. (2.9)).

It has been reported that the AA myogenic mechanism exhibits an asymmetry in its response times for vasoconstriction and vasodilation [106, 104]. Loutzenhiser and co-workers [106, 104] observed that the initial delay in the activation of a pressure-dependent vasoconstriction was ~ 0.3 s, whereas vasodilation exhibited an initial delay of ~ 1 s. To attain that asymmetry, the delay τ_m in Eq. (2.3) depends on the rate of change of P^i : $\tau_m = 0.3$ s for increasing pressure, and $\tau_m = 1$ s for decreasing pressure.

Intercellular communication

Axial signal propagation along an AA segment takes place through two pathways: gap junctions between neighboring AA smooth muscle cells, or conduction through the endothelial cell layer. Communication through AA smooth muscle cell gap junctions is represented by the I_{gap}^i term in Eq. (2.1).

The endothelial cell layer consists of N_{cell} endothelial cell models; each is connected via gap junctions to an AA smooth muscle cell and to its neighboring endothelial cells. The model represents the membrane potential of the i th endothelial cell, denoted by v_e^i

$$C_e \frac{dv_e^i}{dt} = g_{\text{SMC-endo}}(v^i - v_e^i) + I_{\text{gap,e}}^i, \quad (2.4)$$

where C_e denotes the capacitance of the endothelial cell. The first term on the right-side of Eq. (2.4), $g_{\text{SMC-endo}}(v^i - v_e^i)$, denotes the gap-junction current between smooth muscle and endothelial cells. The second term, $I_{\text{gap,e}}^i = g_{\text{gap,e}}(v_e^{i-1} - 2v_e^i + v_e^{i+1})$, denotes axial gap-junction current.

Axial gap junction communication requires the specification of boundary con-

ditions for the first and last cells ($i = 1$ and N_{cell}). In the absence of an electrical stimulation, we assume that the AA is electrically sealed at the two ends, i.e., zero gap-junction currents at the two ends. Thus, $I_{\text{gap}}^1 = g_{\text{gap}}(-v^1 + v^2)$ and $I_{\text{gap}}^{N_{\text{cell}}} = g_{\text{gap}}(v^{N_{\text{cell}}-1} - v^{N_{\text{cell}}})$. Analogous boundary conditions are applied to the endothelial cells. When a local electrical stimulation is applied to the vessel, a fraction of that current is assumed to exit through the vessel boundaries. The remainder of that current is presumably accounted for by the leak current, so that there is minimal net charge accumulation within the vessel.

2.2.2 Luminal fluid model

Luminal flow through the model AA is assumed to be at quasi-steady state, and is described by Poiseuille flow

$$\frac{dP}{dx} = -\frac{8\mu Q}{\pi r^4}, \quad (2.5)$$

where P is the hydrostatic pressure, μ is the dynamic viscosity of blood, Q is the volumetric flow rate, and r is the luminal radius.

As previously noted, the pressure drop across the AA segment and the resistor, given by $P_{\text{end}} - P_0(t)$, is assumed to be known *a priori*. The resistance of the AA segment is given by its luminal radius, which may change due to spontaneous vasomotion, myogenic response, or electrically induced vasomotor response. Given the pressure drop and the total resistance, the volumetric flow Q can be computed as follows:

$$Q = \frac{\pi(P_0(t) - P_{\text{end}})}{16\mu L} \left(\sum_{i=1}^N \frac{\Delta x}{(r^i)^4} + R_{\text{end}} \right)^{-1},$$

Once Q is known, we can then update the hydrostatic pressure at each cell.

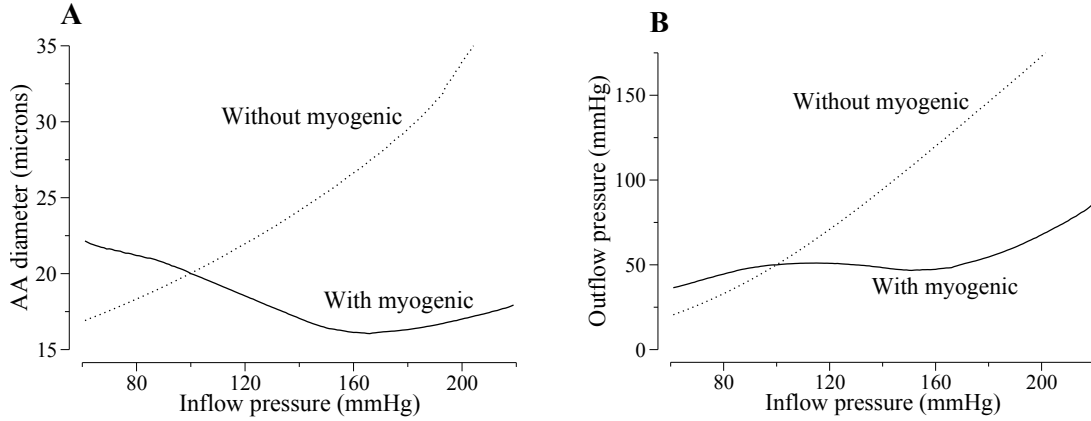


FIGURE 2.2: Space and time-averaged luminal diameter of the AA (panel A) and outflow pressure (panel B) as a function of inflow pressure P_0 with (solid line) or without (dotted line) myogenic response.

2.3 Results

2.3.1 Autoregulatory response of the model vessel

We assessed the model AA's ability to maintain a stable outflow pressure by applying a range of time-independent inflow pressure and computing time-averaged luminal diameters and outflow pressures. Results are shown in Fig. 2.2. Panel A, solid line, shows time-averaged AA diameter profiles for various inflow pressures values, where vasodilation can be seen at low pressure (80 mmHg), and vasoconstriction at higher pressure (120 mmHg). From the outflow pressure values shown in Fig. 2.2B, solid line, one observes that for inflow pressure between 80–180 mmHg, the model AA maintained a somewhat stable outflow pressure that varied between ~ 45 –55 mmHg, where 50 mmHg is the outflow pressure that corresponds to a reference inflow pressure of 100 mmHg. When inflow pressure exceeded 180 mmHg, the model AA failed to adequately compensate, and outflow pressure began to noticeably rise.

To illustrate the effects of the myogenic response, we simulated the administration of papaverine, which is a smooth muscle relaxant that abolishes autoregulation in the dog kidney [160]. We computed outflow pressure while neglecting myogenic response;

i.e., we assumed that the activity of the non-selective cation channel is unaffected by changes in transmural pressure. In all simulations, we set I_{myo}^i to 0 for all i 's. In the absence of myogenic response, the model vessel reacts passively to changes in transmural pressure (see Figs. 2.2A and 2.2B, dotted lines). At higher inflow pressures, the vasodilation reduces vascular resistance, which lowers pressure drop and further increases downstream pressure relative to base case, resulting in a larger vessel diameter downstream (results not shown).

2.3.2 Responses to a step perturbation

To better understand the characteristic of our AA model, we simulated the time-courses of the responses of diameter and pressure to a step increase or decrease in input pressure. Results are shown in Fig. 2.3.

When inflow pressure was increased from 100 to 120 mmHg (Fig. 2.3A, solid line), the model AA constricted. The time-course of the diameter corresponding to the first AA cell is shown in Fig. 2.3B, solid line. The time-courses of the AA diameter at other spatial locations are similar and not shown. The vasoconstrictive response was fully attained after ~ 10 s. The outflow pressure initially rose with the inflow pressure, but, as the AA constricted, the outflow pressure gradually returned to its reference value of ~ 50 mmHg (Fig. 2.3C, solid line).

When inflow pressure was decreased from 100 to 80 mmHg, the model AA first briefly exhibited a passive constriction, and then dilated (Fig. 2.3B, dashed line). After an initial decline, outflow pressure (Fig. 2.3C, dashed line) and fluid flow (not shown) returned to their respective references values. Vasodilation was fully attained after ~ 20 s.

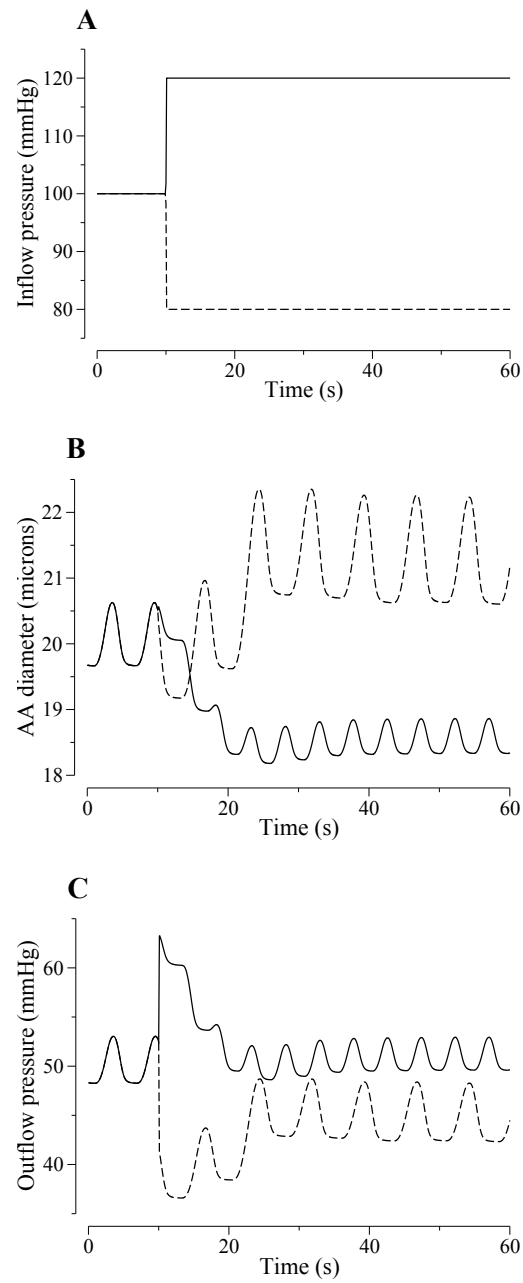


FIGURE 2.3: Model responses to a step 20% increase (solid lines) or decrease (dashed line) in AA inflow pressure (panel A). Changes in AA diameter and outflow pressure are shown in panels B and C, respectively.

2.3.3 Responses to sinusoidal oscillations in inflow pressure

To study the characteristics of the transduction of oscillations in fluid pressure along the AA, we superimposed a sinusoidal perturbation onto the steady-state inflow pressure ($x = 0$): we applied a pressure of

$$P_0(t) = \bar{P}_0 + P_p \sin(2\pi ft),$$

where $\bar{P}_0 = 100$ mmHg, $P_p = 20$ mmHg, and f denotes the oscillation frequency.

We first studied the model AA's response to a slow sinusoidal perturbation with $f = 0.1$ Hz. The resulting oscillations in AA luminal diameter and outflow pressure are illustrated in Figs. 2.4A2 and 2.4A3. The interactions among pressure perturbations, spontaneous oscillations in AA cellular transport and diameter, the asymmetric myogenic response times to pressure increase and decrease, and the coupling among the AA cells through gap junction, endothelial cells, and luminal fluid flow transform the regular oscillations in inflow pressure to highly irregular oscillations in luminal diameter and outflow pressure.

Next we imposed a faster oscillation of $f = 1$ Hz in the inflow pressure. Note that these pressure oscillations are much faster than the natural frequency of the AA, taken to be the frequency of the spontaneous vasomotion (~ 170 mHz). The resulting oscillations in AA luminal diameter and outflow pressure are illustrated in Figs. 2.4B2 and 2.4B3. Instead of responding to the high-frequency pressure variations passively without attenuation, the model vessel exhibited a sustained vasoconstriction, owing to the cumulative effect of the faster contractile responses [27, 106, 104].

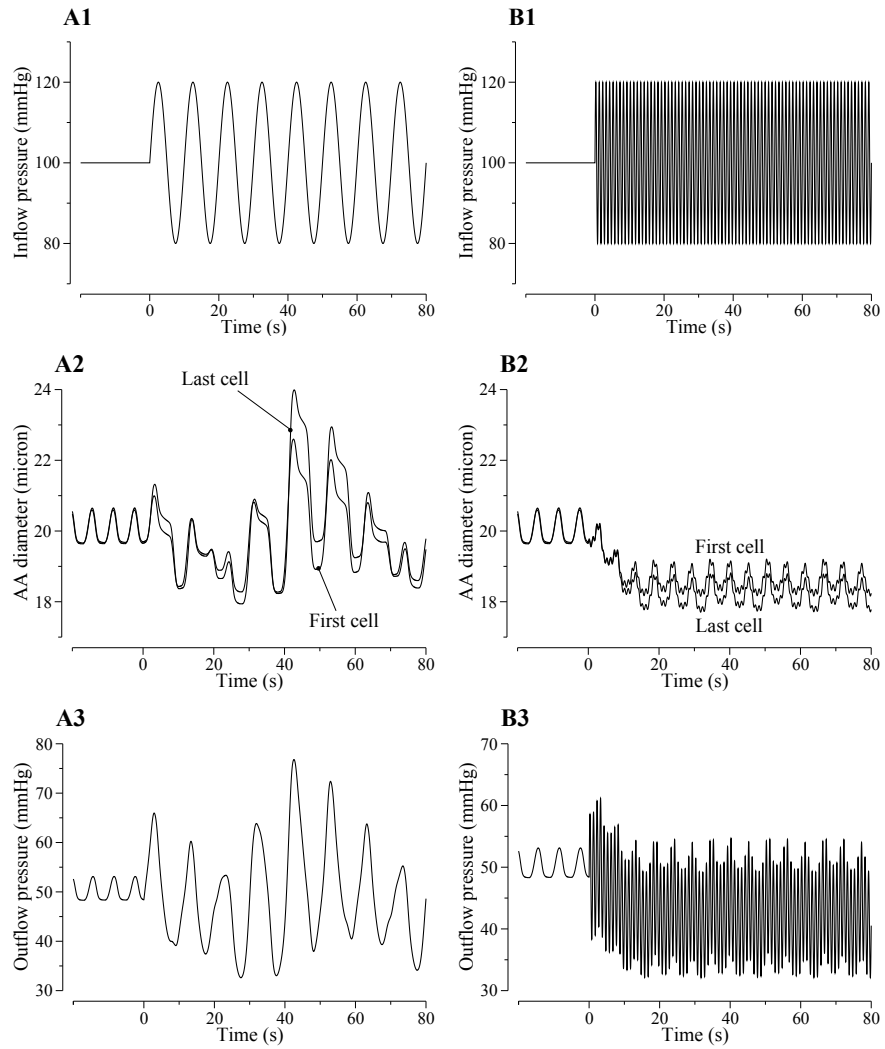


FIGURE 2.4: Oscillations, as function of time, in AA luminal diameter (panels A2 and B2) and outflow pressure (panels A3 and B3) when a sinusoidal perturbation is applied to inflow pressure pressure (panels A1 and B1). Panels A1–A3: slow oscillations at 0.1 Hz. Panels B1–B3: fast oscillations at 1 Hz. Fast pressure oscillations give rise to a sustained vasoconstrictive response.

2.3.4 Asymmetric upstream and downstream propagation

We used the model to analyze the propagation of vasoconstrictive responses, induced by local electrical stimulation, along the AA. That is modeled by adding a depolarization term, I_{depol}^i , to Eq. (2.1):

$$C \frac{dv^i}{dt} = -I_L^i - I_K^i - I_{\text{Ca}}^i + I_{\text{gap}}^i + I_{\text{SMC-endo}}^i + I_{\text{myo}}^i + I_{\text{depol}}^i.$$

We assumed that only the middle AA smooth muscle cell was depolarized. Thus, $I_{\text{depol}}^i = 0$ except when i equals the index of the middle AA cell (denoted $N_{\text{mid}} = (N_{\text{cell}} + 1)/2$), in which case a depolarizing current was applied for $t \geq 20$ s:

$$I_{\text{depol}}^{N_{\text{mid}}} = \begin{cases} 0, & 0 \leq t < 20 \text{ s}, \\ 11.31 \text{ pA}, & t \geq 20 \text{ s}. \end{cases} \quad (2.6)$$

The value of I_{depol}^i was chosen to achieve a steady-state constricted diameter of $\sim 10 \mu\text{m}$ at the stimulation site. To avoid an excessive accumulation of current within the vessel, we assumed that 50% of the depolarizing current exited through the two ends of the model AA. Thus, we set $I_{\text{gap}}^1 = g_{\text{gap}}(-v^1 + v^2) - 0.25I_{\text{depol}}^{N_{\text{mid}}}$ and $I_{\text{gap}}^{N_{\text{cell}}} = g_{\text{gap}}(v^{N_{\text{cell}}-1} - v^{N_{\text{cell}}}) - 0.25I_{\text{depol}}^{N_{\text{mid}}}$. Because the current leaving the two ends of the AA is the same, any asymmetry in the propagation of the vasomotor response is not caused by boundary conditions.

Figure 2.5 shows spatial profiles of smooth muscle cell and endothelial cell membrane potentials, luminal pressure, and vascular diameter at three time instances. The profiles labelled “ t_0 ” were obtained 0.01 s before the stimulation. At this time, pressure exhibits an approximately linear drop, with vascular diameter and membrane potential oscillating around constant means.

The profiles labelled “ t_1 ” in Figure 2.5 show the response of the AA 0.15 s after the electrical stimulation is applied. Note that sufficiently far away from the stimulation site, v_e is higher than v , i.e., v lags v_e , which indicates that axial propagation of

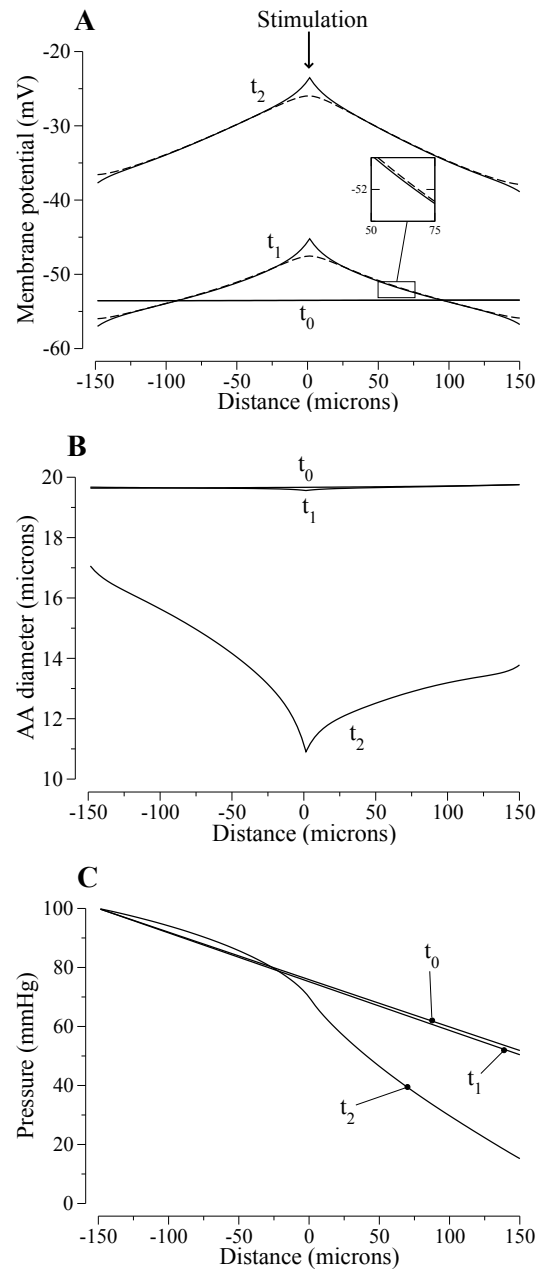


FIGURE 2.5: Model responses to an electrical stimulation, in membrane potentials v and v_e (panel A), luminal diameter (panel B), and pressure (panel C). Profiles are shown for three time instances: t_0 , 0.01 s before stimulation; t_1 , 0.15 s after stimulation; t_2 , 13.25 s after stimulation.

vasoresponse takes place primarily through the gap-junctions among the endothelial cells, which are assumed to have much higher conductance than the smooth muscle cell gap junctions. Depolarization raised intracellular Ca^{2+} concentration of the stimulated cell, and the AA constricted locally. The increase in vascular resistance caused downstream pressure to decrease; in contrast, upstream pressure was not affected. The lower downstream pressure induced a myogenic response there. Note that near the two ends, the vessel was hyperpolarized, i.e., $v(t_1) < v(t_0)$ near the ends. That transient response is due to the boundary conditions imposed for the smooth muscle cell gap-junction communication, where we assume that a fraction of the stimulating current exits through the vessel ends, thereby transiently and locally hyperpolarizing the vessel.

As the vasomotor response was conducted along the AA, the vessel further constricted and the pressure drop increased. Profiles for membrane potential, luminal pressure, and vascular diameter 13.25 s after the stimulation are shown in Fig. 2.5, labelled “ t_2 .” The model predicts that while the propagation of the depolarizing current was approximately symmetrical around the stimulation point (see Fig. 2.5A), the strength of the vasomotor response was stronger downstream (see Fig. 2.5B). To further illustrate the asymmetry of the vasoconstrictive response, we show the luminal diameters of the upstream-most, middle, and downstream-most cells as functions of time in Fig. 2.6A. At 30 s after the stimulation, the diameter of the downstream-most cell was $\sim 80\%$ of the upstream-most one.

We also show, in Fig. 2.6B, the percentage of the maximum response along the AA, obtained approximately 30 s after the stimulation. The downstream and upstream decays are approximated by exponential functions with length constants of 340 and 121 μm , respectively. Steinhausen et al. [155] measured similar decay constants of 420 and 150 μm in a vascular tree that comprised mostly of cortical radial artery. The length-scale ratio predicted by the model (2.80) matches that of

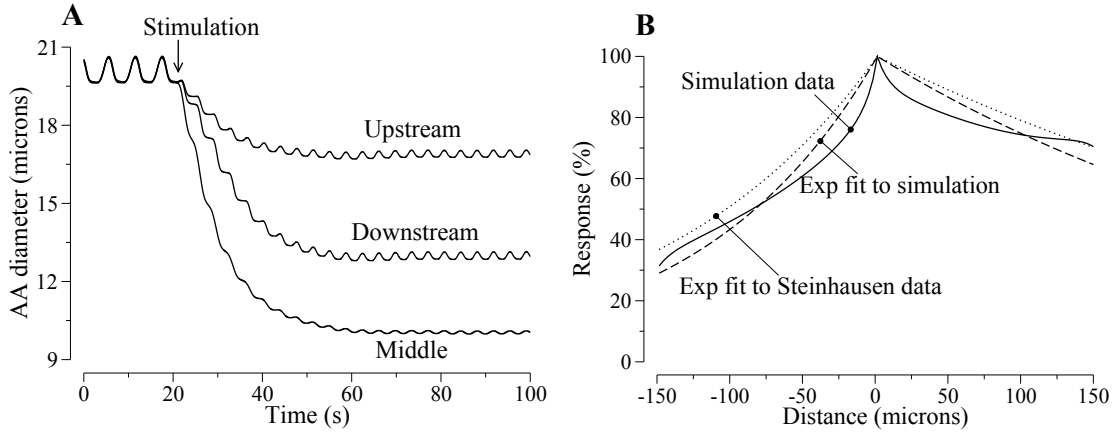


FIGURE 2.6: Propagation of vasoconstrictive response induced by an electrical stimulation. A, responses of selected AA cells as functions of time. B, comparison of model AA diameter profile, given as percentage of maximum response, obtained ~ 30 s after stimulation, with exponential fit of measurements by Steinhausen et al. [155].

Steinhausen et al.

The above results illustrate that symmetric electrical conduction along the AA (Fig. 2.5A) transforms into asymmetric mechanical response (Figs. 2.5B, 2.6A, 2.6B). That asymmetric decay can be attributed to two factors. The first contributing factor is the shift in the autoregulatory response of a depolarized AA smooth muscle cell. Below we conducted simulations that demonstrate the effect of depolarization on the myogenic-induced vasodilation of an AA smooth muscle cell. Another factor is the differences in the muscle mechanics of the smooth muscle cells, which may have arisen as a result of the adjustments of the smooth muscle cell to their surrounding pressure that, at steady state, decreases approximately linearly in space (see Eq. (2.9)). Assuming that the myogenic response, in terms of the dependence of the non-selective cation channel opening on pressure variations, is the same among the smooth muscle cells, the balance between muscle stresses and wall tension (Eq. (2.10)) differs among different cells except at the steady-state pressure.

To illustrate the above arguments, we simulated the individual myogenic re-

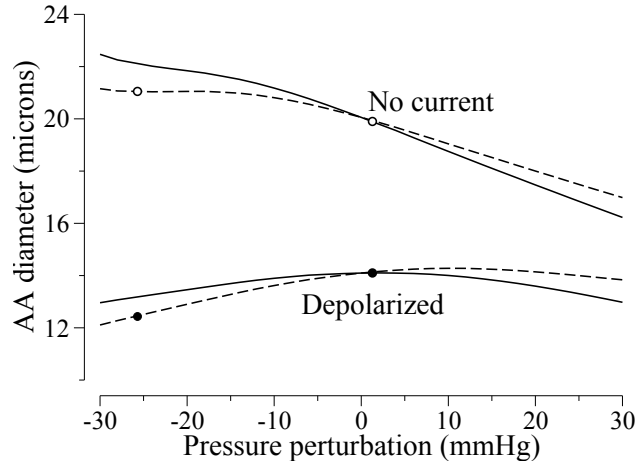


FIGURE 2.7: Time-averaged AA luminal diameters as a function of perturbation from reference transmural pressure, obtained for an upstream cell (solid lines) and a downstream cell (dashed lines). Simulations were done with a depolarizing current of 0.06 pA and without.

sponses of two cells along the AA segment, one at $x = L/4$ and the other at $x = (3/4)L$, which we call “upstream cell” and “downstream cell,” respectively. (Note that these two cells were chosen to be equidistant from the midpoint, where the electrical stimulation was applied in the preceding experiment. Since the propagation of the electrical current is approximately symmetric, the two cells’ membrane potentials should not differ significantly.) In the following isolated-cell simulations, we prescribed transmural pressure values, simulated only gap-junction current between smooth muscle and endothelial cells, and neglected axial gap-junction currents. We computed time-averaged inner diameters of the two cells for a range of pressure perturbations ΔP , given by perturbations from their reference pressure P^* , which are 87.5 and 62.5 mmHg, respectively. Results are shown in Fig. 2.7, the curves labelled “No current.” Both model cells constricted as pressure increased, but constriction was stronger for the upstream cell. Nonetheless, at the pressures that the two cells experienced during the preceding electrical stimulation experiment, which deviated from the upstream and downstream reference pressure values by +2.50

and -25.7 mmHg, respectively (see Fig. 2.5C), the cell models predicted that the downstream cell was dilated relative to the upstream cell (compare open circles in Fig. 2.7), a result that is inconsistent with the asymmetric conduction response.

We then repeated the isolated-cell simulations, this time with a depolarizing current of 0.06 pA applied to each cell. That depolarizing current was chosen so that the predicted membrane potentials are similar to their values in the preceding vasoresponse conduction simulations. The model predicted that, in the presence of the depolarizing current, which induced vasoconstriction in the cells and shifted their autoregulatory curves, the ability of the cells to dilate was impaired. As a result, at lower pressures, the myogenic-induced vasodilation failed to sufficiently compensate for the lower tension force, and the diameter of both cells decreased. The differences in the cells' muscle mechanics also play a role, in that the downstream cells are even less able to dilate at low pressure. Recall that in the preceding electrical stimulation experiment, the upstream and downstream cells experienced fluid pressures that deviated from their reference pressure values by $+2.5$ and -25.7 mmHg, respectively. At those pressure perturbations, the downstream cell exhibited a diameter that is $\sim 84\%$ of the upstream cell (compare closed circles in Fig. 2.7.)

To use these results to explain the asymmetric propagation of vasoresponse along the AA vessel, we note that following the application of the depolarizing current, the AA constricted, vascular resistance increased, and downstream pressure decreased. That drop in downstream pressure resulted in two competing effects: a decrease in the tension force arising from transmural pressure, and a vasodilative myogenic response. However, as can be seen in Fig. 2.7, a depolarized cell cannot effectively dilate, and that impairment is more pronounced for downstream cells. Consequently, the lower tension force dominated downstream, leading to a slower decay of the vasoconstrictive response downstream. In other words, the balance between the two competing effects resulting from the lower downstream pressure—vasoconstriction

Table 2.1: Vasoresponse propagation length constants λ 's for differing boundary conditions. α_{BC} denotes the fraction of depolarizing current that escapes through the ends of the AA (* denotes the base case).

α_{BC}	downstream λ (μm)	upstream λ (μm)	λ ratio
Ref. [155]	420	150	2.80
0.3	334.95	123.58	2.71
0.4	383.15	131.24	2.92
0.5*	339.82	121.27	2.80
0.6	275.97	105.65	2.61
0.7	211.61	87.54	2.42

from the lower tension force, and vasodilation from myogenic response—shifted in favor of the former when a depolarizing current is applied.

2.3.5 Parameter sensitivity studies

In the simulations for asymmetric propagation, we set the amount of depolarizing current that exits through the two ends of the vessels, denoted by I_{BC} , to $I_{BC} = \alpha_{BC} I_{\text{depol}}^{51}$ where $\alpha_{BC} = 0.5$. To assess the impact of that assumption on model predictions, we conducted a parameter sensitivity study in which we recomputed the conduction length constants for $\alpha_{BC} = 0.3, 0.4, 0.6, 0.7$. Results are summarized in Table 2.1. Model predicted that propagation length constants decrease as α_{BC} increases, because as more current was allowed to exit through the ends of the vessel, the extent to which AA was depolarized was reduced (thus, less constriction). This result is consistent with our argument that the asymmetric vasoresponse propagation arises from the shift in the autoregulatory response of a depolarized smooth muscle cell. Nonetheless, in all cases the model predicted a stronger downstream propagation of the vasomotor response, with the downstream-upstream length-scale ratios all fall within 15% of the value (2.80) measured by Steinhausen et al. [155].

The model assumes that the conductance among smooth muscle cells is low compared to that among endothelial cells. To assess model sensitivity to variations in

Table 2.2: Vasoreponse propagation length constants λ 's for varying gap-junction coupling constants (* denotes the base case).

Percentage of base-case value (%)	downstream λ (μm)	upstream λ (μm)	λ ratio
inter-smooth muscle cell coupling, g_{gap}			
120	445.36	140.58	3.17
110	390.36	131.37	2.97
100*	339.82	121.27	2.80
90	290.31	110.01	2.64
80	232.25	94.40	2.46
inter-endothelial cell coupling, $g_{\text{gap,e}}$			
120	382.87	130.63	2.93
110	361.85	126.18	2.87
100*	339.82	121.27	2.80
90	318.95	116.39	2.74
80	295.18	110.37	2.67
smooth muscle cell-endothelial cell coupling, $g_{\text{SMC-endo}}$			
120	353.94	124.15	2.85
110	346.21	122.72	2.82
100*	339.82	121.27	2.80
90	332.72	119.80	2.78
80	325.68	118.29	2.75

gap-junction coupling, we varied g_{gap} , $g_{\text{gap,e}}$ and $g_{\text{SMC-endo}}$, and we recomputed conduction length constants. Results are shown in Table 2.2. With stronger coupling, the vasoreponse decayed more slowly along the vessel, in both directions. When $g_{\text{gap,e}}$ or $g_{\text{SMC-endo}}$ is varied from 80% to 120% of base-case values, the downstream-upstream length-scale ratios λ all fall within 5% of base-case value. Model results are relatively more sensitive to variations in smooth muscle cell coupling. Given the same variations in g_{gap} , λ varies by as much as 13%.

2.4 Discussion

To study the conduction of vasomotor response along the AA, a phenomenon that is central to the coordination of the responses of individual cells, we have developed a multi-cell model for the rat AA. The model AA's myogenic response is based on

the assumption that changes in hydrostatic pressure induce changes in the activity of nonselective cation channels. The model was used to study the autoregulatory response of the AA, and the mechanism by which vasoconstriction initiated from local sites can spread upstream and downstream along the vessel. Through its myogenic response, the model AA maintained an approximately stable outflow pressure for a range of steady-state inflow pressure from 80 to 180 mmHg. Also, the model predicted pressure-radius relations (Fig. 2.2A) that are consistent with that obtained in the hydronephrotic rat kidney [106], and with those obtained for isolated rabbit AA, with and without the application of the smooth muscle relaxant papaverine, which abolishes autoregulation [49].

In addition to the above steady-state simulations, we studied the response of the model to oscillating inflow pressure. Simulation results suggest that, owing to the asymmetry in vasoconstriction and vasodilation response times, the AA may be able to sense systolic pressure and respond with a sustained vasoconstriction when systolic pressure is elevated (see Figs. 2.4B1 and 2.4B2). Similar results were obtained in previous modeling studies [27, 104, 168].

2.4.1 Conduction of vasomotor response

August Krogh once proposed that the mechanism by which a vasodilatory response propagates among the toes of the frog hind limb was provided by the innervation of blood vessels [89]. However, decades of studies in the regulation of microcirculatory blood flow has yielded a better understanding of the ultrastructural organization of the arteriolar networks, and an alternative explanation for the conduction of vasomotor response: electrotonic conduction of electrical signaling through the endothelial or smooth muscle cell layer. It has been demonstrated in cheek pouch arterioles that the propagation of vasoconstrictive or vasodilative response is coupled to variations in membrane potential [171, 167], which suggests that the conducted vasomotor

response results from the conduction of a electrical signal along the vessel, both upstream and downstream.

Given that the propagation of vasomotor response in arterioles does not appear to depend on flow-mediated changes (e.g., the increased production of NO induced by higher shear stress) or neural transmission, it is generally believed that vasomotor signal is conducted through the endothelial or smooth muscle cell gap junctions. Evidence supporting the role of gap junctions includes the observation that conducted vasomotor responses in hamster cheek pouch are abolished or attenuated with the application of putative gap junction uncouplers [143, 172]. Moreover, electron microscopy has demonstrated that neighboring endothelial and smooth muscle cells in renal vasculature [119], thoracic aorta [152], and iridial arterioles [67] are connected by gap junctions, which render these cells electrically and chemically coupled [12, 167, 142, 100, 118, 171, 172, 11, 67]. See Ref. [63] for a review on these issues.

When a depolarizing stimulus was applied to one of the AA cells, a local vasoconstrictive response was induced, and that vasomotor response was conducted along the vessel. Vasomotor responses decay with increasing distance from the stimulation site, with a faster decay in the upstream flow direction than downstream, as observed by Steinhausen et al. [155]. The mechanisms that account for a directional propagation of vasomotor response was previously not well understood. Steinhausen et al. proposed as potential factors the differences in vessel depths, in electrical conductance of the surrounding tissues, in vascular reactivity between upstream and downstream stimulate sites, in conduction of electrical current, and in transport of biochemical factors in the vascular lumen [155]. Our model results suggest that a depolarizing current reduces the dilation induced by the myogenic response of an AA smooth muscle cell at low pressures, particularly for the downstream cells. That effect shifts the balance between the myogenic response and the reduced tension force among the downstream AA cells in favor of the latter factor, thereby generating a slower decay

of the vasoconstrictive response downstream.

The model predicted that the downstream and upstream decays of vasomotor responses are approximated by exponential functions with length constants 340 and 121 μm , respectively. Steinhausen et al.[155] reported decay constants of 420 and 150 μm , respectively. Upstream decay length constants of $\sim 300\text{--}600$ μm were measured in renal microvasculature by Wagner et al. [165] for vasoconstriction caused by microapplication of KCl, and by Chen et al. [28] for tubuloglomerular feedback (TGF)-initiated vasoconstriction. The upstream decay length constant predicted by our model is smaller than Steinhausen et al. [155] but falls within the range measured in in Refs. [28, 165]. The discrepancy in length scales determined by our model and Steinhausen et al. may be attributed to the latter using a vascular tree that comprised mostly of interlobular artery [155]. Nonetheless, the length-scale ratios predicted by the model and in the experiments match. Given the preference for propagation downstream, myogenic activation of interlobular artery is likely to be more powerfully transmitted to downstream vascular segments.

2.4.2 Comparison with previous models

The multi-cell AA model of the present study is an extension of our previous AA cell model [27], which represents the response of both the smooth muscle cells and the endothelium along a very small segment of the AA, or one single cell. The AA cell model [27] was in turn based on a model for cerebral arterioles in cat that was developed by Gonzalez-Fernandez and Ermentrout [61], with appropriate adjustments in parameters. Consistent with the present study, the AA cell model [27] responded to a high-frequency pressure oscillations with a sustained constriction. The AA model of the present study was constructed by connecting instances of the AA cell model in series, with each cell model coupled to its neighbors through gap junctions, which allow the representation of electrotonic conduction along the AA. A fluid dynamics

model was included to relate fluid pressure, fluid flow, and tubular resistance. Also, some of the parameters of the AA cell model were adjusted to depend upon the location within the AA because of the decrease in intravascular pressure along the vessel.

Lush and Fray developed a mathematical model of the myogenic control of the AA [109] (hereafter referred to as the L&F model), and used that model to study the steady-state autoregulation of renal blood flow in the dog kidney. Their model computes steady-state renal blood flow assuming a balance of the distensive and constrictive forces acting on the AA. Similar to our model, the AA smooth muscle contraction in the L&F model is assumed to be initiated by pressure-induced changes in calcium permeability, and their model describes the effect of transmural pressure on calcium permeability, intracellular calcium concentration, and contractile activity. Because Lush and Fray focused on steady-state autoregulation, details of the kinetics of the AA ionic transport and muscle mechanics were not represented, nor was the asymmetry in the response times of the AA to pressure increase and decrease. Also, individual AA cells are not differentiated in the L&F model. Despite these differences, the L&F model and the present model predicted similar autoregulatory responses (compare fig. 4 in Ref. [109] and Fig. 2.2).

Secomb and co-workers developed a model of blood flow regulation [19, 2]. Their model's representations of the active contractile force and resulting muscle mechanics are similar to the L&F model, but the model by Secomb and co-workers represents also metabolic vasoactive and shear stress-dependent responses. Their model was formulated for both large and small arterioles, each with a different set of parameters.

Marsh et al. [112] also adopted the smooth muscle cell model of Gonzalez-Fernandez and Ermentrout [61] to study the interactions between AA myogenic response and TGF. However, as noted in a previous study [27], in Ref. [112] myogenic responses were generated only in response to oscillatory transmural pressure, whereas it has

long been observed that changes in mean pressure also induce myogenic responses [106]. In contrast, our model exhibits myogenic responses as a function of both pressure and its rate of change. Another difference is that the myogenic model in Ref. [112] represents only two AA segments. Thus, each submodel represents a rather long segment along the AA, whereas each of our AA cell submodel roughly corresponds to an AA cell. Both AA segments in Ref. [112] share the same model parameters; in contrast, based on the observation that the AA cells respond different external environments (e.g., intravascular fluid pressure), we adjusted some of the AA cell parameters based on their location within the AA.

2.4.3 Model limitations and future extensions

Because the model represents a series of AA and endothelial cells, some degree of simplification was necessary to keep computational costs low. Thus, the model adopts a phenomenological representation of certain details of the myogenic response. For example, to recapitulate the asymmetric constrictive and dilation kinetics similar to behaviors observed *in vitro*, the model myogenic mechanism represents asymmetric time delays, based on experimental measurements [106, 104], and assumes a rate-sensitive non-selective cation channels activation. While this model description yields predictions that are consistent with experimental observations [106, 104], potentially important details are neglected, including the possible involvement of ENaC channels in the initiation of the myogenic response, signaling pathways underlying the vascular smooth muscle constriction, or signaling mechanisms that modulate the myogenic response.

Fluid dynamics in the AA is represented as quasi steady-state Poiseuille flow, which assumes that the flow is laminar and through a long pipe with constant radius. Because the AA walls constrict and dilate, conditions for Poiseuille flow are only approximately satisfied, provided that the amplitude of the vasomotion is suf-

ficiently small, and the time-scale of the fluid dynamics is much faster than wall mechanics. A more realistic fluid model would be the Navier-Stokes equations, but the computations required for solving the Navier-Stokes equations are much more time-consuming.

Despite its limitations, the present AA model can be used as an essential component in models of integrated renal hemodynamic regulation. By coupling a number of AA models, one can investigate how vasomotor responses propagate among a vascular tree. And using an approach similar to Ref. [112], the AA model could then be combined with a model of glomerular filtration (e.g., Ref. [42]) and a model of the TGF mechanism (e.g., Ref. [91]), to study the interactions between the myogenic and TGF mechanisms in the context of renal autoregulation.

2.5 Appendix: Model equations and parameters

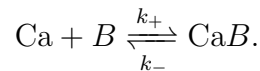
This appendix contains model equations that describe the ionic transport and mechanical properties of an AA smooth muscle cell [27], as well as a list of model parameters.

2.5.1 Ion transport and membrane potential

The smooth muscle cells of the AA can undergo contractions that are determined by the free cytosolic calcium concentration Ca . The sum of Ca and bound buffer $\text{Ca}B$ gives the total calcium concentration Ca_T , i.e.,

$$\text{Ca}_T = \text{Ca} + \text{Ca}B \tag{2.7}$$

The free cytosolic calcium and the unbound buffer B combine to yield $\text{Ca}B$ in a reversible reaction that can be represented by



Because the kinetics of the calcium-buffer system is substantially faster than other relevant membrane transporters, the above reaction is assumed to be at equilibrium. Thus,

$$\text{Ca}B = \frac{\text{Ca}B_T}{K_d + \text{Ca}}. \quad (2.8)$$

By differentiating Eq. (2.7) with respect to time and using Eq. (2.8), one obtains

$$\frac{d\text{Ca}_T}{dt} = \frac{d\text{Ca}}{dt} \left(1 + \frac{B_T K_d}{(K_d + \text{Ca})^2} \right).$$

The rate of change of Ca_T can be described by the following first-order kinetics:

$$\frac{d\text{Ca}_T}{dt} = -\frac{1}{z_{\text{Ca}}\beta V_{\text{cell}}F} g_{\text{Ca}} m_{\infty} (v - v_{\text{Ca}}) - k_{\text{Ca}} \text{Ca},$$

where V_{cell} is the cell volume; β is the fraction of cell volume occupied by the cytosol; F is the Faraday constant; $z_{\text{Ca}} = 2$ is the valence of the calcium ion; and k_{Ca} is the first-order rate constant for cytosolic calcium extrusion. m_{∞} is the equilibrium distribution of open calcium channel states, and is described as a function of membrane potential v [50, 96]:

$$m_{\infty}(v) = 0.5 \left(1 + \tanh \left(\frac{v - v_1}{v_2} \right) \right),$$

where v_1 is the voltage at which half of the channels are open, and v_2 determines the spread of the distribution.

The opening of potassium channels induces a transmembrane K^+ efflux, which polarizes the cell membrane. To represent the K^+ flux, we describe the rate of change of the fraction of K^+ channel open states, denoted n , by first-order kinetics [122]:

$$\frac{dn}{dt} = \lambda_n (n_{\infty}(v, \text{Ca}) - n),$$

where n_∞ denotes the equilibrium distribution of open K^+ channel states. The rate constant λ_n is given by

$$\lambda_n = \phi_n \cosh\left(\frac{v - v_3}{2v_4}\right),$$

where ϕ_n determines the rate at which the potassium channels open. This distribution depends on the membrane voltage v and the free cytoplasmic calcium concentration Ca :

$$n_\infty(v, Ca) = 0.5 \left(1 + \tanh\left(\frac{v - v_3}{v_4}\right) \right),$$

$$v_3 = -\frac{v_5}{2} \tanh\left(\frac{Ca - Ca_3}{Ca_4}\right) + v_6.$$

The potential v_3 , which determines the voltage at which half of the potassium channels are open, is a function of Ca ; v_4 and Ca_4 are measures of the spread of the distributions of n_∞ and v_3 , respectively.

2.5.2 Myosin phosphorylation

Oscillations in Ca vary the phosphorylation rate of the 20k-Da myosin light chains (MLC), which are involved in the formation of crossbridges between overlapping myosin and actin filaments. The formation of crossbridges causes smooth muscle contractions. Because the kinetics of that phosphorylation, which is calcium dependent, is much faster than other vasomotion processes considered here, we assume that the fraction of phosphorylated MLC to total MLC, denoted by ψ , is given by [136]

$$\psi = \frac{Ca^3}{Ca_m^3 + Ca^3},$$

where Ca_m is a constant. The phosphorylated myosin interacts with actin to form crossbridges and develop stress [84]. Let ω denote the fraction of crossbridges formed;

then we describe the net formation of crossbridges by means of the ordinary differential equation given by

$$\frac{d\omega}{dt} = k_\psi \left(\frac{\psi}{\psi_m + \psi} - \omega \right).$$

2.5.3 Vessel mechanics

Variations in the number of crossbridges induce variations in a contractile force, which in turn gives rise to variations in AA diameter. To simulate the resulting vasomotion, we consider the blood vessel to be a thick-walled cylinder. The motion of the vessel wall is driven, in part, by the transmural pressure, muscle activity, and wall deformation, which give rise to forces described below. Let r_i and r_o denote the inner and outer vessel radius, respectively. Let P denote the transmural pressure, and let x denote the average circumferential length, i.e., $x = \pi(r_i + r_o)$. The transmural pressure causes the vessel to relax or contract, which then gives rise to a tension force in the angular (θ) direction. That force, which we denote by f_P , is given by

$$f_P = \frac{1}{2}P \left(\frac{x}{\pi} - \frac{A}{x} \right),$$

where A , the wall cross-sectional area, is given by $A = \pi(r_o^2 - r_i^2)$ [61].

Wall deformation gives rise to additional stresses along the θ -direction of the wall. Let y and u be the circumferential lengths associated with the contractile and series elastic components, respectively. We assume that those stresses consist of the following components: a contractile component of length y , in series with an elastic component of length u ; these two components are in parallel with an elastic component of length $x = y + u$ (recall that x is the average circumference). We consider the resulting hoop forces on a surface S , which is bounded by the inner and outer radii of the vessel; S is assumed to be perpendicular to the angular (θ) direction, and to have unit length along the axial direction. Then, given the stresses

σ_x , σ_y , and σ_u (see below), the hoop forces on S of the i th AA smooth muscle cell are:

$$f_x^i = \xi^i w_e S \sigma_x^i, \quad f_y^i = \xi^i w_m S \sigma_y^i, \quad f_u^i = \xi^i w_m S \sigma_u^i, \quad (2.9)$$

where w_e and w_m are weights representing the contribution by the elastic and muscular components of the hoop forces, and ξ^i decreases linearly along the AA. The rate of change of the parallel elastic component's length is given by

$$\frac{dx}{dt} = \frac{1}{\tau} (f_P - f_x - f_u), \quad (2.10)$$

where τ is a pseudo-time constant associated with the wall internal friction.

For a given number of crossbridges, the velocity of the contractile component (y) is assumed to depend on the balance between the muscle load experienced by the contractile component, given by the elastic stress σ_u and the contractile stress σ_y . For $\sigma_u \leq \sigma_y$, the velocity is also proportional to phosphorylation level [43, 44, 125]. Thus, following Ref. [61], we have

$$\frac{d(y/x_0)}{dt} = -av'_{\text{ref}} \frac{\psi}{\psi(\text{Ca}_{\text{ref}})} \left(\frac{1 - \sigma_u/\sigma_y}{a + \sigma_u/\sigma_y} \right);$$

for $\sigma_u > \sigma_y$, the contractile component lengthens:

$$\frac{d(y/x_0)}{dt} = c \left(\exp \left(b \left(\frac{\sigma_u}{\sigma_y} - d \right) \right) - \exp(b(1 - d)) \right).$$

To approximate experimental measurements [44, 45, 46, 47, 124], the hoop stresses associated with the parallel elastic, contractile, and series elastic components, de-

noted by σ_x , σ_y , and σ_u , respectively, are given in Ref. [61] by

$$\sigma_x = x_3 \left(1 + \tanh \left(\frac{(x/x_0) - x_1}{x_2} \right) \right) + x_4 ((x/x_0) - x_5) - \quad (2.11)$$

$$- x_8 \left(\frac{x_6}{(x/x_0) - x_7} \right)^2 - x_9,$$

$$\sigma_y = \sigma_{y0} \frac{\exp \left(\frac{-((y/x_0) - y_0)^2}{2(y_1/((y/x_0) + y_2))^{2y_4}} \right) - y_3}{1 - y_3}, \quad (2.12)$$

$$\sigma_u = u_2 \exp(u_1(u/x_0)) - u_3, \quad (2.13)$$

where σ_{y0} is the reference stress that depends on the fraction of crossbridges ω :

$$\sigma_{y0} = \left(\frac{\sigma_{y0}^\#}{\sigma_0^\#} \right) \left(\frac{\psi_m + \psi(\text{Ca}_{\text{ref}})}{\psi(\text{Ca}_{\text{ref}})} \right) \omega.$$

On the right-hand side of Eq. (2.11), the first term represents the stiff collagen fibers that come into play for large expansions; the second term represents the compliant elastin fibers that play a role in smaller deformations; the third term represents the large stiffness that arises when the vessel radius is substantially reduced; and the fourth term serves to fit σ_x to experimental data [124].

2.5.4 Parameters

A large number of parameters are used in this model to describe the AA's geometrical dimensions, membrane transport properties, and muscle mechanical properties. The values of these parameters are given in Tables 2.3–2.7. Most of the parameters that describe the transport and mechanical properties of the AA smooth muscle cells are taken from Ref. [61] (with some modifications to account for the differences in physical dimensions and in dynamic behaviors between the cerebral arterioles modeled in Ref. [61] and the renal AA) and have previously been reported in Ref. [27].

Table 2.3: Afferent arteriole geometric dimensions.

Parameter	Value	Unit
A	1.38×10^{-6}	cm^2
L	303.00×10^{-4}	cm
N_{cell}	101	-
S	2.00×10^{-4}	cm^2
Δx	3.00×10^{-4}	cm

Table 2.4: Smooth muscle cell electrochemical parameters.

Parameter	Value	Unit
α	96.62×10^{15}	$\text{nM} \cdot \text{C}^{-1}$
B_T	10^5	nM
C	6.5	pF
Ca_3	400	nM
Ca_4	150	nM
Ca_m	277	nM
ϕ_n	0.925	s^{-1}
g_L/C	1.00	s^{-1}
g_K/C	4.00	s^{-1}
g_{Ca}/C	2.00	s^{-1}
g_{gap}/C	950	s^{-1}
$g_{\text{SMC-endo}}/C$	85	s^{-1}
K_d	10^3	nM
k_{Ca}	190	s^{-1}
v_1	-22.5	mV
v_2	25.0	mV
v_4	14.5	mV
v_5	8.00	mV
v_6	-15.0	mV
v_L	-70.0	mV
v_K	-95.0	mV
v_{Ca}	80.0	mV

Table 2.5: Arteriolar cell parameters.

Parameter	Value	Unit
$g_{\text{SMC-endo}}/C_e$	13.60×10^2	s^{-1}
$g_{\text{gap,e}}/C_e$	30.40×10^3	s^{-1}
C/C_e	16.0	-

Table 2.6: Smooth muscle cell mechanical parameters (I).

Parameter	Value	Unit
x_0	0.0150	cm
x_1	1.20	-
x_2	0.130	-
x_3	2.22	-
x_4	0.712	-
x_5	0.800	-
x_6	0.0100	-
x_7	0.139	-
x_8	0.890	-
x_9	9.05×10^{-3}	-
u_1	41.8	-
u_2	4.74×10^{-2}	-
u_3	5.84×10^{-2}	-
y_0	0.928	-
y_1	0.639	-
y_2	0.350	-
y_3	0.788	-
y_4	0.800	-

Table 2.7: Smooth muscle cell mechanical parameters (II).

Parameter	Value	Unit
a	0.281	-
b	5.00	-
c	0.0300	s^{-1}
d	1.30	-
k_ψ	0.250	s^{-1}
ψ_m	0.300	-
ω_{ref}	0.685	-
ψ_{ref}	0.599	-
ν_{ref}	0.240	s^{-1}
$\sigma_{y0}^\#$	1.46×10^7	$\text{dyn}\cdot\text{cm}^{-2}$
$\sigma_0^\#$	1.69×10^7	$\text{dyn}\cdot\text{cm}^{-2}$
τ	0.500	$\text{dyn}\cdot\text{s}\cdot\text{cm}^{-1}$
w_e	1/9.00	-
w_m	0.700	-

Control and Modulation of Fluid Flow

3.1 Introduction

For an animal's kidney to function normally, glomerular filtration rate must stay within a narrow window despite changes in arterial pressure. That goal is accomplished by autoregulatory mechanisms. One such mechanism is the *myogenic response*, in which the afferent arteriole dilates or constricts in response to several signals, including blood pressure and tubuloglomerular signal from macula densa [37, 73, 79].

The afferent arteriole arises from the renal artery and branches into glomerular capillaries. A portion of the blood plasma delivered by the afferent arteriole is filtered through the glomerulus into the nephron. Via the myogenic response, vascular smooth muscles of the afferent arteriole respond to increased intraluminal pressure or stretch with active force development, thereby enabling the vessel to constrict. In the arteriolar system, the myogenic response is thought to be important for local autoregulation of blood flow and regulation of capillary pressure [104, 108].

Like many other small arteries and arterioles, the renal afferent arteriole exhibits

spontaneous rhythmic activity, a.k.a. vasomotion [149]. Vasomotion is *spontaneous* in the sense that vascular tone oscillates independently of heart beat, innervation, or respiration. The driving stimulus of vasomotion is believed to be the oscillations intrinsically appearing in the electrical activity of the cells that form the arteriolar walls [129, 73]. Vasomotion is blocked by the same blockers (such as calcium and potassium membrane channels blockers) that eliminate the myogenic response; thus, the two are believed to be functionally related [56, 129].

Another renal autoregulatory mechanism is the *tubuloglomerular feedback* (TGF) system, which is a negative feedback loop in which the chloride ion concentration is sensed downstream in the nephron by the macula densa cells. Experiments in rats have demonstrated that TGF may induce regular oscillations in nephron flow and related variables (e.g., intratubular fluid pressure and solute concentrations) [75, 97]. In the case of spontaneously hypertensive rats, TGF-mediated oscillations can be irregular and appear to have characteristics of chaos [71, 173]. We have previously studied the signal transduction process along the loop of Henle [92, 93]. That transduction process involves the transformation of variations in tubular fluid flow rate into chloride ion concentration variations in tubular fluid alongside the macula densa. Owing to the nonlinearity of that transformation, harmonic frequencies are generated and contribute to the complexity of TGF-mediated oscillations. However, those models do not represent the afferent arteriole, which is the effector of both the myogenic response and TGF.

In this study, we have developed a mathematical model of renal hemodynamics in the rat kidney. This is the first mathematical model that combines (i) detailed representation of ionic transport, membrane potential, and contraction of the afferent arteriole smooth muscle cells; (ii) myogenic responses induced by steady pressure steps and oscillatory pressure variations; (iii) glomerular filtration; and (iv) detailed representation of tubular fluid flow and Cl^- transport. Using this model, we investi-

gated the extent to which autoregulation is attained by the myogenic response, and we studied the signal transduction properties of the vascular and nephron segments, and the extent to which they generate or suppress harmonic frequencies. A better understanding of those properties should clarify the roles of those segments in the regulation of single nephron glomerular filtration rate (SNGFR) and of water and electrolyte delivery to the distal nephron. Model results suggest that heterodyning may contribute to a low frequency oscillation that have been seen *in vivo* and *in vitro* [80, 81, 151], and that is slower than the responses of the constituent components represented in this model.

3.2 Mathematical Model

To model hemodynamics control in the rat kidney, we developed a model that combines: (i) an afferent arteriole model previously developed by us [145]; (ii) a glomerular filtration model developed by Deen et al. [42]; (iii) a renal tubule model previously developed by us [93]. A schematic diagram for the combined model is given in Fig. 3.1.

3.2.1 Afferent arteriole submodel

We represent an *afferent arteriole* segment of length L_{AA} . The submodel consists of a series of N_{AA} vascular smooth muscle cells that form the vascular wall and an endothelial layer. Smooth muscle cells communicate through electrical currents passing between them and also through the endothelium. Each smooth muscle cell represents membrane potential, cytosolic Ca^{2+} dynamics, cross-bridges cycling, and muscle mechanics. The model smooth muscles also incorporate the myogenic response, which enables the vessel to constrict when luminal pressure increases, and vice versa. Luminal blood flow is assumed to be pressure driven. A detailed description of the submodel and a complete set of model equations can be found in Refs. [27, 145].

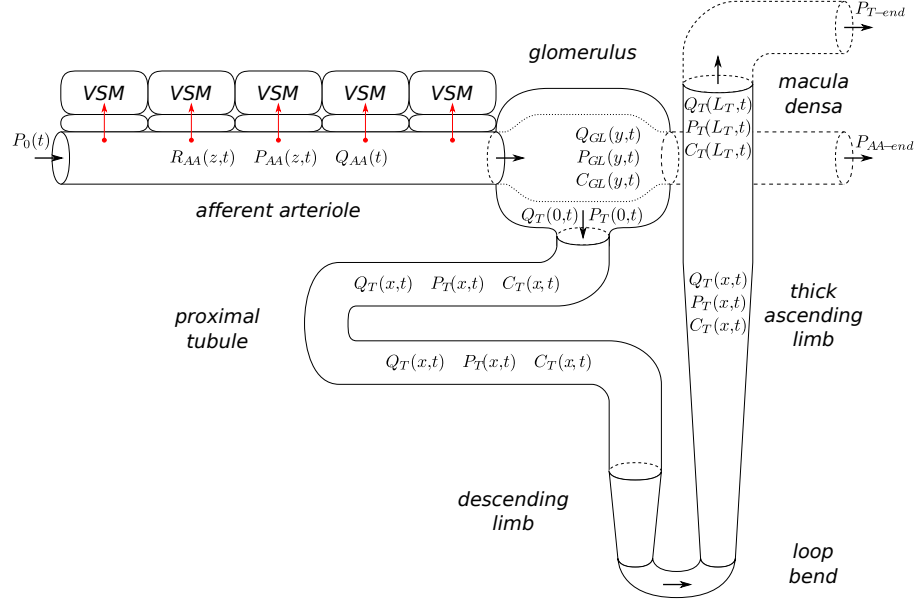


FIGURE 3.1: Schematic diagram of the model nephron. Afferent arteriole is shown with a reduced number of vascular smooth muscles (VSM). Arrows indicate myogenic response (red), and key fluid flow variables (black).

Below we summarize key model equations. Model smooth muscle cells are linearly indexed with i , where i ranges from 1 (cell proximal to the renal artery) to N_{AA} (cell proximal to the glomerulus).

The rates of change of the membrane potentials of the smooth muscle cell $v_m^i(t)$ and the associated endothelial compartment $v_e^i(t)$ are given by

$$C_m \frac{dv_m^i(t)}{dt} = -I_L(v_m^i) - I_K(v_m^i, n^i) - I_{Ca}(v_m^i) + I_{m-m}(v_m^i, v_m^{i-1}, v_m^{i+1}) + I_{m-e}(v_m^i, v_e^i) + I_{myo}^i, \quad (3.1)$$

$$C_e \frac{dv_e^i(t)}{dt} = -I_{m-e}(v_m^i, v_e^i) + I_{e-e}(v_e^i, v_e^{i-1}, v_e^{i+1}), \quad (3.2)$$

where C_m and C_e denote the smooth muscle and endothelial cell capacitances, respectively. Equation (3.1) incorporates the leak current I_L , ionic fluxes mediated by voltage-gated and voltage-calcium-gated Ca^{2+} and K^+ channels, denoted I_{Ca} and I_K , gap-junction communication between adjacent smooth muscle cells I_{m-m} , current

between smooth muscles and the endothelial compartment I_{m-e} , and a current induced by the myogenic response I_{myo}^i [145]. Equation (3.2) describes endothelial cell membrane potential in terms of intercellular current between smooth muscle and endothelial cells, and between adjacent endothelial cell compartments. These currents (except for I_{myo} , see below) are given by

$$I_L(v_m) = g_L(v_m - v_L), \quad (3.3)$$

$$I_K(v_m, n) = g_K n(v_m - v_K), \quad (3.4)$$

$$I_{Ca}(v_m) = g_{Ca} m_\infty(v_m)(v_m - v_{Ca}), \quad (3.5)$$

$$I_{m-m}(v_m^i, v_m^{i-1}, v_m^{i+1}) = g_{m-m}(v_m^{i-1} - 2v_m^i + v_m^{i+1}), \quad (3.6)$$

$$I_{e-e}(v_e^i, v_e^{i-1}, v_e^{i+1}) = g_{e-e}(v_e^{i-1} - 2v_e^i + v_e^{i+1}), \quad (3.7)$$

$$I_{m-e}(v_m, v_e) = g_{m-e}(v_e - v_m). \quad (3.8)$$

Boundary conditions are required to complete Eqs. (3.6) and (3.7). For instance, consider Eq. (3.6). At $i = 1$, we assume that smooth muscle cells further than a distance of L_{AA} (length of the model afferent arteriole) upstream are synchronized so $I_{m-m} = 0$, and we assume that I_{m-m} decreases linearly to zero along that segment ($-L_{AA} \leq z < 0$), which implies that $v_m^0 = v_m^1 - (v_m^2 - v_m^1)(N_{AA} - 1)/N_{AA}$. Analogous boundary conditions are imposed at $i = N$ and on Eq (3.7).

The gating of K^+ channels $n^i(t)$ is described by

$$\frac{dn^i(t)}{dt} = \phi_n \cosh\left(\frac{v_m^i - v_3(c^i)}{2v_4}\right)(n_\infty(v_m^i, c^i) - n^i), \quad (3.9)$$

where c^i denotes free cytosolic Ca^{2+} concentration. The potential v_3 , which determines the voltage at which half of the K^+ channels are open, depends on free cytosolic Ca^{2+} : $v_3(c) = v_6 + 0.5v_5 \tanh((c - c_3)/c_4)$. The equilibrium distribution of open K^+ channels is given by

$$n_\infty(v_m, c) = \frac{1}{2} \left(1 + \tanh\left(\frac{v_m - v_3(c)}{v_4}\right) \right). \quad (3.10)$$

The gating of the Ca^{2+} channels is assumed to be at equilibrium

$$m_\infty(v_m) = \frac{1}{2} \left(1 + \tanh \left(\frac{v_m - v_1}{v_2} \right) \right). \quad (3.11)$$

The Ca^{2+} current I_{Ca} induces changes in free cytosolic Ca^{2+} concentration $c^i(t)$, which is given by

$$\frac{dc^i(t)}{dt} = \frac{(K_d + c^i)^2}{(K_d + c^i)^2 + K_d B_T} (-\alpha_{Ca} I_{Ca}(v_m^i) - k_{Ca} c^i). \quad (3.12)$$

The above equation represents Ca^{2+} influx through the membrane channels, and models the extrusion as a first-order decay. The nonlinear rate constant is obtained by assuming that free cytosolic Ca^{2+} is in equilibrium with various buffers; for more details see Refs. [27, 61].

An important characteristic of the afferent arteriole's myogenic response is the asymmetry in its response times for vasoconstriction and vasodilation [106, 104]: the initial delay in the activation of a pressure-dependent vasoconstriction was observed to be ~ 0.3 s, with the time-profile of the response approximated by an exponential having a time constant of 4 s. In contrast, vasodilation exhibits a longer initial delay of ~ 1 s, with a response that can be approximated by two exponentials having time constants of 1 and 14 s, respectively. That response time asymmetry may be attributable to the independently regulated pathways for constriction and dilation; however, the details involved are not well understood and are beyond the scope of this work. To represent the response time asymmetry, we adopt an empirical approach and model the dynamics of $I_{myo}^i(t)$ by

$$\frac{dI_{myo}^i(t)}{dt} = \begin{cases} -k_{inc}(I_{myo}^i - \bar{I}_{myo}^i(t, P_{AA}^i(t - \tau_m))), & \text{if } \frac{dP_{AA}^i(t - \tau_m)}{dt} \geq 0, \\ -k_{dec}(I_{myo}^i - \bar{I}_{myo}^i(t, P_{AA}^i(t - \tau_m))), & \text{if } \frac{dP_{AA}^i(t - \tau_m)}{dt} < 0, \end{cases} \quad (3.13)$$

where $P_{AA}^i(t)$ denotes luminal pressure, $\bar{I}_{myo}^i(t, P_{AA})$ denotes target current, given by

$$\bar{I}_{myo}^i(t, P_{AA}^i) = C_m F_{myo}(P_{AA}^i - \bar{P}_{AA}^i), \quad (3.14)$$

Table 3.1: Parameters defining the cubic spline $F_{myo}(p)$ for $-20 \leq p \leq 90$ mmHg.

k	p_k	$F_{myo}(p_k)$	$F'_{myo}(p_k)$
-	mmHg	mV·s ⁻¹	mV·s ⁻¹ ·mmHg ⁻¹
1	-20.0	-2.84	0.00
2	-10.0	-2.26	0.05
3	0.00	-0.46	0.24
4	10.0	2.40	0.34
5	20.0	6.01	0.38
6	30.0	9.85	0.39
7	40.0	13.75	0.39
8	50.0	17.60	0.38
9	60.0	21.38	0.39
10	70.0	25.36	0.41
11	80.0	29.50	0.46
12	90.0	33.75	0.00

where C_m is the cell capacitance. The reference pressure \bar{P}_{AA}^i is the pressure that the i -th smooth muscle segment is normally exposed to, which decreases linearly from 100 mmHg to 50 mmHg along the vessel. For $-20 \leq p \leq 90$ mmHg, $F_{myo}(p)$ is the piecewise cubic polynomial, with its values $F_{myo}(p_k)$ and slopes $F'_{myo}(p_k)$ at points p_k displayed in Table 3.1 for $k = 1, \dots, 12$. For $p < -20$ mmHg, $F_{myo}(p)$ is set to $F_{myo}(p_1)$, and for $p > 90$ mmHg to $F_{myo}(p) = F_{myo}(p_{12})$. The different rate constants k_{inc} and k_{dec} in Eq. (3.13), corresponding to pressure increase and decrease, yield a faster vasoconstrictive response compared to vasodilation. The response delay τ_m in Eq. (3.13) is set to 0.3 s for increasing pressure, and to 1 s for decreasing pressure [106, 104].

Free cytosolic Ca^{2+} facilitates phosphorylation and cross-bridges formation that results in the development of tension in the vascular wall. Let $\omega^i(t)$ denote the fraction of cross-bridges formed. The rate of change of $\omega^i(t)$ is given by

$$\frac{d\omega^i(t)}{dt} = k_\psi \left(\frac{\psi(c^i)}{\psi(c^i) + \psi_M} - \omega^i \right), \quad (3.15)$$

where $\psi(c) = c^3/(c_M^3 + c^3)$ is the phosphorylation level; for details see [27, 61].

Muscle mechanics for each smooth muscle segment are represented by a modified Maxwell model, where a viscous component, an elastic component of length $x_c^i(t)$, and a contractile component are connected in parallel. Further, the contractile component consists of a contractile element of length $y_c^i(t)$ and an elastic element of length $u_c^i(t) = x_c^i(t) - y_c^i(t)$, which are connected in series. The rate of contraction of the contractile element is

$$\frac{1}{x_c^0} \frac{dy_c^i(t)}{dt} = \begin{cases} c_c \left(\exp(b_c(\sigma_u/\sigma_y - d_c)) - \exp(b_c(1 - d_c)) \right), & \frac{\sigma_u(u_c^i)}{\sigma_y(y_c^i)} > 1, \\ -\nu_{ref} \frac{\psi(c^i)}{\psi_{ref}} a_c \frac{1 - \sigma_u(u_c^i)/\sigma_y(y_c^i)}{a_c + \sigma_u(u_c^i)/\sigma_y(y_c^i)}, & \frac{\sigma_u(u_c^i)}{\sigma_y(y_c^i)} \leq 1, \end{cases} \quad (3.16)$$

and the rate of change of the overall muscle circumferential length is

$$\frac{dx_c^i(t)}{dt} = \frac{1}{\tau_c} \left(f_P(x_c^i, P_{AA}^i(t)) - f_x(x_c^i) - f_u(u_c^i) \right). \quad (3.17)$$

That is, muscle tone is determined by the forces exerted by the hoop stress developed by the elastic and contractile components, which can be found in Ref. [61, 145]. The force developed by transmural pressure is given by $f_P(x_c, P_{AA}) = P_{AA} R_{AA}(x_c)$, with the pressure exterior to the vascular wall assumed to be zero. If muscles are assumed to be incompressible, then luminal radius $R_{AA}^i(t)$ is related to circumferential length by $R_{AA}^i(t) = (x_c^i(t)/\pi - A/x_c^i(t))/2$, where A is muscle cross-sectional area.

Luminal fluid flow is described as quasi-steady Poiseuille flow

$$\frac{\partial P_{AA}(z, t)}{\partial z} = \frac{8\mu_{AA}}{\pi R_{AA}^4(z, t)} Q_{AA}(t), \quad 0 \leq z \leq L_{AA}. \quad (3.18)$$

Inflow pressure at $z = 0$, denoted $P_0(t)$, is assumed known *a priori*. The model arteriole segment is assumed to be connected in-series to a fixed downstream resistor (Ω_{AA}), with outflow pressure P_{AA-end} assumed constant. Volumetric blood flow rate

$Q_{AA}(t)$ is given by

$$Q_{AA}(t) = \frac{P_0(t) - P_{AA-end}}{16\mu_{AA}L_{AA}/\pi} \left(\Omega_{AA} + \int_0^{L_{AA}} \frac{dz}{R_{AA}^4(z,t)} \right)^{-1}, \quad (3.19)$$

where μ_{AA} is luminal fluid viscosity. Equation (3.19) assumes that volumetric blood flow rate is uniform throughout the arteriole and the downstream resistor.

3.2.2 Glomerular filtration submodel

To model *glomerular filtration*, we adopt a model developed by Deen et al. [42]. The glomerulus is modeled as a single capillary extending from $y = 0$ to $y = L_{GL}$, which corresponds to the connections with the afferent and efferent arterioles, respectively. Let $Q_{GL}(y, t)$ and $C_{GL}(y, t)$ denote the volumetric plasma flow rate and plasma protein concentration, respectively. Conservation of plasma mass implies that

$$\frac{\partial Q_{GL}(y, t)}{\partial y} = -K_f \left(P_{GL}(y, t) - P_T(0, t) - \pi(y, t) \right), \quad (3.20)$$

where K_f is the filtration coefficient, $P_{GL}(y, t)$ is the hydrostatic pressure,

$$\pi(y, t) = \alpha_{GL1}C_{GL}(y, t) + \alpha_{GL2}C_{GL}^2(y, t) \quad (3.21)$$

is the colloidal osmotic pressure inside the glomerular capillaries, and $P_T(0, t)$ is the proximal tubule inflow pressure (predicted by the tubule submodel, below). We assume a linear pressure decrease along the glomerular capillary

$$P_{GL}(y, t) = P_{AA}(L_{AA}, t) - y \frac{\Delta P_{GL}}{L_{GL}}, \quad (3.22)$$

where ΔP_{GL} is a constant, and $P_{AA}(L_{AA}, t)$ is the pressure at the end of the afferent arteriole. Conservation of protein mass yields $C_{GL}(y, t)Q_{GL}(y, t) = C_{GL}(0, t)Q_{GL}(0, t)$, which together with Eq. (3.20) results in

$$\frac{\partial C_{GL}(y, t)}{\partial y} = \frac{K_f}{Q_{GL}(0, t)} \frac{C_{GL}^2(y, t)}{C_{GL}(0, t)} \left(P_{GL}(y, t) - P_T(0, t) - \pi(y, t) \right). \quad (3.23)$$

The inflow plasma protein concentration is fixed at $C_{GL}(0, t) = 5.5$ g/dl. The inflow rate is

$$Q_{GL}(0, t) = (1 - Ht)Q_{AA}(t), \quad (3.24)$$

where $Q_{AA}(t)$ is the volumetric flow rate delivered by the afferent arteriole, given in Eq. (3.19), and Ht is the hematocrit. By integrating Eq. (3.23), one obtains $C_{GL}(L_{GL}, t)$, which is used to compute $Q_{GL}(L_{GL}, t)$ from the conservation of plasma mass. Single nephron glomerular filtration rate is then given by

$$Q_F(t) = Q_{GL}(0, t) - Q_{GL}(L_{GL}, t). \quad (3.25)$$

3.2.3 Renal tubule submodel

The *tubule submodel* represents a proximal tubule and a short loop of Henle, which consists of a descending limb and an ascending limb. The model tubule spans from $x = 0$ to $x = L_T$, where $L_T = 1.58$ cm, with the proximal tubule spanning the initial 1 cm and the thick ascending limb the terminal 0.5 cm. Along the tubule, the model predicts fluid pressure $P_T(x, t)$, fluid flow rate $Q_T(x, t)$, and fluid Cl^- concentration $C_T(x, t)$, which is believed to be a key signal for the tubuloglomerular feedback mechanism (not represented in this study). The tubular walls are assumed to be compliant, with a radius that depends passively on transmural pressure gradient

$$R_T(x, P_T(x, t)) = \alpha_T(x)(P_T(x, t) - P_{T,ext}) + \beta_T(x), \quad (3.26)$$

where $P_{T,ext}$ is the extratubular pressure, $\alpha_T(x)$ characterizes tubular compliance, and $\beta_T(x)$ is the unpressurized radius.

Tubular fluid is assumed to be pressure-driven. At the entrance of the model tubule (i.e., $x = 0$), flow rate equals the glomerular filtration rate $Q_F(t)$ (predicted by the glomerular filtration submodel, Eq. (3.25)). The end of the model tubule (i.e., $x = L_T$) is connected in series to a downstream resistor (Ω_T) with the end-pressure fixed at P_{T-end} .

The proximal tubule and the initial segment of the descending limb are water permeable. Taking into account transmural water flux, denoted by $\Phi_T(x, t)$, pressure and flow rate along the model tubule are given by

$$\frac{\partial P_T(x, t)}{\partial x} = -\frac{8\mu_T}{\pi R_T^4(x, P_T(x, t))} Q_T(x, t), \quad (3.27)$$

$$\frac{\partial Q_T(x, t)}{\partial x} = -2\pi R_T(x, P_T(x, t)) \frac{\partial R_T(x, P_T(x, t))}{\partial P_T} \frac{\partial P_T(x, t)}{\partial t} - \Phi_T(x, t). \quad (3.28)$$

It has been observed experimentally that along the proximal tubule increases in filtration rate incur a concomitant increase in proximal reabsorption [141]; such proportional changes are called glomerular-tubular balance [59]. Micropuncture experiments have shown that $\sim 2/3$ of the water and Cl^- are reabsorbed along the proximal convoluted tubules. Thus, with a base-case glomerular filtration rate of 30 nl/min (denoted Q_{T_0}), water flow rate into the proximal straight tubule is 10 nl/min. Given these considerations, the transmural water flux term $\Phi_T(x, t)$ is given as a step-like function, constructed so that the model predicts a steady-state water flow rate that is consistent with the above measurements and that is ~ 7.0 nl/min at the loop bend [93]:

$$\Phi_T(x, t) = \frac{Q_F(t)}{Q_{T_0}} \Phi_{T,base}(x), \quad (3.29)$$

To compute model solutions, Eqs. (3.27) and (3.28) were combined to eliminate Q_T , yielding the PDE

$$\begin{aligned} 2\alpha_T(x) \frac{\partial P_T(x, t)}{\partial t} &= \frac{R_T^2(x, P_T(x, t))}{2\mu_T} \frac{\partial R_T(x, P_T(x, t))}{\partial x} \frac{\partial P_T(x, t)}{\partial x} \\ &+ \frac{R_T^3(x, P_T(x, t))}{8\mu_T} \frac{\partial^2 P_T(x, t)}{\partial x^2} + \frac{\Phi_T(x, t)}{\pi R_T(x, P_T(x, t))}. \end{aligned} \quad (3.30)$$

Equation (3.30) was solved simultaneously with Eq. (3.27) for P_T and Q_T . Boundary conditions for the system are $Q_T(0, t) = Q_F(t)$, and $Q_T(L_T, t) = (P_T(L_T, t) -$

$P_{T-end})/\Omega_T$, where P_{T-end} and Ω_T denote the end pressure and downstream resistance, respectively. Micropuncture studies in rat [32] suggests a passive dependence of distal tubule resistance on tubular pressure. Thus, the model assumes a sigmoidal dependence of Ω_T on distal pressure, given by

$$\Omega_T = \Omega_{T,ref} \left(1 - \tanh(s_{\Omega,T}(\bar{P}_T - \bar{P}_{T,ref})) \right) \quad (3.31)$$

where \bar{P}_T is the average of $P_T(L_T, t)$ and P_{T-end} , and $\bar{P}_{T,ref}$ is a constant reference pressure.

Chloride ion (Cl^-) concentration is given by conservation of mass

$$\begin{aligned} R_T^2(x, P_T(x, t)) \frac{\partial C_T(x, t)}{\partial t} &= -2R_T(x, P_T(x, t)) C_T(x, t) \frac{\partial}{\partial t} R_T(x, P_T(x, t)) \\ &- \frac{1}{\pi} \frac{\partial}{\partial x} (Q_T(x, t) C_T(x, t)) \\ &- 2R_{T,ss}(x) \left(\frac{V_{max}(x) C_T(x, t)}{K_M + C_T(x, t)} + \kappa(x) (C_T(x, t) - C_{T,ext}(x)) \right) \end{aligned} \quad (3.32)$$

where $R_{T,ss}(x, t)$ is the steady-state tubular radius, and $C_{T,ext}(x)$ is the extratubular (interstitial) Cl^- concentration, which is set to 115 mM along the cortex and increases linearly along the cortico-medullary axis to 275 mM at the outer-inner medullary boundary. The first term inside the large pair of parentheses corresponds to active solute transport characterized by Michaelis-Menten-like kinetics of maximum active transport rate $V_{max}(x)$ and Michaelis constant K_M ; the other term represents transepithelial diffusion, characterized by transmural Cl^- permeability $\kappa(x)$. Fluid entering the proximal tubule is assumed to have constant Cl^- concentration 115 mM.

3.2.4 Parameters and numerical method

Parameter values for the afferent arteriole and tubule submodels can be found in Refs. [145, 93]. Parameters that have not been previously reported or differ from

values in Refs. [145, 93], as well as parameters for the glomerular filtration submodel, are summarized in Table 3.2.

To compute numerical solutions for the model equations, we first discretized the model equations in space. For the model afferent arteriole, we computed model solution at locations $z^i = (i - \frac{1}{2})h_{AA}$, for $i = 1, \dots, N_{AA}$ and $h_{AA} = L_{AA}/N_{AA}$. Each grid point z^i represents a smooth muscle cell model. For the model tubule, we computed model solution at $x^i = (i-1)h_T$, for $i = 1, \dots, N_T$ and $h_T = L_T/(N_T - 1)$. A uniform spatial grid was not used for the glomerular filtration model, as explained below. Only the tubule submodel includes PDEs, namely (3.30) and (3.32); the afferent arteriole and glomerular filtration submodels includes ODEs, in time or space only. The PDEs of the tubule submodel were first discretized in space using the centered difference method adopted in Ref. [91]. The resulting system of coupled ODEs was integrated in time using an adaptive time-stepping method based on numerical differential formulae (`matlab ode15s`). During each time step, the afferent arteriole flow Eq. (3.18), and glomerular protein conservation Eq. (3.20) must be integrated in space. An adaptive Runge-Kutta method (RK45) was used to integrate Eq. (3.23), whereas Eq. (3.18) was numerically integrated using the Trapezoidal rule. An adaptive method was not used for the latter so that the fluid pressure is known at the locations of the smooth muscle cells. Note that the myogenic response, Eq. (3.13), involves delay. Because a variable time-stepping method was used, model solution may not have been computed at time $t_n - \tau_m$, and thus the delayed values $P_{AA}^i(t_n - \tau_m)$ and $dP_{AA}^i(t_n - \tau_m)/dt$ may not be known. In that case, their values were approximated by linear interpolation. Due to the interpolation used in the approximation of the delayed values, the resulting numerical method is limited to second order temporal accuracy.

In the numerical discretization, we set N_{AA} and N_T to 101 and 543, respectively, and we constrained the time-step not to exceed 0.3 s, which is the shorter delay τ_m

Table 3.2: Model parameters not reported in Refs. [145, 93]

AA	a_c	2.81	-
	w_e	0.17	-
	μ_{AA}	16.0	cP
GL	K_f	2.07	nl·min ⁻¹ ·mmHg ⁻¹
	ΔP_{GL}	3.02	mmHg
	Ht	0.45	-
	α_{GL1}	1.63	mmHg·dl·g ⁻¹
	α_{GL2}	0.29	mmHg·dl ² ·g ⁻²
	L_{GL}	1	-
TB	L_T	1.58	cm
	μ_T	0.67	cP
	P_{T-end}	2.00	mmHg
	$\Omega_{T,ref}$	0.71	mmHg·min·nl ⁻¹
	$s_{\Omega,T}$	0.86	mmHg ⁻¹
	$\bar{P}_{T,ref}$	4.5	mmHg
	$\Phi_{T,base,PCT}$	0.02	nl·min ⁻¹ ·cm ⁻¹
	$\Phi_{T,base,PST}$	0.05	nl·min ⁻¹ ·cm ⁻¹
	$\kappa_{PST,PCT}$	0.60	$\mu\text{m}\cdot\text{s}^{-1}$
	$\kappa_{DL,TAL}$	0.40	$\mu\text{m}\cdot\text{s}^{-1}$
	$V_{max,PCT}$	8.40	nmol·cm ⁻² ·s ⁻¹
	$V_{max,PST,DL}$	0.0	nmol·cm ⁻² ·s ⁻¹
	$V_{max,TAL}$	18.15	nmol·cm ⁻² ·s ⁻¹

associated with the vasoconstrictive response.

As in Ref. [93], the profiles $\alpha_T(x)$, $\beta_T(x)$, $\Phi_{T,base}(x)$, $R_{T,ss}(x)$, $V_{max}(x)$, $\kappa(x)$, and $C_{T,ext}(x)$ are given as piecewise functions. To avoid numerical errors that may arise from using a centered finite-difference method to compute the derivatives of discontinuous functions, we replaced them by appropriate smooth approximations.

3.3 Results

3.3.1 Base-case spatiotemporal behavior

Using base-case parameters and a fixed afferent arteriole inflow pressure of $P_0(t) = 100$ mmHg, we computed fluid pressure, fluid flow rate, and luminal radius along the model vessel and nephron, and we also computed Cl^- concentration along the

Table 3.3: Time-averaged base-case predictions at steady afferent arteriole inflow pressure of 100 mmHg. P_0 and P_D denote afferent arteriole entrance and exit pressure, respectively. Subscripts T , LB , and MD denote tubular entrance, loop bend, and macula densa, respectively.

P_0	100.00	mmHg
P_D	49.87	mmHg
Q_{AA}	319.27	nl·min ⁻¹
P_T	13.02	mmHg
P_{LB}	8.87	mmHg
P_{MD}	7.03	mmHg
Q_T	30.07	nl·min ⁻¹
Q_{LB}	7.16	nl·min ⁻¹
Q_{MD}	7.16	nl·min ⁻¹
C_T	115.00	mM
C_{LB}	250.41	mM
C_{MD}	32.15	nM

proximal tubule and loop of Henle. Model variables associated with the afferent arteriole exhibit spontaneous limit-cycle oscillations (vasomotion): the interactions of Ca^{2+} and K^+ fluxes, which are mediated by voltage-gated and voltage-calcium-gated channels, respectively, give rise to periodicity in the transport of those two ions. This results in time-periodic variations in cytoplasmic Ca^{2+} concentration, phosphorylation, and cross-bridges formation with the attending muscle stress, similar to results obtained in previous modeling studies [61, 27, 145]. Periodic variations in vascular luminal radius translate into variations in vascular resistance, fluid pressure, fluid flow, glomerular filtration rate, and eventually, tubular flow and solute transport. Figure 3.2 depicts the time courses of fluid pressure, and fluid flow at the entrance, middle, and exit of the afferent arteriole, as well as fluid pressure, fluid flow, and tubular fluid Cl^- concentration at the entrance of the proximal tubule, loop bend, and macula densa. Time averaged values of model’s predictions are summarized in Table 3.3.

Snapshots in time of pressure, flow rate, and Cl^- concentration are shown in

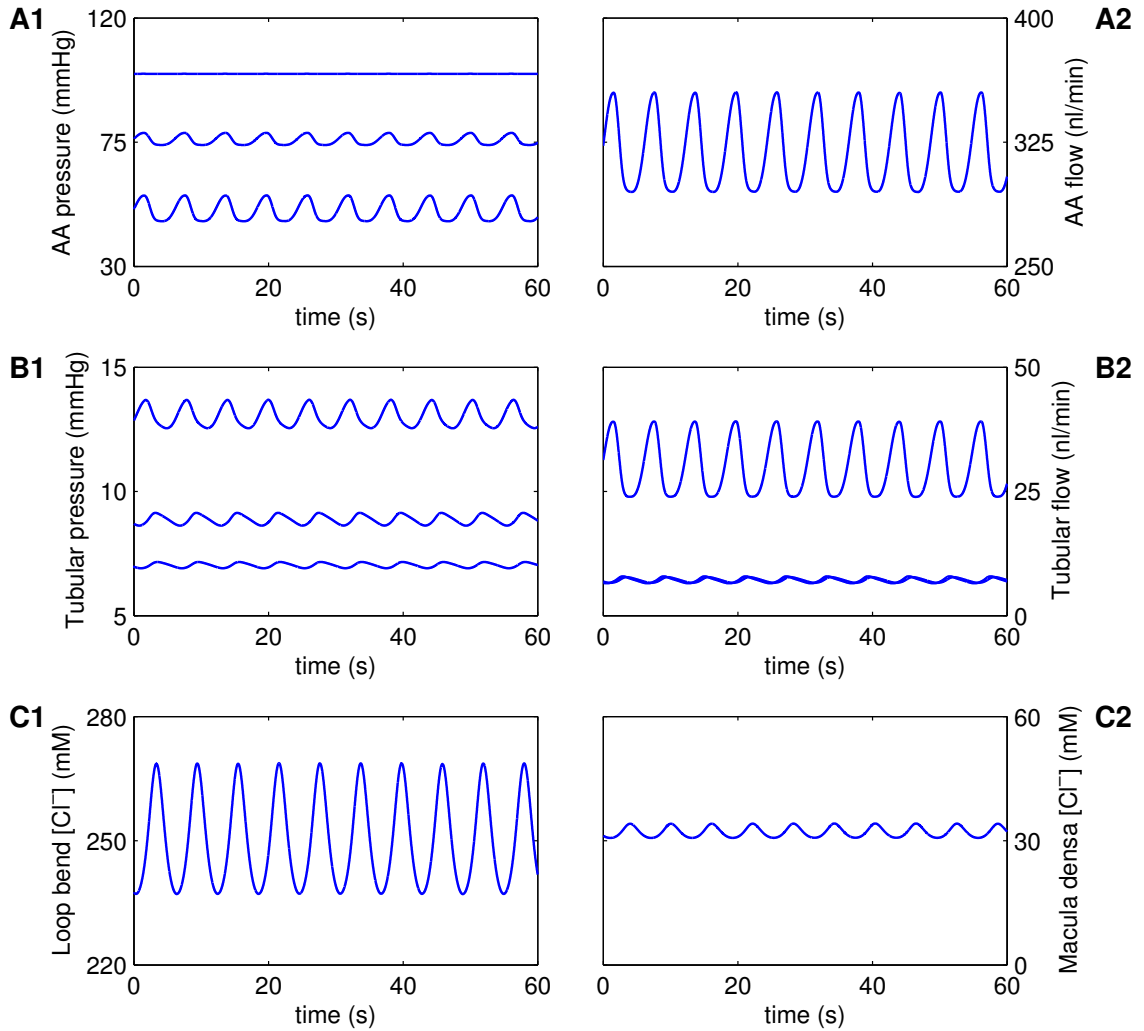


FIGURE 3.2: Base-case temporal predictions. A1, A2: pressure and flow rate in the afferent arteriole (AA); B1, B2: pressure and flow rate along the proximal tubule and loop of Henle; C1, C2: tubular fluid Cl^- concentration at loop bend and macula densa, respectively.

Fig. 3.3. Flow rate along the afferent arteriole is constant, which results in an approximately linear decrease in fluid pressure, whereas flow rate decreases along the proximal tubule and loop of Henle as determined by the outward-directed water flux term $\Phi_T(x, t)$. Chloride concentration along the proximal tubule remains almost flat, increases along the descending limb and then progressively decreases along the thick ascending limb.

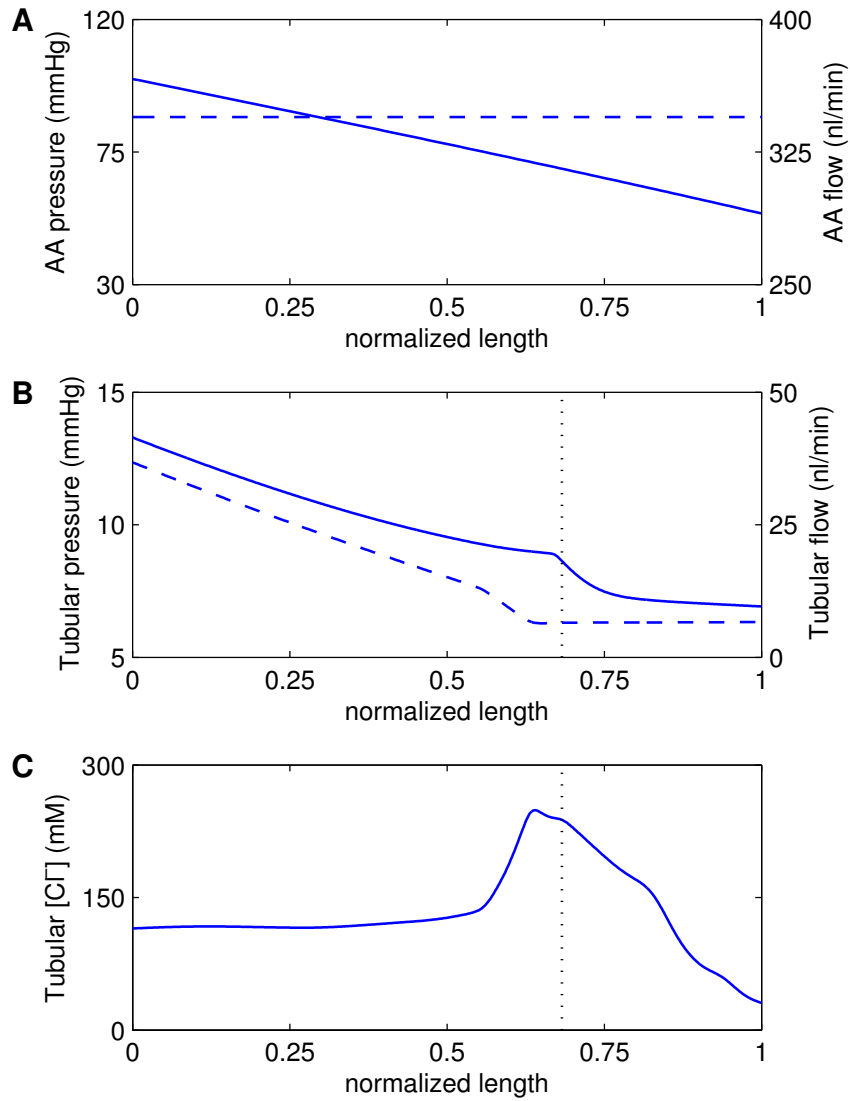


FIGURE 3.3: Spatial profiles of fluid pressure (solid lines) and flow rate (dashed lines) along the afferent arteriole (A) and along the proximal tubule and loop of Henle (B). C: tubular fluid Cl^- concentration profile. Afferent arteriole and tubular lengths are normalized by L_{AA} and L_T , respectively. Dotted line indicate the position of the loop bend. Profiles change dynamically due to spontaneous vasomotion. Profiles shown are snapshots at time $t = 25$ s (see Fig. 3.2).

3.3.2 Autoregulatory response to steady pressure perturbations

We studied the model’s response to sustained $P_0(t)$ perturbations. Figure 3.4 displays the normalized deviations of time-averaged pressure and flow at various locations within the model nephron, and Cl^- concentration at the macula densa, as functions of a range of time-independent P_0 values. These deviations were normalized by the corresponding base-case values of Table 3.3. Two sets of simulations were carried out: one with the full model (solid lines), and one with the myogenic response disabled (dashed lines). The latter case was implemented by setting the myogenic current $I_{myo}^i(t)$ to zero.

At low inflow pressure ($P_0 < 100$ mmHg), the full model predicts vasodilation, which reduces vascular resistance and raises downstream pressure; at high pressure ($P_0 > 100$ mmHg), the afferent arteriole smooth muscle cells constrict, with opposite effects. With these myogenic responses, the model attains a hemodynamic “plateau” for P_0 that falls within the range 90–190 mmHg, where time-averaged downstream fluid pressure and flow values remain close to base-case values.

The sigmoidal dependence of \bar{I}_{myo}^i on pressure deviations (see Table 3.1) implies lower and upper limits beyond which the induced I_{myo}^i fails to provide further alteration in smooth muscle membrane potential. Due to this restriction, vascular diameter at low ($P_0 < 80$ mmHg) or high ($P_0 > 200$ mmHg) pressures does not adjust sufficiently. As a result, some of the pressure perturbation is transmitted downstream. Because the model afferent arteriole fails to adequately compensate, outflow delivery deviates noticeably from base case.

When the myogenic response was disabled, the model predicted a steady increase in vascular and tubular fluid pressure and flow, as P_0 was increased. It is noteworthy that macula densa Cl^- concentration is highly sensitive to increases in tubular inflow conditions (Fig. 3.4E). However, at low inflow pressure and tubular flow, Cl^- con-

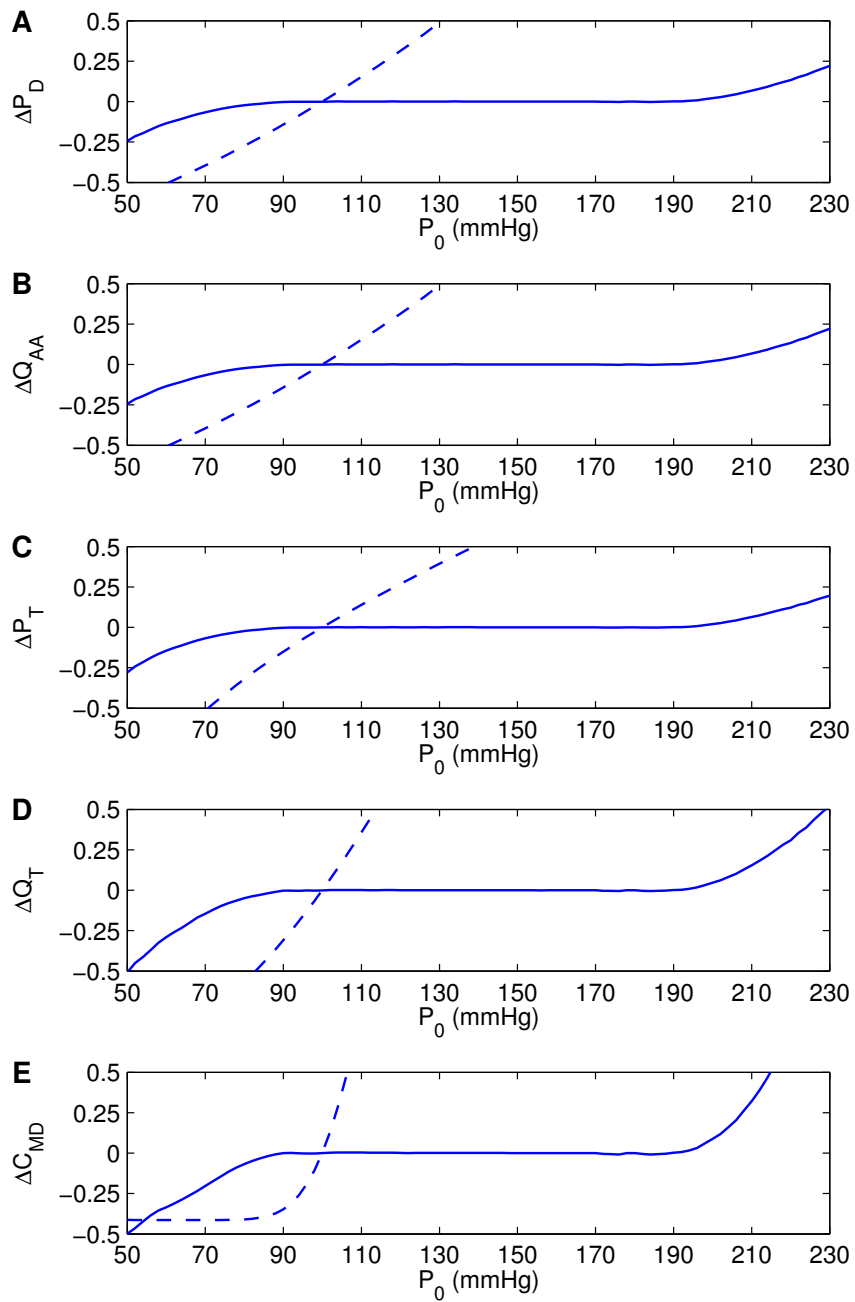


FIGURE 3.4: Autoregulatory responses to sustained steady P_0 perturbations, obtained with (solid lines) and without (dashed lines) the myogenic response. Results are shown as deviations from base-case values, normalized by respective reference values (listed in Table 3.3). A, B: afferent arteriole outflow pressure and flow rate, respectively; C, D: proximal tubule inflow pressure and flow rate, respectively; E: tubular fluid Cl^- concentration at macula densa.

centration at thick ascending limb becomes low enough that the active reabsorption of Cl^- is sufficiently slow to be balanced by the passive diffusion into the lumen. At this point, a “static head” is reached, in which the axial gradient of the luminal Cl^- concentration profile near the macula densa approaches zero, and Cl^- concentration at macula densa no longer decreases as inflow pressure is further lowered.

3.3.3 Response to step-pressure changes

We simulated the responses of flow and Cl^- transport to a rapid step-like increase and decrease in $P_0(t)$. Specifically, the afferent arteriole inflow pressure had the form

$$P_0(t) = \bar{P}_0 \pm P_p \frac{1 + \tanh(t/s_p)}{2}, \quad (3.33)$$

where $\bar{P}_0 = 100$ mmHg, $P_p = 15$ mmHg, and $s_p = 0.10$ s. With these parameters, the pressure step approximately completes within ~ 0.5 s. Results are shown in Fig. 3.5.

With both pressure up- and down-steps, the responses of pressure and flow rate at the afferent arteriole and the proximal tubule were almost instant. In contrast, the response of the macula densa Cl^- concentration had a delay of ~ 5 s. Following the step perturbations, all variables underwent a transient overshoot that lasted considerably longer for the pressure down-step than the pressure up-step. Characteristically, the Cl^- concentration response induced by the pressure down-step was fully developed within ~ 40 s, while for the pressure up-step the response was fully developed within ~ 25 s. It is also noteworthy that the deviation in macula densa Cl^- concentration, relative to its base-case value, is much larger than the corresponding relative change in pressures and flow rates.

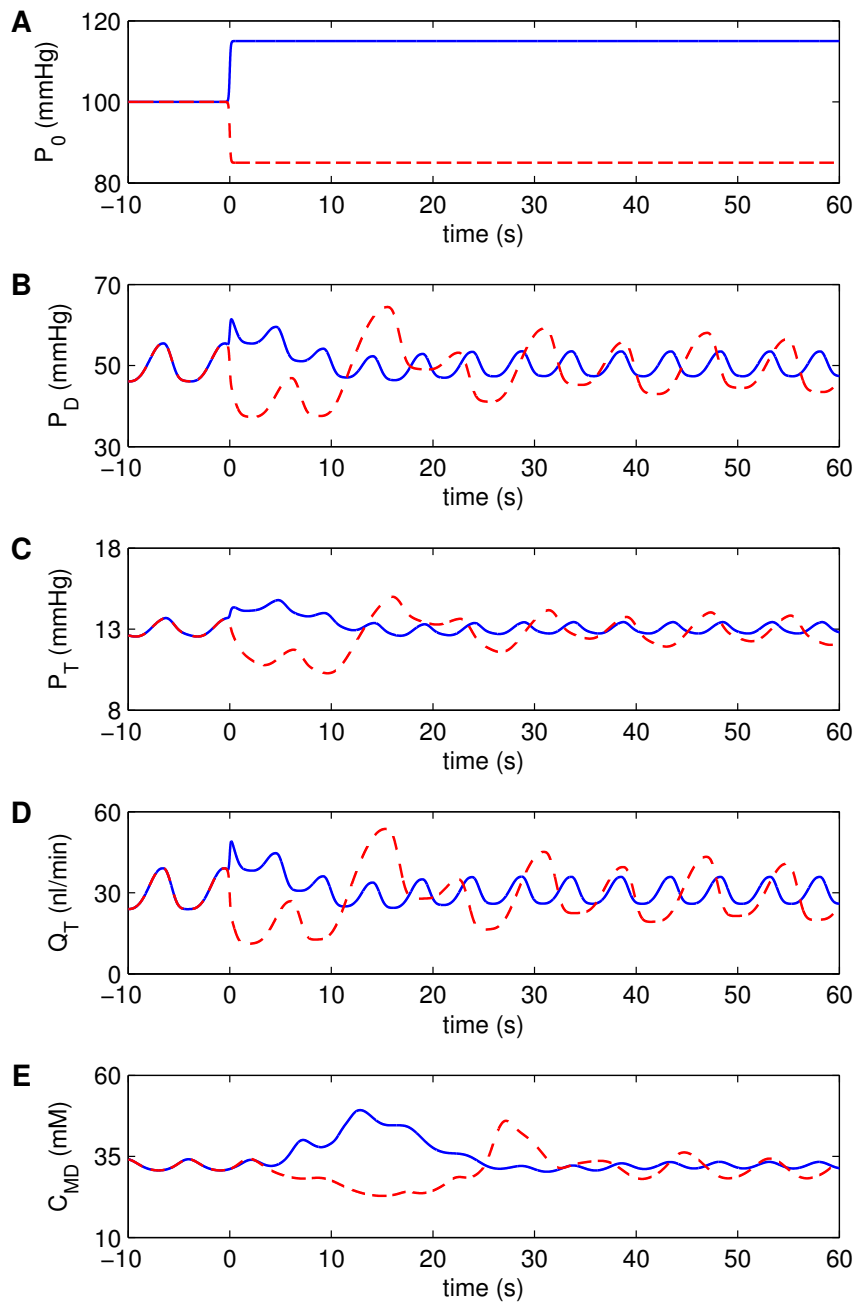


FIGURE 3.5: Model responses to step-pressure changes in afferent arteriole inflow pressure. Solid lines: step-increase; dashed lines: step-decrease. A, B: afferent arteriole inflow and outflow pressures, respectively; C, D: proximal tubule inflow pressure and flow rate, respectively; E: tubular fluid Cl^- concentration at macula densa.

3.3.4 Spectral response to sinusoidal pressure perturbations

To study the characteristics of the transduction of oscillations in $P_0(t)$ into oscillations in fluid flow and tubular Cl^- transport, we superimposed a sinusoidal perturbation onto $P_0(t)$, i.e., for $t \geq 0$ we applied an inflow pressure of

$$P_0(t) = \bar{P}_0 + P_p \sin(2\pi f_{ext}t), \quad (3.34)$$

where $\bar{P}_0 = 100$ mmHg and $P_p = 2.5$ mmHg. The frequency f_{ext} was varied between 0 and 250 mHz.

Figure 3.6 shows the power spectral density of proximal tubule inflow pressure for three f_{ext} values: 0, 30, 60 mHz. To compute power spectra, we sampled the proximal tubule inflow pressure at 80 Hz, over the time window $100 \leq t \leq 1738$ s. At $t = 100$ s, practically all transient responses had dissipated. The sampled pressure values were normalized by 13 mmHg and the resulting time series was used to compute power spectra. For the numerical evaluation of all power spectra presented here no windowing is used, which results in spectral leakage and consequently widening of the associated spectral peaks.

The case with $f_{ext} = 0$ corresponds to the base case where no external forcing was applied; thus, Fig. 3.6C1 is the same as the top time course in Fig. 3.2B1. In this case, model variables oscillated with frequency $f_{myo} = 165$ mHz, driven by the spontaneous vasomotion exhibited by the afferent arteriole. The spectrum shown in Fig. 3.6C2 contains a single peak at f_{myo} . The harmonics $2f_{myo}$, $3f_{myo}$, etc. are also present (harmonics not shown).

Sinusoidal forcing introduces complexities into the power spectra of the system. When an external forcing of 30 mHz was applied, the resulting power spectrum (Fig. 3.6B2) shows not only the frequencies of the forcing and vasomotion (at 30 and 165 mHz, respectively), harmonics of the forcing (60, 90, 120, 150 mHz), but also linear combinations of these frequencies (105, 135, 195 mHz), which arise from a phe-

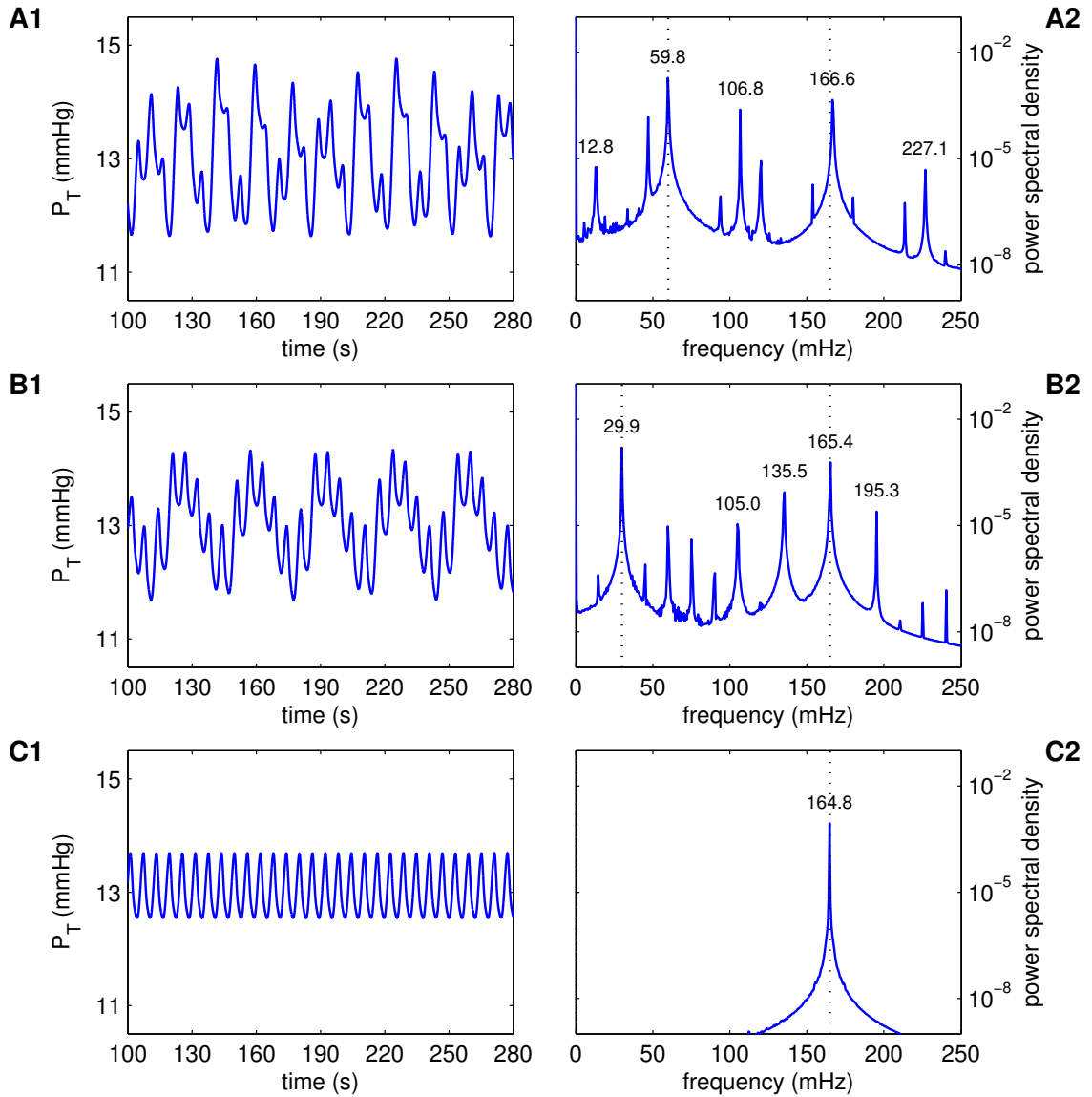


FIGURE 3.6: Proximal tubule inflow pressure responses to pressure perturbations at $f_{ext} = 60$ mHz (A1), 30 mHz (B1), and 0 mHz (C1, unperturbed pressure, i.e., Fig. 3.2B1). Corresponding power spectra are shown in A2, B2, C2, respectively. Dotted lines denote f_{ext} and vasomotion frequency f_{my0} .

nomenon known as heterodyning (see Discussion). A similar analysis can be applied to the power spectrum obtained when a 60 mHz forcing was imposed (Fig. 3.6A2).

The model's response to P_0 oscillations at frequencies 0–250 mHz is summarized in Fig. 3.7, which shows the power spectral density (color coded) of the frequency components (horizontal axis) corresponding to the forcing frequencies. The magenta lines identify spectral peaks, which arise from vasomotion, external forcing, heterodyning, and harmonics. The line labelled f_{myo} , which corresponds to vasomotion, runs parallel to the f_{ext} -axis, which suggests that the vasomotion frequency is insensitive to the forcing frequency of the applied perturbations. The line labelled f_{ext} , which corresponds to the frequency of the external forcing, extends from the origin and runs diagonally across the f - f_{ext} plane. One can also discern additional lines that extend from the origin. These lines, which can be approximated by $f = kf_{ext}$, where $k = 2, 3, \dots$, correspond to the harmonics of the forcing frequency. Heterodyning, which generates frequencies from mixing the forcing and myogenic frequencies, gives rise to lines $\alpha f_{myo} \pm \beta f_{ext} = 0$, where α and β are integers.

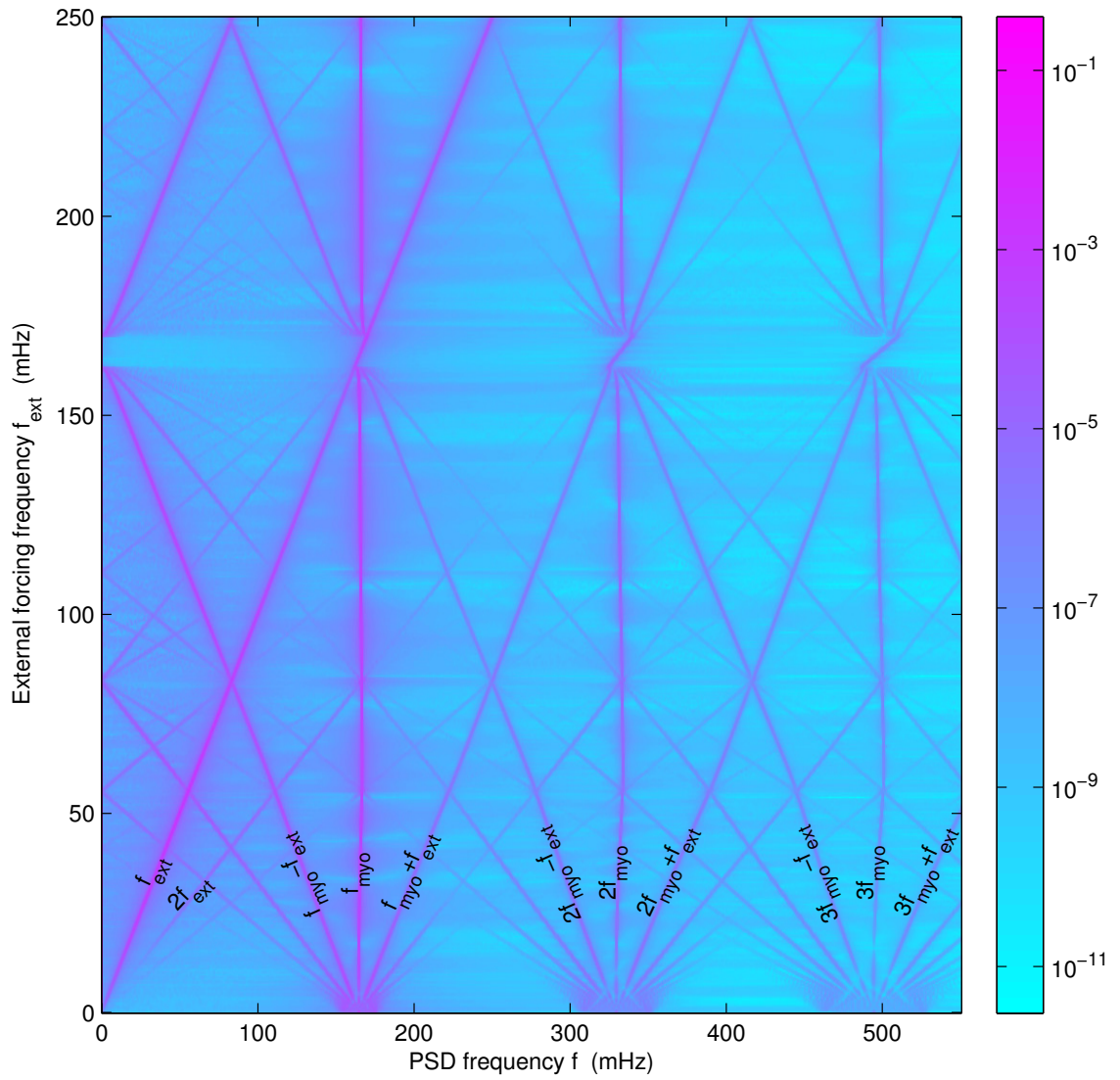


FIGURE 3.7: Contour of power spectral density of proximal tubule inflow pressure obtained for forcing frequencies f_{ext} 0–250 mHz. Peaks arising from forcing (f_{ext}) and vasomotion (f_{myo}) are identified, as well as harmonics and major heterodynes.

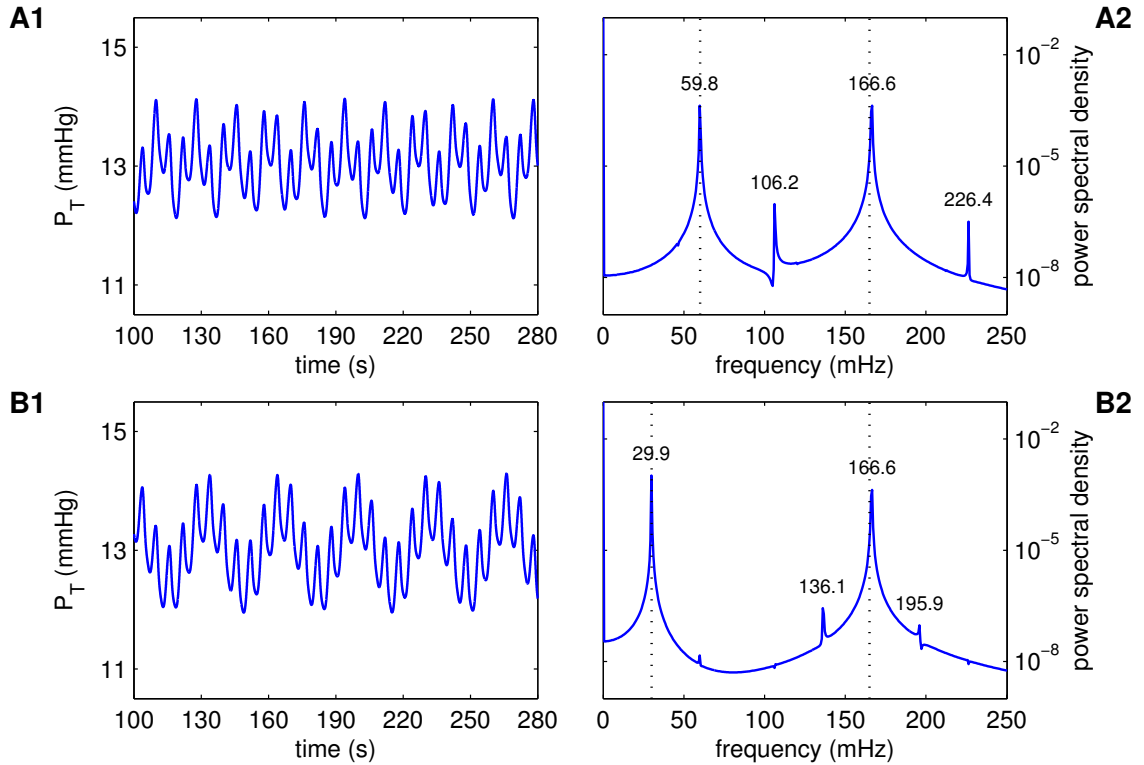


FIGURE 3.8: Proximal tubule inflow pressure responses to pressure perturbations at $f_{ext} = 60$ mHz (A1) and 30 mHz (B1), obtained with the myogenic response disabled. Corresponding power spectra are shown in A2, B2, respectively. Dotted lines denote f_{ext} and vasomotion frequency f_{myo} .

Interestingly, the model also revealed a small range of f_{ext} for which only one dominant frequency can be identified. That region corresponds to the narrow sparse band of $160 \leq f_{ext} \leq 170$ mHz in Fig. 3.4. In this region, f_{ext} is sufficiently close to f_{myo} that the two oscillations synchronize, resulting in the disappearance of all frequencies that would otherwise be generated from heterodyning.

Next we considered the signal transduction properties of different segments of the nephron. To that end, we applied sinusoidal inflow pressure perturbations at 30 mHz, and computed oscillations in tubular fluid pressure, fluid flow, and chloride concentration at the proximal tubule entrance, loop bend, and macula densa. Those time courses, normalized by the respective reference values (listed in Table 3.3), are

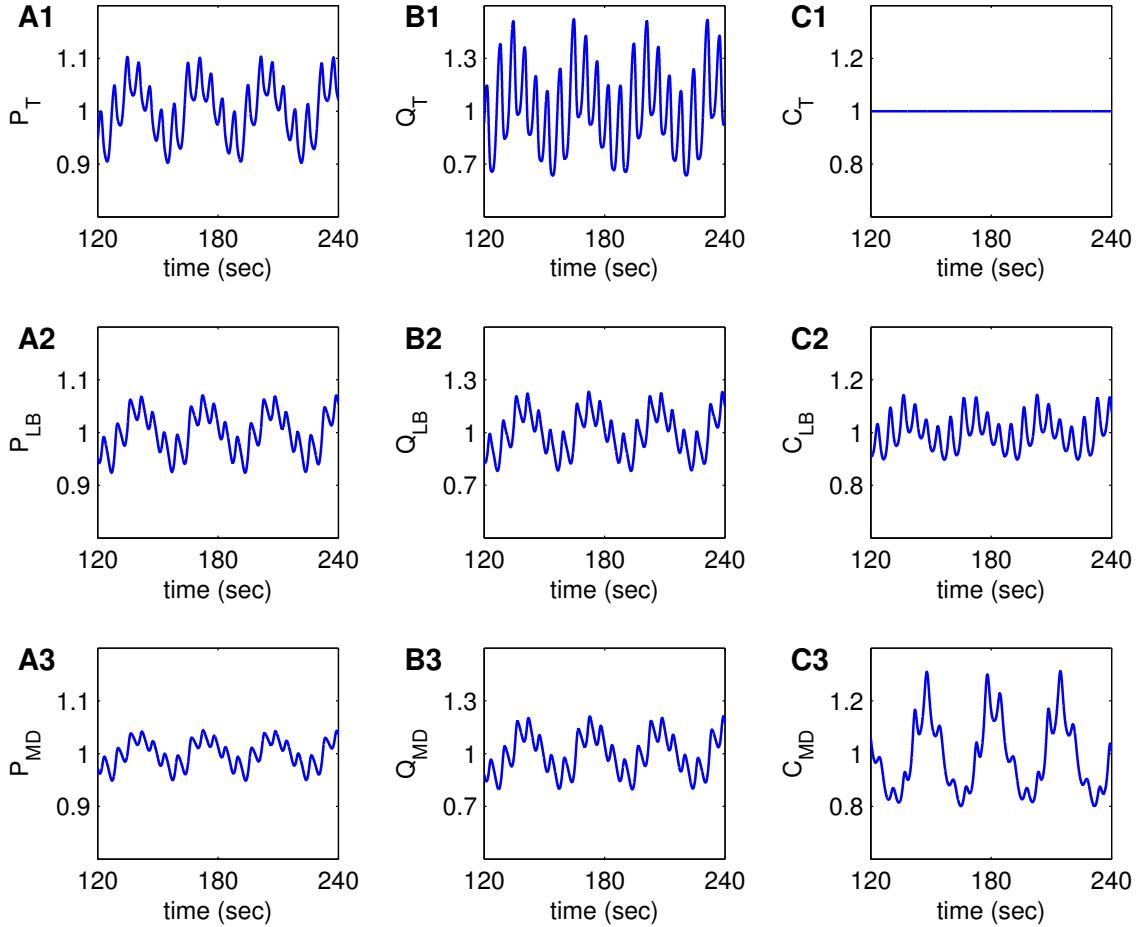


FIGURE 3.9: Pressure, flow, and $[Cl^-]$ oscillations, driven by sinusoidal pressure forcing at 30 mHz, obtained at proximal tubule entrance (top row), loop bend (middle row), and macula densa (bottom row). Time courses have been normalized by respective reference values (listed in Table 3.3).

shown in Fig. 3.9. Due to the tortuosity of the proximal tubule which results in a model tubule of considerable length, and to the nonlinear dependence of Ω_T on distal tubular pressure, significant damping is observed in the pressure oscillations. A comparison of proximal tubule inflow and thick ascending limb outflow pressure time courses reveals an amplitude reduction of $\sim 75\%$ in agreement with measurements [72]. If Ω_T were fixed, the amplitude damping is lowered to $\sim 50\%$ (results not shown).

The more significant damping on flow oscillations along the proximal tubule and

descending limb is attributable to the assumption of fractional reabsorption, such that water reabsorption is proportional to glomerular filtration rate (Eq. (3.29)). Recall that boundary chloride concentration at the proximal tubule was assumed constant. Thus, the oscillations in $[\text{Cl}^-]$ at the loop bend arose from oscillations in fluid flow rate and the resulting oscillations in Cl^- transport along the proximal tubule and descending limb. It is noteworthy that Cl^- oscillations of significant amplitude were generated both at low and high frequencies. A comparison between the $[\text{Cl}^-]$ profiles at loop bend and macula densa suggests that the thick ascending limb imposes significant damping on $[\text{Cl}^-]$ oscillations, especially at high frequencies. In other words, the thick ascending limb serves as a low-pass filter for the $[\text{Cl}^-]$ signal.

Besides mediating spontaneous vasomotion, the myogenic response determines arteriolar flow and pressure, and thus also tubular transport. To study the impacts of the myogenic response on the spectral complexity of the tubular fluid oscillations, we repeated the above simulations for $f_{ext} = 30$ and 60 mHz, with the myogenic response disabled. That is, we set $I_{myo}^i(t) = 0$ for all smooth muscles. The resulting proximal tubule inflow pressure time courses and the corresponding power spectral densities are shown in Fig. 3.8. A comparison of Fig. 3.8, panels A2 and B2, with Fig. 3.6, panels A2 and B2, suggests that the absence of the myogenic response significantly reduces the spectral complexity of the tubular flow oscillations. In Figs. 3.8A2 and 3.8B2, the only clearly identifiable peaks are found at $f_{myo} = 165$ mHz, and $f_{ext} = 30$ or 60 mHz, and at the major heterodynes at $f_{myo} \pm f_{ext}$. Unlike in Fig. 3.6, harmonics and other heterodynes are substantially weaker.

3.3.5 Spectral response to sinusoidal electrical perturbations

Besides the myogenic response considered thus far, the afferent arteriole is the effector also of a number of other regulatory mechanisms. One such mechanism is the TGF mechanism, by which an electrical signal is sent to distal afferent arteriole cells to

induce vasoconstriction or vasodilation in response to variations in luminal fluid Cl^- concentration near the macula densa. It is known that TGF can lead to oscillations in tubular fluid flow and Cl^- transport. To simulate that oscillatory signal, and to study the spectral complexity of the tubular flow oscillations that the signal generates, we kept P_0 constant at 100 mmHg and applied a sinusoidal current

$$I_{ext}(t) = C_m I_p \sin(2\pi f_{ext} t), \quad (3.35)$$

to the membrane potential dynamics, Eq. (3.1), of the 20 smooth muscles proximal to the glomerulus. To facilitate a comparison between these simulations with the ones carried with sinusoidal pressure perturbations, the amplitude I_p was set to $4 \text{ mV}\cdot\text{s}^{-1}$, so that at $f_{ext} = 30 \text{ mHz}$ the amplitudes of the induced proximal tubule pressure oscillations were similar in the two sets of simulations.

The electrical perturbation induced periodic polarization and depolarization in the 20 afferent arteriole cells to which the current was applied, as well as in all upstream arteriole cells, albeit to a lesser extent, owing to the intercellular coupling via gap junctions and via the endothelium.

The interactions among spontaneous vasomotion (at f_{myo}) and electrically-induced vasomotion (at f_{ext}) resulted in composite periodic oscillations in vascular resistance, afferent arteriole flow, glomerular filtration rate, tubular flow, and Cl^- transport. Proximal tubule inflow pressure oscillations are shown in Fig. 3.10 (A1 and B1), for $f_{ext} = 60$ and 30 mHz . The power spectra, obtained as described above, exhibit complexity similar to those obtained for sinusoidal pressure perturbations (compare with Fig. 3.6). Harmonics and heterodynes can be identified in the power spectra (Fig. 3.10, A2 and B2). Further, a contour plot of power spectral density as a function of f and f_{ext} is qualitatively similar to Fig. 3.7 (not shown).

3.4 Discussion

We have developed a mathematical model that simulates fluid flow along the afferent arteriole, glomerulus, and short-loop nephron in a rat kidney. The model predicts dynamical fluid pressure, flow rate, and Cl^- concentration profiles (Fig. 3.3). Also, within the afferent arteriole smooth muscles, the model predicts that interactions among Ca^{2+} and K^+ membrane transports spontaneously generate cytosolic Ca^{2+} oscillations resulting in vasomotion with frequency ~ 165 mHz [27, 145].

The model afferent arteriole's myogenic response is based on the assumption that changes in luminal pressure induce changes in the activity of nonselective cation channels, which in turn changes the smooth muscle cell membrane potential that sets the vascular tone and thus resistance to blood flow. Through its myogenic response, the model afferent arteriole is effective in maintaining almost stable afferent arteriole's outflow for steady inflow pressure in the range 90–190 mmHg. As a result, flow and Cl^- transport in the renal tubule are also stabilized in that range of inflow pressures (Fig. 3.4). A stable glomerular filtration rate is essential for maintaining normal kidney functions. Abnormally high arteriolar pressure that is not effectively regulated by the afferent arteriole may lead to damages in the glomerulus, whereas exceedingly low glomerular filtration may impair the elimination of waste products such as urea and creatinine. Indeed, failure to adjust doses of drugs that are normally excreted by the kidneys, e.g., aminoglycoside antibiotics and heparin, may lead to accumulation of those drugs at toxic levels.

In addition to studying the model's response to steady pressure perturbations, we obtained model results for periodic pressure or electrical forcing. A prediction of the model nephron is that heterodyning increases the complexity of the power spectra associated with the oscillations of fluid flow and Cl^- transport variables. Heterodyning is the phenomenon in which when two input frequencies (which, in

our case, correspond to spontaneous vasomotion and the pressure or electrical forcing) are combined in a nonlinear signal processor, new frequencies are generated that are linear combinations of the original frequencies. As can be observed in Figs. 3.6, 3.7, 3.8, and 3.10, the heterodynes are associated with frequencies at approximately $\alpha f_{myo} + \beta f_{ext}$, where α and β are integers. The strongest of such peaks are predicted at the frequencies $f_{myo} \pm f_{ext}$. These peaks have been previously identified experimentally using spectral analysis in Sprague-Dawley and spontaneously hypertensive rats [135, 29].

With appropriate forcing frequencies, the model predicts spectral peaks in the low frequency band around or below 10–20 mHz (see Figs. 3.6, 3.7, and 3.10). These peaks are heterodynes that arise from the interaction between the external forcing and the spontaneous vasomotion, or between their harmonics. (Note that TGF may be seen as an instance of (almost) periodic external electrical forcing.) It has been previously proposed that spectral peaks in this frequency range, which have been identified *in vivo* and *in vitro* using spectral analysis [80, 81, 151], indicate the existence of a third autoregulatory mechanism. Our model results suggest that heterodyning may explain, or at least contribute to, the generation of these slow oscillations.

Previous efforts in modeling renal autoregulation include a model of the myogenic control of the afferent arteriole by Lush and Fray [109], who used that model to study the steady-state autoregulation of renal blood flow in the dog kidney. Further, Moore et al. [121] presented a steady-state model of the renal vascular and tubular systems to simulate TGF and myogenic mechanisms. Because these models focused on steady-state autoregulation, details of the kinetics of the ionic transport and arteriolar muscle mechanisms were not represented.

In this study, the representation of the smooth muscle cells in the afferent arteriole submodel is based on our previous work [27, 145], which was in turn based

on a model for the cat cerebral arterioles developed by Gonzalez-Fernandez and Erementrout [61], with appropriate adjustments in parameters and the addition of the myogenic response. The model in Ref. [61] was also adopted by Marsh et al. [112] to study the interactions between myogenic response and TGF. In that model, myogenic responses were generated only by oscillatory transmural pressure, although experimental observations have indicated that changes in mean pressure also induce myogenic responses [106]. In contrast, our model exhibits myogenic responses as a function of both pressure and its rate of change, with the current associated with the myogenic response chosen such that the autoregulatory plateau agrees with experimental findings (Fig. 3.4). Another difference is that the myogenic model in Ref. [112] represents only two myogenically active afferent arteriolar segments. Thus, each submodel represents a rather long segment along the afferent arteriole, whereas in the present study, each afferent arteriolar cell submodel roughly corresponds to an afferent arteriole cell [102], with parameters adjusted for each cell based on the observation that the arteriolar cells are exposed to different external environments (e.g., intravascular fluid pressure).

The present model can be used as an essential component in models of integrated renal hemodynamic regulation. An important renal autoregulatory mechanism that is not represented in the current model is the tubuloglomerular feedback (TGF) system, which is a negative feedback loop in which glomerular filtration rate is adjusted according to Cl^- concentration that is sensed downstream in the nephron tubule by the macula densa cells. Our decision not to include TGF in this study was driven by the goal to paint a clear picture of the roles of myogenic response and vasomotion, and their interactions, in renal blood flow, and our belief that the inclusion of a feedback mechanism should be done only after a thorough understanding of the individual components.

By incorporating the TGF response in future studies, one may study the interac-

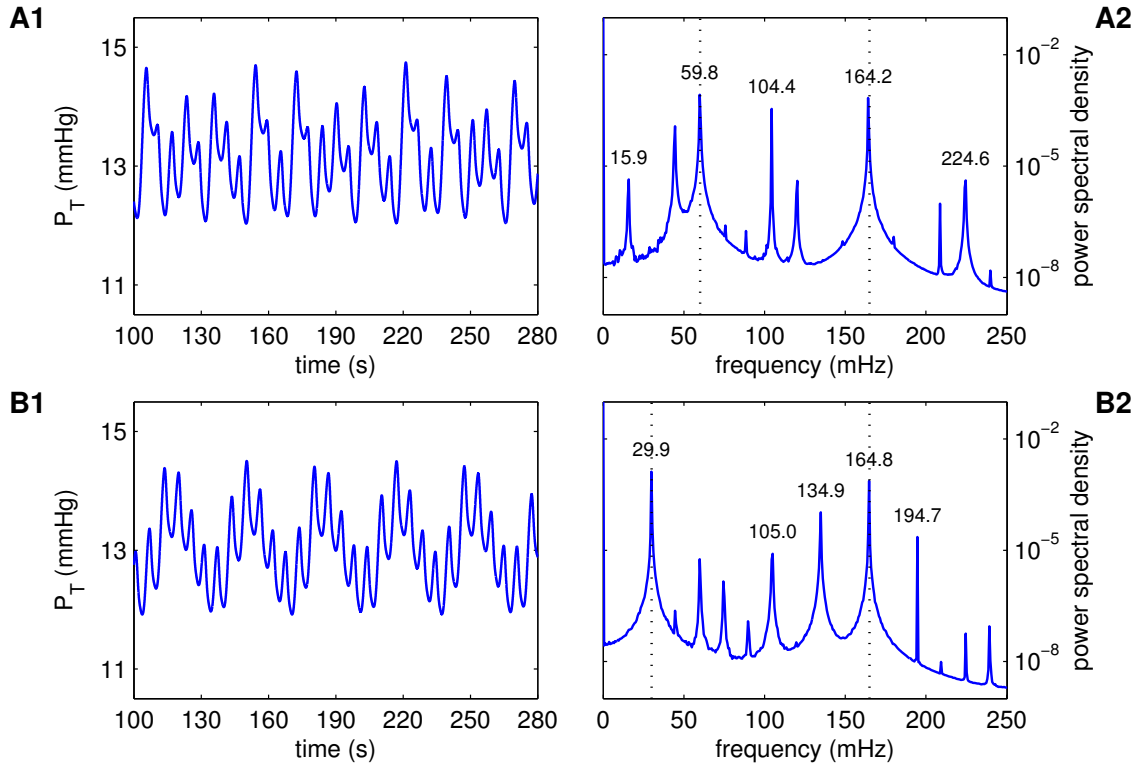


FIGURE 3.10: Proximal tubule inflow pressure responses to electrical perturbations at $f_{ext} = 60$ mHz (row A) and 30 mHz (row B), and corresponding power spectra. Dotted lines denote f_{ext} and vasomotion frequency f_{myo} .

tions between the myogenic and TGF responses, which share the afferent arteriole as a common effector. Further down the road, by coupling a number of these nephrovascular hemodynamics models, one can investigate the propagation of vasomotor and TGF response along the renal vasculature.

Assessment of Renal Autoregulation

4.1 Introduction

The generally stable glomerular filtration rate (GFR) is a result of renal autoregulation, as is the protection of glomerular capillaries from excessive intravascular pressure and shear stress. Renal autoregulation is mediated by several mechanisms: the myogenic response, which is a property of the preglomerular vasculature wherein a rise in intravascular pressure elicits a reflex constriction that generates a compensatory increase in vascular resistance; and the tubuloglomerular feedback (TGF), a negative feedback response that balances glomerular filtration with tubular reabsorptive capacity [37, 73, 82]. A third mechanism has been speculated to make a minor contribution; this mechanism appears to be much slower and remains poorly understood [82, 150]. A fourth mechanism, which has been termed connecting-tubule TGF, appears to induce dilation in the afferent arteriole when sodium concentration rises in the connecting tubule [137].

The major autoregulatory mechanisms, myogenic response and TGF, operate via depolarization of the afferent arteriole smooth muscle cells. By sharing a common

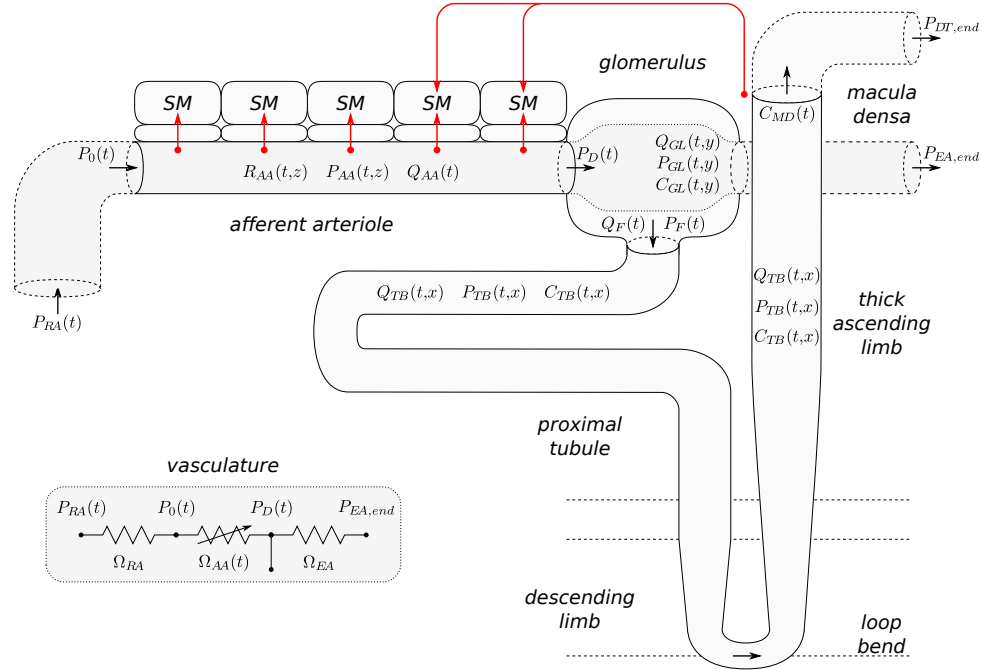


FIGURE 4.1: Schematic diagram of model configuration. Red arrows represent myogenic and TGF currents. R , P , Q , C , and Ω denote radius, fluid pressure, fluid flow, concentration, and resistance. Afferent arteriole segment is shown with a reduced number of smooth muscles (SM). *Inset:* Equivalent circuit of the model vasculature.

effector, the two mechanisms are expected to interact. To study the two mechanisms and their interactions, we have developed a mathematical model that combines the myogenic response and TGF at the nephrovascular level in the rat kidney. The other two mechanisms, which are less well characterized, are not considered. We use the model to assess the relative contributions of myogenic response and TGF to overall autoregulation, under physiological and pathophysiological conditions.

4.2 Mathematical model

A schematic diagram of the renal autoregulation model is given in Fig. 4.1. The model consists of three major components: (i) an afferent arteriole segment [145], (ii) glomerular filtration [41], and (iii) a short loop nephron segment [90]. These components are described below.

4.2.1 Afferent arteriole submodel

The representation of the afferent arteriole segment is based on a model previously developed by us [145]. It represents an afferent arteriole segment consisting of a series of $N_{AA} = 101$ smooth muscle cell models [27], electrically coupled via gap junctions and via an endothelial cell layer. The cellular dynamics of each smooth muscle cell, influenced by the autoregulatory mechanisms, determine the vascular tone. The resulting vascular resistance is the main determinant of blood flow and single-nephron GFR (SNGFR) (see below).

Each smooth muscle cell model incorporates cell membrane potential, transmembrane ionic transports, cytosolic Ca^{2+} regulation, and muscle contraction. The interactions between Ca^{2+} and K^+ fluxes, which are mediated by voltage-gated and voltage-calcium-gated channels, respectively, give rise to the development of spontaneous oscillations in membrane potential. This in turn results in oscillations in cytoplasmic Ca^{2+} concentration and muscle tone.

Detailed descriptions of the afferent arteriole smooth muscle cell and vessel models can be found in Refs. [27, 145]. Here we summarize key components of the model and highlight modifications from previous models.

Smooth muscle cell membrane potential

The smooth muscle cells that form the afferent arteriole are indexed by i , where $i = 1$ and $i = N_{AA}$ denote the cells proximate to the renal artery ($z = 0$) and glomerulus ($z = L_{AA}$), respectively. The rate of change of the membrane potential v_m^i of the i -th smooth muscle is a function of the sum of transmembrane currents

$$C_m \frac{dv_m^i}{dt} = -I_L^i - I_K^i - I_{\text{Ca}}^i + I_{m-m}^i + I_{m-e}^i + I_{\text{MR}}^i + I_{\text{TGF}}^i, \quad (4.1)$$

where C_m denotes the cell capacitance, and I_L^i , I_K^i , I_{Ca}^i , I_{m-m}^i , I_{m-e}^i denote transmembrane leak current, potassium current, calcium current, gap junctional current

between smooth muscle cells, and gap junctional current between smooth muscle cell and the endothelium, respectively. The remaining currents, I_{MR}^i and I_{TGF}^i , arise from the operation of the myogenic response and TGF (see below).

Myogenic response The model assumes that the activity of non-selective cation channels is shifted by changes in intravascular pressure, such that the smooth muscle membrane depolarizes with increasing intravascular pressure and *vice versa*. This process is represented by a pressure-dependent current I_{MR}^i in Eq. (4.1) given by

$$\frac{d}{dt}I_{\text{MR}}^i(t) = \begin{cases} -k_{\text{inc}}(I_{\text{MR}}^i(t) - \bar{I}_{\text{MR}}^i(P_{\text{AA}}^i(t))), & \text{if } \frac{d}{dt}P_{\text{AA}}^i(t - \tau_m) \geq 0, \\ -k_{\text{dec}}(I_{\text{MR}}^i(t) - \bar{I}_{\text{MR}}^i(P_{\text{AA}}^i(t))), & \text{if } \frac{d}{dt}P_{\text{AA}}^i(t - \tau_m) < 0, \end{cases} \quad (4.2)$$

where P_{AA}^i denotes the intravascular pressure. The rate of change of I_{MR}^i at time t depends on the direction in which P_{AA}^i is changing at an earlier time $t - \tau_m$. If $\frac{d}{dt}P_{\text{AA}}^i(t - \tau_m) \geq 0$, then the afferent arteriole responds to a pressure increase; conversely, if $\frac{d}{dt}P_{\text{AA}}^i(t - \tau_m) < 0$, the afferent arteriole responds to a pressure decrease. The target current \bar{I}_{MR}^i increases with pressure and saturates at sufficiently large perturbations; see Fig. 4.2A. Specifically, \bar{I}_{MR}^i is given by the following sigmoidal function:

$$\bar{I}_{\text{MR}}^i(P_{\text{AA}}^i) = C_m \left(I_{\text{MR},\text{min}} + \frac{I_{\text{MR},\text{max}} - I_{\text{MR},\text{min}}}{1 - \left(\frac{I_{\text{MR},\text{max}}}{I_{\text{MR},\text{min}}} \right) \exp(-s_{\text{MR}}(P_{\text{AA}}^i(t - \tau_m) - \bar{P}_{\text{AA}}^i))} \right) \quad (4.3)$$

The reference pressure \bar{P}_{AA}^i varies among the cells inasmuch as the baseline luminal pressure profiles, which reduces linearly along the vessel from 95 mmHg to 50 mmHg. The model assumes that the myogenic current is a function of local pressure only, whereas channel-mediated currents typically depend on membrane potential and resting potential. Because the cation channels that might be involved in the myogenic response have yet to be identified, the related resting potential too is unknown.

Owing to these uncertainties, the simplifying assumption of a pressure-dependent myogenic current is made.

To model the asymmetry in the vasoresponse time courses reported in [106, 105], the rate constants k_{inc} and k_{dec} in Eq. (4.2), which correspond to pressure increase and decrease, are set to 0.55 s^{-1} and 0.13 s^{-1} , respectively. Similarly, the response delay τ_m is set to 0.3 s for pressure increase and to 1 s for pressure decrease.

Tubuloglomerular feedback The TGF signal is represented by the current I_{TGF}^i , which is applied to the smooth muscles spanning the distal $60 \mu\text{m}$ of the afferent arteriole. The current I_{TGF}^i is assumed to exhibit a sigmoidal dependence on intratubular macula densa $[\text{Cl}^-]$ (denoted C_{MD}),

$$I_{\text{TGF}}^i(C_{\text{MD}}) = C_m \left(I_{\text{TGF},\text{min}} + \frac{I_{\text{TGF},\text{max}} - I_{\text{TGF},\text{min}}}{1 - \left(\frac{I_{\text{TGF},\text{max}}}{I_{\text{TGF},\text{min}}} \right) \exp(-s_{\text{TGF}}(C_{\text{MD}} - \bar{C}_{\text{MD}}))} \right), \quad (4.4)$$

where $\bar{C}_{\text{MD}} = 32 \text{ mM}$ is the operating macula densa $[\text{Cl}^-]$. The parameters $I_{\text{TGF},\text{max}}$, $I_{\text{TGF},\text{min}}$, and s_{TGF} determine the dynamic range and open-loop gain of TGF.

Calcium dynamics and crossbridge phosphorylation Free cytosolic Ca^{2+} concentration, denoted c^i , is assumed in equilibrium with the buffer B_{T} and is related to influx through the membrane channels I_{Ca}^i by

$$\frac{dc^i}{dt} = \frac{(K_d + c^i)^2}{(K_d + c^i)^2 + K_d B_{\text{T}}} \left(-\alpha_{\text{Ca}} I_{\text{Ca}}^i - k_{\text{Ca}} c^i \right), \quad (4.5)$$

where α_{Ca} , which depends on the cytosolic volume and valence of the calcium ion, relates the calcium current to changes in cytosolic $[\text{Ca}^{2+}]$, and k_{Ca} is the first-order rate constant for cytosolic calcium extrusion [26]. Cytosolic $[\text{Ca}^{2+}]$ determines the phosphorylation level ψ^i

$$\psi^i = \frac{(c^i)^3}{c_{\text{M}}^3 + (c^i)^3}, \quad (4.6)$$

which in turn determines the fraction of formed crossbridges, denoted ω^i , according to

$$\frac{d\omega^i}{dt} = k_{\psi} \left(\frac{\psi^i}{\psi^i + \psi_M} - \omega^i \right). \quad (4.7)$$

Parameters value can be found in Table 4.2.

Muscle mechanics To represent muscle mechanics, we have adopted the model formulated by Secomb and co-workers [21, 3, 20]. In this model, vasomotion is driven by the balance between pressure-induced tension, T_P^i , and wall tension, T_{wall}^i . Wall tension consists of a passive and an active components, $T_{\text{wall}}^i = T_{\text{pass}}^i + T_{\text{act}}^i$. The active wall tension component is given by

$$T_{\text{act}}^i = \omega^i T_{\text{act,max}}^i, \quad (4.8)$$

where $T_{\text{act,max}}^i$ is the maximum active tension that can be generated at a given vessel circumference (see below). The muscle activation level is taken equal to the fraction of formed crossbridges ω^i .

For a given smooth muscle luminal radius R_{AA}^i , the following wall tensions are developed

$$T_{\text{pass}}^i = C_{\text{pass},0} \exp \left(C_{\text{pass},1} \left(\frac{R_{AA}^i}{R_{AA,c}} - 1 \right) \right), \quad (4.9)$$

$$T_{\text{act,max}}^i = C_{\text{act},0} \exp \left(\left(\frac{R_{AA}^i/R_{AA,c} - C_{\text{act},1}}{C_{\text{act},2}} \right)^2 \right). \quad (4.10)$$

Parameter values are listed in Table 4.3. Tension arising from transmural pressure is given by the Laplace law:

$$T_P^i = (P_{AA}^i - P_{\text{ext}}) R_{AA}^i. \quad (4.11)$$

The extravascular pressure P_{ext} is assumed constant at 5 mmHg.

The difference between pressure-induced tension and the wall tension gives rise to changes in vascular radius

$$\frac{dR_{AA}^i}{dt} = \frac{1}{\tau_c} \left(T_P^i - \xi^i T_{\text{wall}}^i \right). \quad (4.12)$$

Because the hydrostatic pressure P_{AA}^i decreases along the vessel, baseline T_P^i also decreases axially. Thus, a scaling factor ξ^i , which decreases linearly from 4/3 to 2/3 along the vessel, is included to scale the wall tension accordingly.

Blood flow

To compute vascular blood flow, we assume that the model afferent arteriole is connected in series to a pre-afferent arteriolar resistor Ω_{RA} and a post-afferent arteriolar resistor Ω_{EA} ; see inset in Fig. 4.1. The overall resistance of the model afferent arteriole is computed from the radius profile

$$\Omega_{AA} = \frac{8\mu_{AA}}{\pi} \int_0^{L_{AA}} \frac{dz}{R_{AA}(z)^4}, \quad (4.13)$$

where μ_{AA} denotes blood viscosity.

The perfusion pressure P_{RA} is assumed known *a priori*. The post-efferent arteriolar pressure $P_{EA,\text{end}}$ is kept constant at 0 mmHg. We assume simple Poiseuille flow so that arteriolar flow can be computed from the pressure drop along the afferent arteriole and the arteriolar resistance

$$Q_{AA} = \frac{P_{RA} - P_{AA}(t, L_{AA})}{\Omega_{RA} + \Omega_{AA}}. \quad (4.14)$$

Along the post-glomerular vascular segment, blood flow is given by the difference between arteriolar flow and SNGFR, and is related to pressure drop and vascular resistance as follows:

$$Q_{AA} - Q_F = \frac{P_{GL}(t, L_{GL}) - P_{EA,\text{end}}}{\Omega_{EA}}. \quad (4.15)$$

where $P_{\text{GL}}(t, L_{\text{GL}})$ is the hydrostatic pressure at the end of the glomerular capillary (see below). The relation between $P_{\text{AA}}(t, L_{\text{AA}})$ and $P_{\text{GL}}(t, L_{\text{GL}})$ is described in the following subsection. The values of Ω_{RA} and Ω_{EA} are chosen such that in the base case they account for 5% and 50% of the pressure drop $P_{\text{RA}} - P_{\text{EA, end}}$, respectively.

Blood pressure at the entrance of the afferent arteriole is $P_0 = P_{\text{RA}} - Q_{\text{AA}}\Omega_{\text{RA}}$, and the pressure gradient along the arteriolar lumen is given by the Poiseuille equation

$$\frac{\partial P_{\text{AA}}}{\partial z} = -\frac{8\mu_{\text{AA}}}{\pi R_{\text{AA}}^4} Q_{\text{AA}}. \quad (4.16)$$

4.2.2 Glomerulus submodel

To model glomerular filtration, we adopt the model developed by Deen et al. [41]. The glomerulus is represented as a single capillary extending from $y = 0$ to $y = L_{\text{GL}}$, with the two end-points corresponding to the connections with the afferent and efferent arterioles, respectively. Let Q_{GL} and C_{GL} denote the plasma flow rate and plasma protein concentration, respectively. Based on conservation of plasma mass, we have

$$\frac{\partial Q_{\text{GL}}}{\partial y} = -K_f \left(P_{\text{GL}} - P_{\text{F}} - \pi \right), \quad (4.17)$$

where K_f is the ultrafiltration coefficient. P_{GL} is the hydrostatic pressure, assumed to decrease linearly along the capillary $P_{\text{GL}} = P_{\text{AA}}(t, L_{\text{AA}}) - y\Delta P_{\text{GL}}/L_{\text{GL}}$, where ΔP_{GL} is constant. P_{F} denotes the proximal tubule inflow pressure (computed in the subsection below), and π denotes colloid osmotic pressure

$$\pi = \alpha_{\text{GL1}} C_{\text{GL}} + \alpha_{\text{GL2}} C_{\text{GL}}^2. \quad (4.18)$$

Conservation of protein yields $C_{\text{GL}}(t, y)Q_{\text{GL}}(t, y) = C_{\text{GL}}(t, 0)Q_{\text{GL}}(t, 0)$, which together with Eq. (4.17) results in

$$\frac{\partial C_{\text{GL}}}{\partial y} = \frac{K_f}{Q_{\text{GL}}(t, 0)} \frac{C_{\text{GL}}^2(t, 0)}{C_{\text{GL}}(t, 0)} \left(P_{\text{GL}} - P_{\text{F}} - \pi \right). \quad (4.19)$$

Plasma protein concentration entering the glomerulus is assumed fixed at 5.5 g/dl. Plasma enters at a rate determined by hematocrit Ht and arteriolar blood flow

$$Q_{\text{GL}}(0, t) = (1 - Ht)Q_{\text{AA}}(t). \quad (4.20)$$

Integrating Eq. (4.19), one obtains $C_{\text{GL}}(L_{\text{GL}}, t)$, which is used to compute $Q_{\text{GL}}(L_{\text{GL}}, t)$ from the conservation of plasma mass. SNGFR is given by

$$Q_{\text{F}}(t) = Q_{\text{GL}}(0, t) - Q_{\text{GL}}(L_{\text{GL}}, t). \quad (4.21)$$

4.2.3 Tubule submodel

The tubule model, based on a previously-applied TGF model [90], represents a proximal tubule followed by a short loop of Henle, extending from $x = 0$ (connection with the glomerulus) to $x = L_{\text{TB}}$ (site of macula densa). More specifically, the tubule model comprises the proximal convoluted tubule (5 mm), proximal straight tubule (2.5 mm), descending limb (1.5 mm), and thick ascending limb (5 mm) (see Fig. 4.1).

The model predicts intratubular pressure (P_{TB}), water flow rate (Q_{TB}), and Cl^- concentration (C_{TB}). Tubular walls are assumed to be compliant, with a radius that depends passively on transmural pressure gradient

$$R_{\text{TB}} = \alpha_{\text{TB}}(P_{\text{TB}} - P_{\text{ext}}) + \beta_{\text{TB}}, \quad (4.22)$$

where α_{TB} characterizes tubular compliance, and β_{TB} is the unpressurized radius.

Water transport

Tubular water flow is assumed to be pressure driven. The proximal tubule and the initial segment of the descending limb of Henle's loop are water permeable. Taking the transmural water flux Φ_{TB} into account, pressure and flow rate along the model

nephron are given by

$$\frac{\partial P_{\text{TB}}}{\partial x} = -\frac{8\mu_{\text{TB}}}{\pi R_{\text{TB}}^4} Q_{\text{TB}}, \quad (4.23)$$

$$\frac{\partial Q_{\text{TB}}}{\partial x} = -2\pi R_{\text{TB}} \frac{\partial R_{\text{TB}}}{\partial t} - \Phi_{\text{TB}}. \quad (4.24)$$

At the site of macula densa, the model tubule is connected to a resistance Ω_{DT} , at the end of which pressure is assumed to be fixed at $P_{\text{DT, end}} = 2$ mmHg. Thus, tubular fluid pressure and flow at the macula densa are related by

$$P_{\text{TB}}(L_{\text{TB}}, t) = P_{\text{DT, end}} + Q_{\text{TB}}(L_{\text{TB}}, t)\Omega_{\text{DT}}. \quad (4.25)$$

Micropuncture studies indicate a strong passive dependence of distal tubule's resistance on pressure [32]. Consequently, Ω_{DT} is modeled with a sigmoidal dependence on intratubular pressure

$$\Omega_{\text{DT}} = \Omega_{\text{DT, ref}} \left(1 - \tanh \left(\frac{P_{\text{DT}} - 4.5}{1.16} \right) \right), \quad (4.26)$$

where P_{DT} (given in mmHg) is the average of $P_{\text{TB}}(t, L_{\text{TB}})$ and $P_{\text{DT, end}}$.

Transmural water flux depends on SNGFR and on perfusion pressure

$$\Phi_{\text{TB}} = S_{\text{GTB}}(Q_{\text{F}}) S_{\text{PN}}(P_{\text{RA}}) \Phi_{\text{TB, base}}, \quad (4.27)$$

where $\Phi_{\text{TB, base}}$ is the baseline water flux profile. The factor S_{GTB} models glomerotubular balance [156, 158]

$$S_{\text{GTB}}(Q_{\text{F}}) = \frac{1}{1 + 0.7 \left(\frac{30}{Q_{\text{F}}} - 1 \right)}, \quad (4.28)$$

where Q_{F} is given in nl/min. The second factor S_{PN} accounts for pressure natriuresis, where proximal tubular water reabsorption decreases when perfusion pressure increases,

$$S_{\text{PN}}(P_{\text{RA}}) = 1 - 0.45 \left(\frac{\max(P_{\text{RA}}, 80)}{100} - 1 \right), \quad (4.29)$$

where P_{RA} is in mmHg. The slope -0.45 is chosen so that proximal tubule reabsorption is reduced by 55% when perfusion pressure is raised to 200 mmHg.

Chloride transport

Chloride concentration along the tubule is given by conservation of mass

$$\frac{\partial}{\partial t} (\pi R_{\text{TB}}^2 C_{\text{TB}}) = -\frac{\partial}{\partial x} (Q_{\text{TB}} C_{\text{TB}}) - 2\pi R_{\text{TB,ss}} \left(\frac{V_{\text{max}} C_{\text{TB}}}{K_{\text{M}} + C_{\text{TB}}} + \kappa_{\text{TB}} (C_{\text{TB}} - C_{\text{TB,ext}}) \right)$$

where $R_{\text{TB,ss}}$ is the steady-state tubular radius. Interstitial Cl^- concentration, denoted $C_{\text{TB,ext}}$, is set to 115 mM in the cortex and increases to 275 mM at the outer-inner medullary boundary [94]. The first term in the last pair of parentheses corresponds to active solute transport characterized by Michaelis-Menten-like kinetics, and the second term represents transepithelial diffusion with transmural permeability κ_{TB} . Strictly speaking, Na^+ ion is actively transported via the Na^+/K^+ -ATP pump, with Cl^- ion transported passively through the basolateral membrane. On the apical side, the NKCC2 transporter binds one Na^+ ion for each K^+ or NH_4^+ ion plus two Cl^- ions. Thus, the Michaelis-Menten term in the above equation is an approximation, which appears to be sufficient. At the entrance of the proximal tubule ($x = 0$), tubular fluid $[\text{Cl}^-]$ is set to 115 mM.

To represent glomerulotubular balance, whereby the NaCl and water reabsorption along the proximal tubular varies *in tandem*, we assume that along the proximal tubule, maximum active NaCl transport V_{max} exhibits an analogous dependence upon SNGFR and perfusion pressure as the transmural water flux Φ_{TB} , given by

$$V_{\text{max}} = \left(1 + 0.65 \left(S_{\text{GTB}}(Q_{\text{F}}) - 1 \right) \right) \left(1 + 2 \left(S_{\text{PN}}(P_{\text{RA}}) - 1 \right) \right) V_{\text{max,base}}, \quad (4.30)$$

where $V_{\text{max,base}}$ is the baseline maximum transport rate along the proximal tubule.

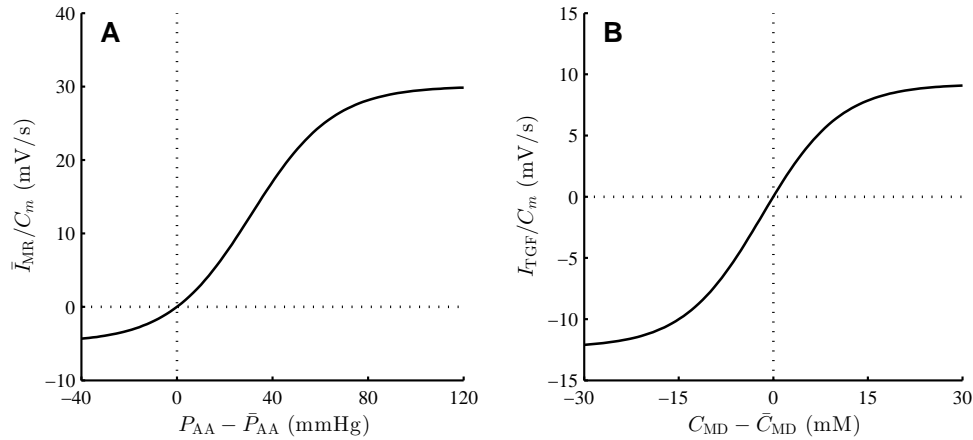


FIGURE 4.2: Autoregulatory currents, normalized by smooth muscle capacitance C_m . A, normalized myogenic response current; B, normalized TGF current.

4.2.4 Parameters

The model involves a large number of parameters. Parameters for the afferent arteriole model are adopted from Ref. [145]; parameters for the glomerular filtration model are based on Refs. [4, 120]; parameters for the tubule model are adopted from Ref. [90, 146]. Baseline profiles of selected parameters and the resulting steady-state solution for the tubule model are shown on Fig. 4.3. Parameter values not found in, or modified from, the above references are given in Tables 4.3–4.4.

The TGF current I_{TGF}^i has been constructed such that baseline open-loop TGF gain equals 3 and that SNGFR falls within the range 20–40 nl/min, [95, 70]. The target myogenic current \bar{I}_{MR}^i has been chosen as the lowest current necessary for the model to predict stable time-averaged SNGFR for perfusion pressures in the range 80–180 mmHg [73, 148]. The two currents are shown in Fig. 4.2.

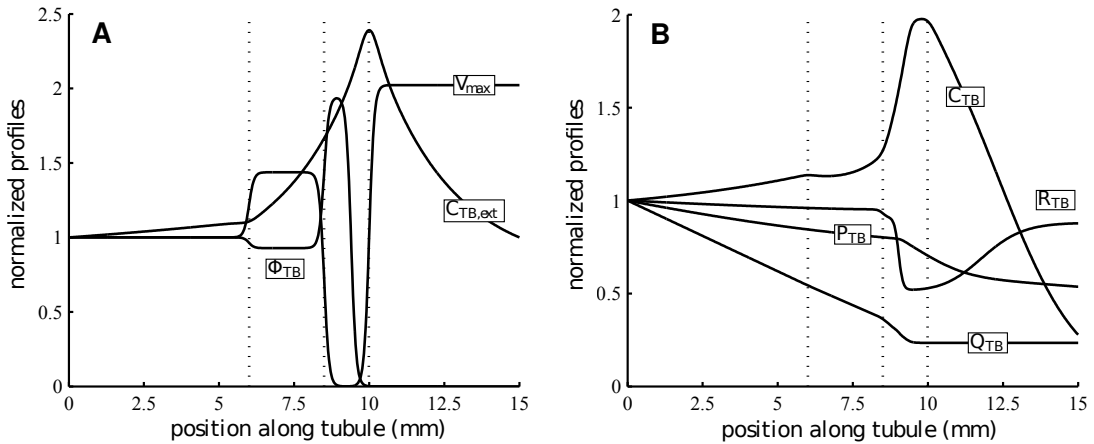


FIGURE 4.3: Baseline spatial profiles of model parameters and steady-state solution, normalized by respective boundary values. A, extratubular Cl^- concentration $C_{TB,ext}$, water reabsorption rate Φ_{TB} , and maximum active transport rate V_{max} . B, steady-state tubular pressure P_{TB} , flow rate Q_{TB} , radius R_{TB} , and intratubular Cl^- concentration C_{TB} , obtained for SNGFR 30 nl/min. Dotted lines indicate cortico-medullary boundary, outer-inner stripe boundary, and loop bend.

4.3 Results

4.3.1 Base-case predictions

The model equations were solved using baseline parameters and a steady perfusion pressure $P_{RA} = 100$ mmHg. The model predicts an arteriole flow that oscillates around 280 nl/min. The oscillations involve a slow, TGF-mediated oscillation at 36 mHz, and a fast, myogenic oscillation at 167 mHz; see Fig. 4.4. Both oscillations are initiated by periodic changes in afferent arteriole smooth muscle membrane potential, which translate into fluctuations in vascular tone. The resulting vasomotion alters the vascular resistance and blood delivery to the glomerulus, which transmits the fluctuations to SNGFR and downstream tubular transport. Time-averaged, minimum, maximum, and amplitude values of key model variables are listed in Table 4.5. A snapshot of the pressure, flow, and concentration profiles along the afferent arteriole and tubule, together with the corresponding envelopes (minimum and maximum values), is shown in Fig. 4.5.

When TGF gain, which is proportional to the slope of the TGF response curve at the operating point (Fig. 4.2B), is reduced to $< 60\%$ of its baseline value by decreasing s_{TGF} (Eq. (4.4)) accordingly, the TGF-mediated oscillations disappear, whereas the myogenic oscillations persist (not shown).

4.3.2 Assessment of autoregulation

To assess the individual contributions of the myogenic and TGF mechanisms to renal hemodynamic control, we conducted simulations in which we selectively inhibited these mechanism by setting the appropriate currents (I_{MR} and I_{TGF}) in Eq. (4.1) to zero. For each set of simulations, we compute time-averaged SNGFR and total arteriolar resistance for a range of steady renal perfusion pressure, from 60 to 200 mmHg. These results are shown in Fig. 4.6. In the base case (curve labelled “i”), SNGFR exhibits a wide plateau, where it stays within 5% of its baseline value, for perfusion pressures 80–180 mmHg [74, 36]. For the same range, afferent arteriole outflow pressure is also maintained close to its baseline value. In contrast, afferent arteriole inflow pressure increases inasmuch as perfusion pressure, wheres in the middle of the arteriole pressure varies between 65 and 120 mmHg, consistent with measurements by Carmines et al. [22].

Hydrostatic pressure profiles along the arteriolar length for perfusion pressures near the lower limit, center, and upper limit of the autoregulatory range are shown in Fig. 4.7. The profound pressure drop occurring at the terminal vascular segment is attributed in large part to the operation of TGF, which despite the gap junctional coupling of the smooth muscles that allows the TGF signal to spread thought the whole vessel, its effect is larger near its direct application site (i.e. distal 60 μm).

When both autoregulatory mechanisms are disabled (curve labelled “iv”), the SNGFR curve is predicted to rise with a slightly concave-upward shape as pressure increases, inasmuch as the higher blood pressure results in passive vasodilation, which

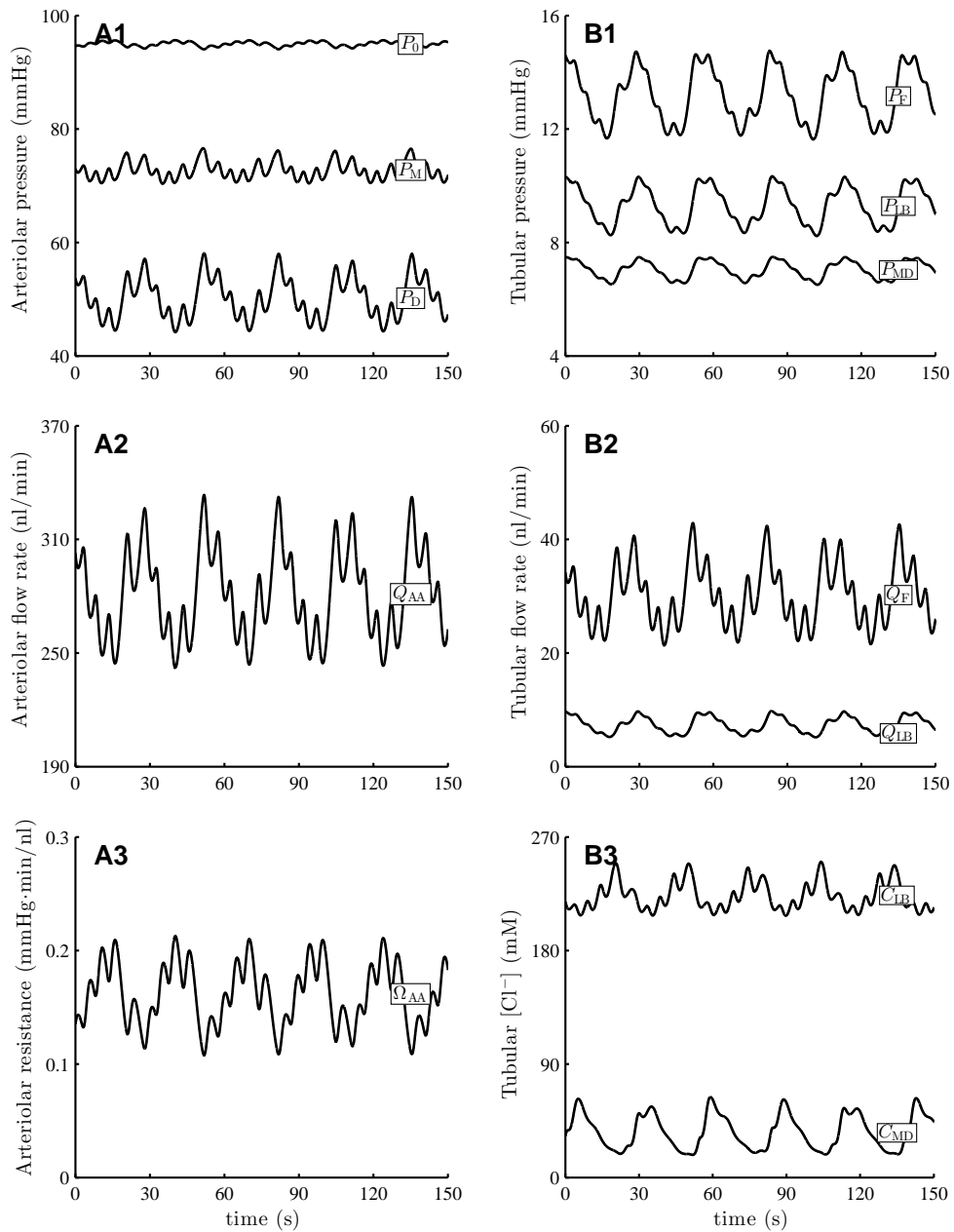


FIGURE 4.4: Time-course of baseline fluid pressure, fluid flow, arteriolar resistance, and tubular fluid $[Cl^-]$ at selected locations. Present are a slow, TGF mediated oscillation (period ~ 30 s) and a fast, myogenic oscillation (period ~ 6 s). Subscripts 0, M, D denote afferent arteriole entrance, middle, and exit; subscripts F, LB, MD denote proximal tubule entrance, loop bend, and macula densa.

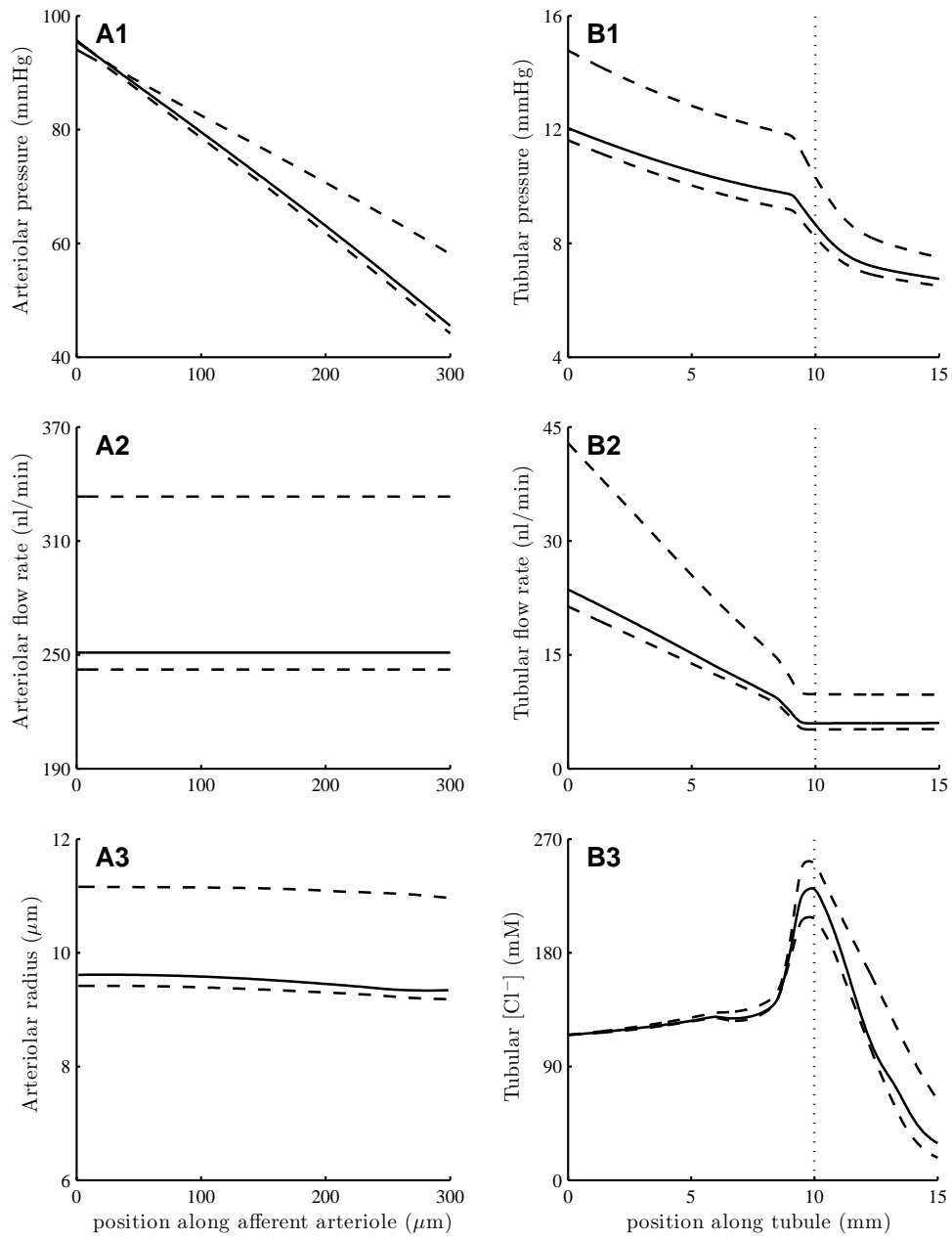


FIGURE 4.5: Base-case spatial profiles for afferent arteriole and tubular fluid pressure, fluid flow, arteriolar resistance, and tubular fluid $[\text{Cl}^-]$. Solid lines show profiles obtained at time 15 s; associated envelopes are shown in dashed lines. Dotted lines in panels B1–B3 indicate loop-bend position.

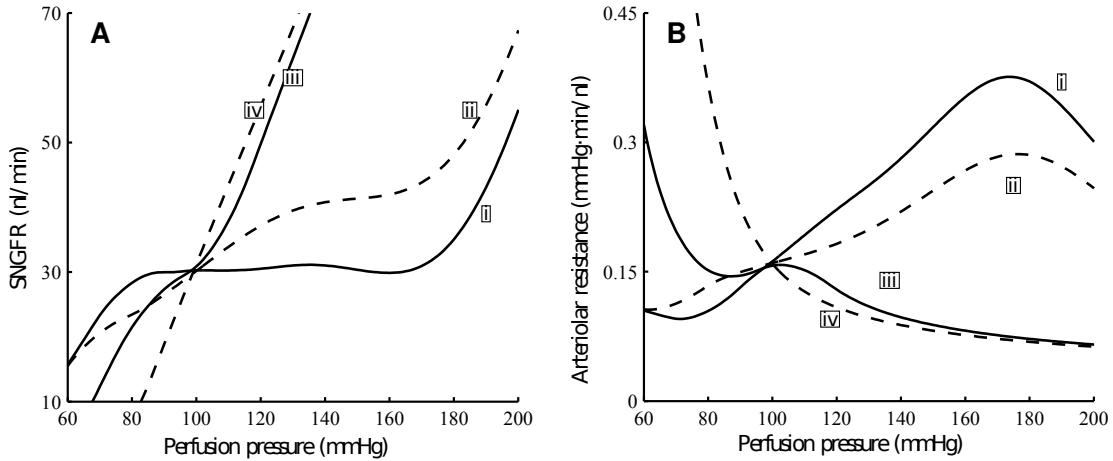


FIGURE 4.6: Time-averaged SNGFR (A) and vascular resistance (B) as functions of perfusion pressure. i, base case (full autoregulation); ii, TGF inhibited; iii, myogenic response inhibited; iv, no autoregulation. Results suggest that the contribution of myogenic response is substantially larger than TGF in stabilizing SNGFR.

lowers vascular resistance and yields a higher SNGFR. This result is consistent with findings by Dokkum et al. in the fawn-hooded rat [164].

When only TGF is inhibited, the model predicts a rise in SNGFR for perfusion pressure above baseline value, but the arteriolar resistance and SNGFR profiles generally follows the corresponding baseline profiles (see Fig. 4.6, curve labelled “ii”). In contrast, when myogenic response is inhibited, SNGFR deviates substantially from its baseline value when perfusion pressure exceeds 110 mmHg or falls below 80 mmHg (see Fig. 4.6, curve labelled “iii”). These results indicate that the contribution of TGF is significant only for a narrow range of pressure values around the baseline, where pressure natriuresis induces significant changes in macula densa $[Cl^-]$, thereby initiating a substantial TGF response and causing the appropriate changes in vascular tone to stabilize SNGFR. When perfusion pressure, and thus macula densa $[Cl^-]$, deviate substantially from baseline, however, the TGF signal becomes ineffective owing to its sigmoidal response (see Fig. 4.2B).

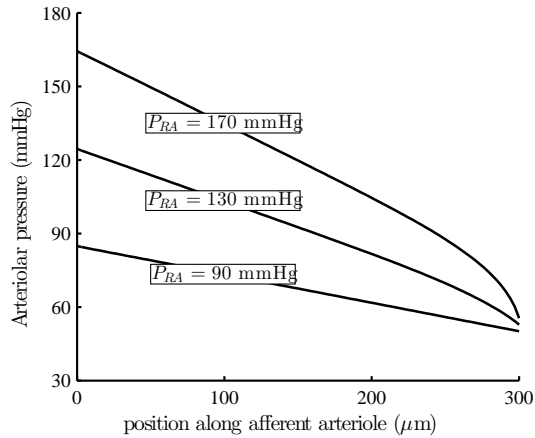


FIGURE 4.7: Time-averaged blood pressure profiles along the model afferent arteriole for perfusion pressures 90, 130, 170 mmHg. Afferent arteriole exit pressure is well autoregulated despite the large perfusion pressure variation.

4.3.3 Response to rapid pressure increase

We study the model's response to a rapid, step-like increase in input pressure from 80 to 160 mmHg. Figure 4.8 shows the imposed changes in the perfusion pressure and the resulting autoregulatory currents and vascular resistance time courses. For simplicity, the currents activating the myogenic response are shown only for the first and last smooth muscles of the afferent arteriole.

After an initial delay, the pressure step induces a rapid vasoconstriction mediated by nearly maximal I_{MR} and I_{TGF} (Fig. 4.8B). That constrictive response leads to an overshoot in vascular resistance seen at 25 s (Fig. 4.8C). A slower response follows, during which the proximal part of afferent arteriole remains constricted and absorbs most of the applied perturbation, whereas the distal vascular segment dilates and gradually returns to its reference dimension. During that phase, a transient oscillation is also observed that quickly dissipates after one period (~ 30 s), consistent with the biphasic responses reported by Just [82]. About 1.5 min after the pressure step, the system attains a steady state with a SNGFR of 35.7 nl/min, which is 19% higher than baseline, resulting in a rise in macula densa $[Cl^-]$ and a sustained constrictive

TGF response.

To determine the origin of the transient oscillation described above, we first note that the TGF current is transiently activated following the initial overshoot, which suggests that the oscillation may be TGF-mediated. To assess the validity of that hypothesis, we repeated the pressure-step simulation with TGF inhibited. The model predicts an impaired autoregulatory response that is, when assessed in terms of arteriolar resistance, $\sim 80\%$ of the baseline value. A similar initial overshoot in arteriolar resistance, with a smaller amplitude, is observed (see Fig. 4.8C). In contrast, in the absence of TGF, that overshoot in arteriolar resistance is followed by a gradual, monotonic decrease to its steady-state value. Hence, together these observations suggest that the transient post-overshoot oscillation observed in the base case is mediated by TGF.

Furthermore, the above results suggest that the contributions of TGF and myogenic mechanism to the overall vasoconstrictive response are approximately 20% and 80%, respectively, for the particular pressure step applied (80 to 160 mmHg). Note that the exact split depends on the size of the pressure step. Recall that the contribution of TGF to steady-state perfusion pressure perturbations is significant only within a narrow band of pressure (Fig. 4.6). Thus, if the beginning and end pressure values of the pressure step both fall within this pressure band, then the contribution of TGF to the vasoconstrictive response is significantly larger ($\sim 40\%$).

When the myogenic response is inhibited, with either TGF intact or similarly inhibited, the afferent arteriole responds to the pressure step-perturbation with a passive dilation (results not shown), resulting in no attenuation of the applied perturbation and thus a substantially higher SNGFR.

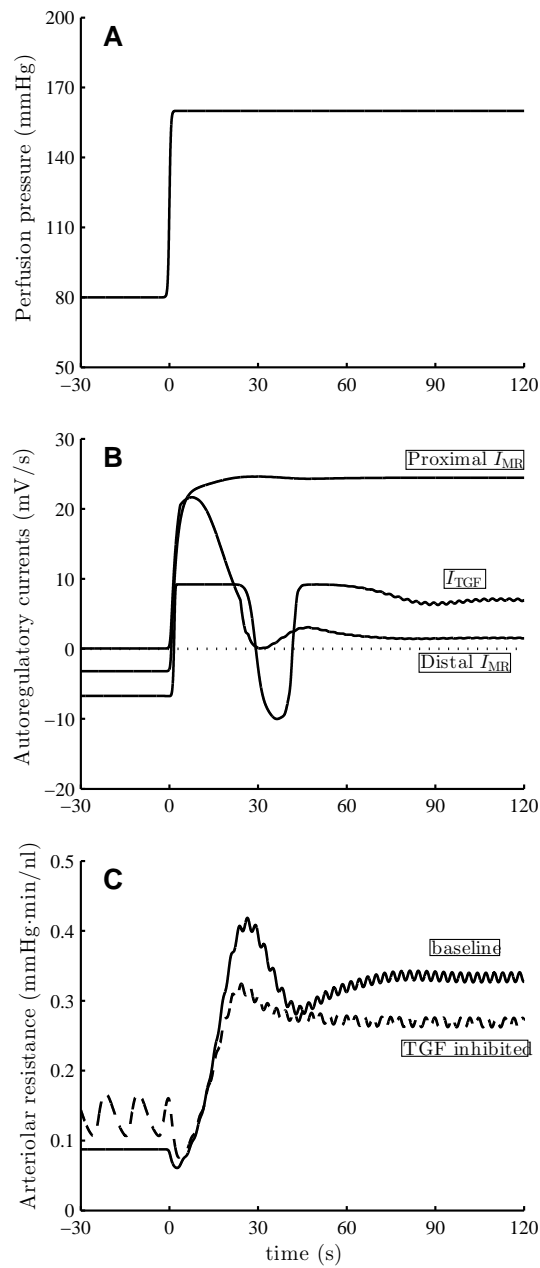


FIGURE 4.8: Model response to pressure up-step. A, input perfusion pressure. B, baseline myogenic and TGF currents. C, afferent arteriole resistance, for base case and with TGF inhibited. Vascular resistance shows a biphasic response: an overshoot, followed by a transient oscillation. That oscillation disappears when TGF is inhibited.

4.3.4 Rate-dependent response to pressure-ramp perturbations

Flemming et al. measured the response of renal vascular conductance to ramp-shaped changes in renal perfusion pressure [55]. Their results indicate that the changes in conductances are “markedly influenced by the velocity of pressure changes,” with faster pressure changes inducing larger conductance increases. Further, that effect is more pronounced during an increasing pressure-ramp as compared to a decreasing ramp. To assess the underlying mechanisms leading to such rate-dependent vasore-sponse we conducted the following simulations.

In separate simulations, we applied to the model’s perfusion pressure a fast ramp-shaped perturbation at 1 mmHg/s, and a slow ramp-shaped perturbation at 0.1 mmHg/s. These pressure perturbations and the predicted vascular conductances are shown in Figs. 4.9A1– B1. The model exhibits two-phase responses to all ramps, fast and slow, increasing and decreasing. When the perfusion pressure is approximately above 80 mmHg, the model maintains almost perfect autoregulation, with vascular conductance varying in the opposite direction of perfusion pressure. However, when the perfusion pressure drops below 80 mmHg, the model arteriole fails to sufficiently reduce wall tension to counteract the drop in pressure-induced tension. Consequently, vascular conductance varies *in tandem* with perfusion pressure.

Consistent with the measurements by Flemming et al. [55], conductance time-course associated with the fast ramp exhibits a marked asymmetry, but not for the slow-ramp response. Specifically, the asymmetric response is characterized by (i) a shorter passive response interval during the decreasing pressure-ramp (marked “ F_2 ” in Fig. 4.9B2) than during the increasing ramp (marked “ F_3 ”), and (ii) a higher maximum conductance (overshoot) during the increasing pressure-ramp as compared to the decreasing ramp. This asymmetry, which Flemming et al. refer to as “hysteresis,” was not further investigated in Ref. [55] is studied closely below.

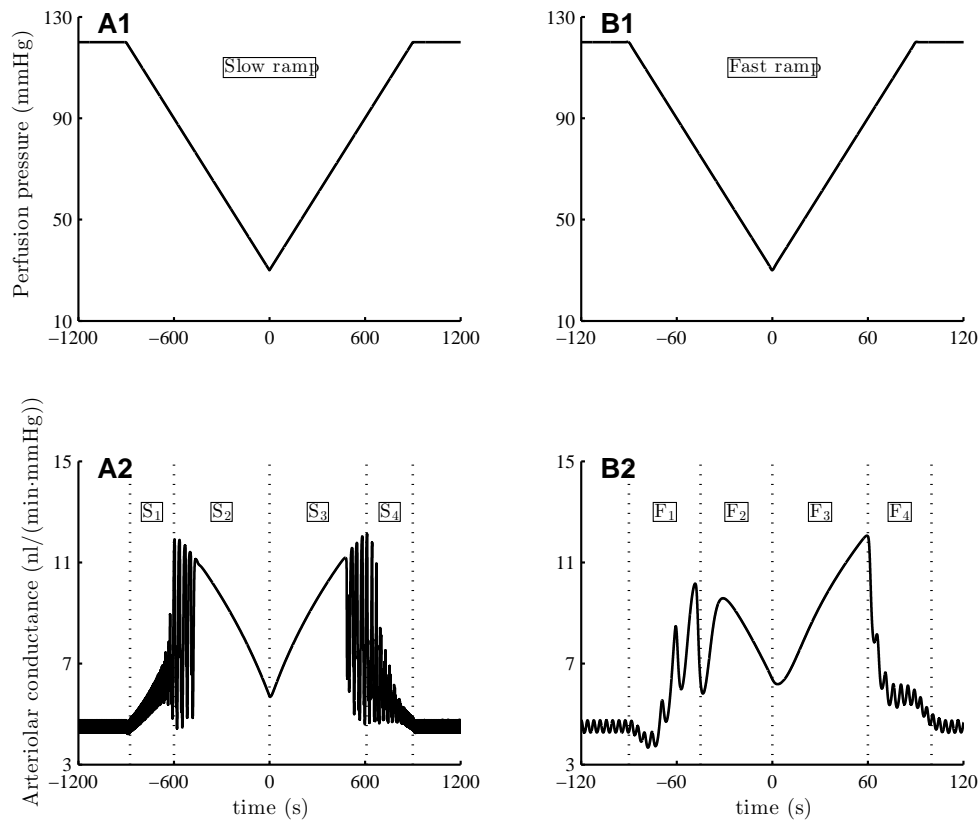


FIGURE 4.9: Model response to slow and fast pressure ramps. A1-B1, input perfusion pressure; note different scaling of time axes. A2-B2, arteriolar vascular conductance. In both cases, the decreasing pressure ramp induces a two-phase response in vascular conductance, with active vasodilation followed by passive vasoconstriction. An analogous two-phase response is observed along the increasing pressure ramp. The response is markedly asymmetric for the fast ramp.

Somewhat surprisingly, TGF appears to play no significant role in the observed conductance asymmetry. Simulations in which TGF was disabled predict qualitatively similar conductance time courses (results not shown).

The asymmetry in the peak conductances can be attributed, in large part, to the asymmetry in the kinetics of the myogenic response. To illustrate this, we compute the trajectories of myogenic current (I_{MR}) and perfusion pressure of the arteriolar smooth muscle cells. For simplicity, trajectories associated with the first cell are

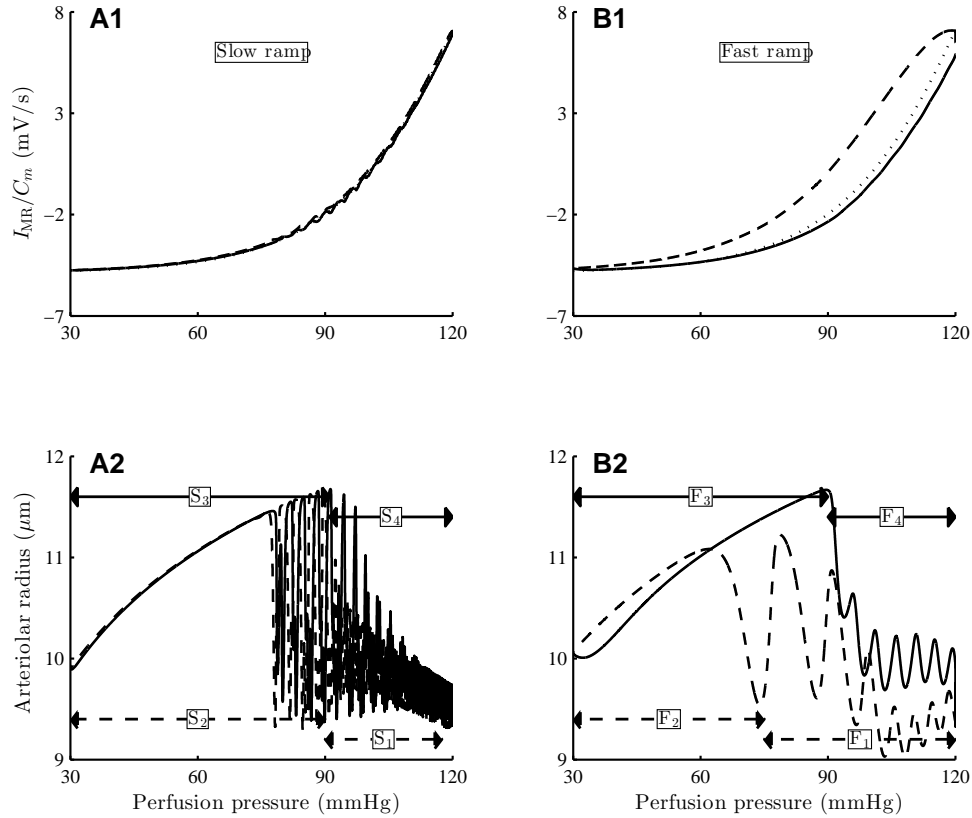


FIGURE 4.10: Model autoregulatory responses to slow and fast pressure ramps. Panels A1-B2 show normalized myogenic current (I_{MR}/C_m) as function of pressure; panels A2 and B2 show arteriolar radius. Solid lines, responses during increasing pressure ramp; dashed lines, responses during decreasing pressure ramp. Owing to the slower myogenic response to pressure reductions, the myogenic current fails to equilibrate during the decreasing fast pressure ramp.

shown on Fig. 4.10A1 – B1; the rest of the cell behave similarly and are not shown. For the slow ramp, the myogenic current trajectories produced by increasing and decreasing pressure ramps almost overlap (see Fig. 4.10A1), with the target myogenic current given by \bar{I}_{MR} (see Eq. (4.2)). In contrast, the increasing and decreasing fast ramps produce significantly different myogenic current trajectories (see Fig. 4.10B1). This mismatch is attributed to the rate-dependent kinetics of the myogenic mechanism, given in Eq. (4.2), which provides a faster response to increasing pressure than

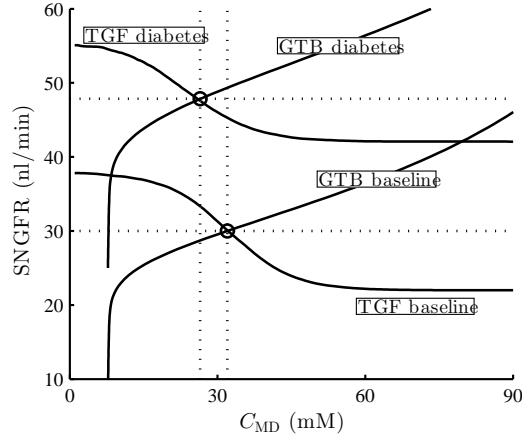


FIGURE 4.11: Glomerular hyperfiltration in diabetes. Solid lines: SNGFR under prescribed C_{MD} (labelled “TGF baseline” and “TGF diabetes,”) and C_{MD} under prescribed SNGFR (labelled “GTB baseline” and “GTB diabetes”). Baseline operating point is located at 30 nl/min and 32 mM, and diabetic operating point is at 48 nl/min and 27 mM (marked by circles).

to decreasing pressure. As a result, the myogenic current trajectory corresponding to the increasing pressure-ramp lies close to the target current, whereas the trajectory corresponding to the decreasing pressure ramp is situated much above the target current; see Fig. 4.10B1. The separation is much less noticeable with the slow ramp, in which case the myogenic current is given sufficient time to equilibrate. The trajectory of the arteriolar radius follows that of the myogenic current (Fig. 4.10A2 – B2).

4.3.5 Hemodynamics in diabetes

We conduct simulations to assess the extent to which functional impairment in afferent arteriole voltage-gated Ca^{2+} (VGC) channels observed in diabetic rats [23] diminishes the vasoconstrictive response, that causes glomerular hyperfiltration. The model represents the voltage-dependent distribution of open Ca^{2+} channel states by

$$m_{\infty}^i(v_m^i) = 0.5 \left(1 + \tanh \left(\frac{v_m^i - v_1}{v_2} \right) \right), \quad (4.31)$$

where $v_1 = -22.5$ mV is the voltage at which half of VGC channels are open in the unimpaired state, and $v_2 = 25$ mV determines the spread of the opening distribution. To represent VGC impairment, we increase v_1 to -20.7 mV.

At the onset of diabetes, the proximal tubule is known to hypertrophize [161]. As a result, water and salt reabsorption along the proximal tubule increases, a process which we simulate by increasing proximal tubule transmural water flux and maximum active transport rate by 78% and 150%, respectively. Diabetes is also associated with TGF resetting [157, 163], which we represent by lowering the operating macula densa $[\text{Cl}^-]$ (\bar{C}_{MD} in Eq. (4.4)) from its baseline value of 32 to 27 mM. Finally, the ultrafiltration coefficient K_f is increased by 20% from the baseline value [7].

With this set of modified parameters, the model predicts hyperfiltration in diabetes, with a SNGFR of 48 nl/min, 60% above base case. Together with a higher proximal tubule reabsorption, however, loop-bend flow rate remains at 7 nl/min, whereas macula densa $[\text{Cl}^-]$ is reduced by 5 mM, consistent with experimental results by Vallon and Thomson [162, 163].

We then conduct simulations to further investigate TGF efficiency in diabetes. First, we note that the open-loop TGF gain is given by the product of (i) the slope of the curve of SNGFR as a function of macula densa $[\text{Cl}^-]$, evaluated at the operating point, and (ii) the inverse of the slope of the curve of macula densa $[\text{Cl}^-]$ as a function of prescribed SNGFR, again evaluated at the operating point. Thus, to determine TGF gain in the diabetic model, we compute the curves in (i) and (ii); the results are shown in Fig. 4.11.

The curves labelled “TGF baseline” and “TGF diabetes” are obtained, for the base and the diabetic cases, respectively, with macula densa $[\text{Cl}^-]$ prescribed. Owing in large part to VGC impairment, the diabetic model predicts a substantial degree of hyperfiltration. As a result, the diabetes curve is shifted upward from baseline (see Fig. 4.11).

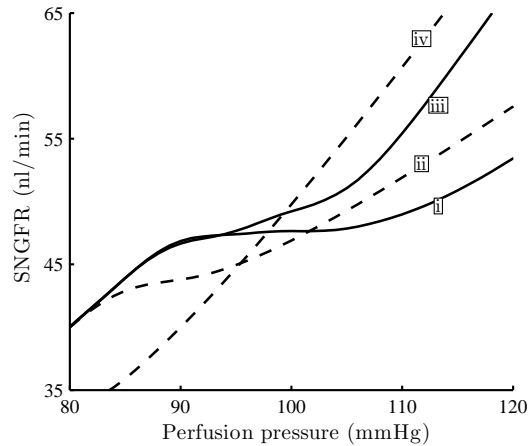


FIGURE 4.12: Autoregulatory plateaus of simulated diabetes. Time-averaged SNGFR as functions of perfusion pressure. i, base case (full autoregulation); ii, TGF inhibited; iii, myogenic response inhibited; iv, no autoregulation.

The curves labelled “GTB baseline” and “GTB diabetes” are obtained with SNGFR prescribed; that is, the ordinate (SNGFR) is the inputs, and abscissa (C_{MD}) is the predicted values (Fig. 4.11). These simulation results are presented in this manner to facilitate comparison with data in Ref. [163], figure 2. The upward shift of the diabetes curve results from the elevated proximal tubular reabsorption and the consequently lowered macula densa $[Cl^-]$.

Open-loop TGF gains for the base case and for the diabetes case can be computed by evaluating the slopes of the curves in Fig. 4.11 at the respective operating points (denoted by open circles) as described above. The baseline TGF gain is 3, and the diabetic TGF gain is reduced by 41% to 1.74. That reduction of TGF gain is attributable, in comparable degrees, to the impaired responsiveness of the afferent arteriole to the TGF signal, due to impairment of VGC channels, and to proximal tubule hypertrophy: the operating-point slope of the “TGF diabetes” curve is 26% lower than base case, whereas the corresponding slope of the “GTB diabetes” curve is 20% lower.

To assess renal autoregulation under diabetic conditions, we first consider steady

perfusion pressures and conducted simulations analogous to those used for Fig. 4.6. When both myogenic response and TGF are intact, the model predicts stable SNGFR for perfusion pressures between 85–115 mmHg, a plateau that is significantly narrower than the base case (compare Figs. 4.6 and 4.12). In particular, the ability of the myogenic response to stabilize SNGFR is significantly impaired in diabetes, as indicated by the shape of the SNGFR profile labelled “ii,” which corresponds to the case with TGF inhibited.

We then compare the model’s response to fluctuations in blood pressure under normal and diabetic conditions, by imposing a sinusoidal oscillations to a mean perfusion pressure of 100 mmHg. The applied oscillations have a frequency of 1 Hz and an amplitude of 60 mmHg (Fig. 4.13A). Both the normal and diabetic models respond with sustained vasoconstriction, owing to the faster myogenic response to pressure elevations than to pressure decreases [26, 144, 103], such that after an initial transient elevation, afferent arteriole outflow pressure returns to the level before the perturbation is applied (Fig. 4.13, panels B and C). As previously discussed, the diabetic model exhibits glomerular hyperfiltration, as can be seen in the higher peak and average pressures (compare panels B and C).

4.3.6 Sensitivity studies

The model comprises a large number of parameters. In the following set of sensitivity studies, we assess the degree to which the model’s autoregulation is impacted by variations in selected parameters which characterize the myogenic response and TGF.

We first vary the target myogenic current \bar{I}_{MR} by $\pm 10\%$ and $\pm 20\%$, as shown in Fig. 4.14. When \bar{I}_{MR} is reduced from its baseline value, the model fails to attain a stable SNGFR for any significant pressure range (see Fig. 4.14B). When \bar{I}_{MR} is raised above its baseline value, the model over-compensates, as expected; the deviation from the stable SNGFR value is particularly marked when TGF is inhibited (see

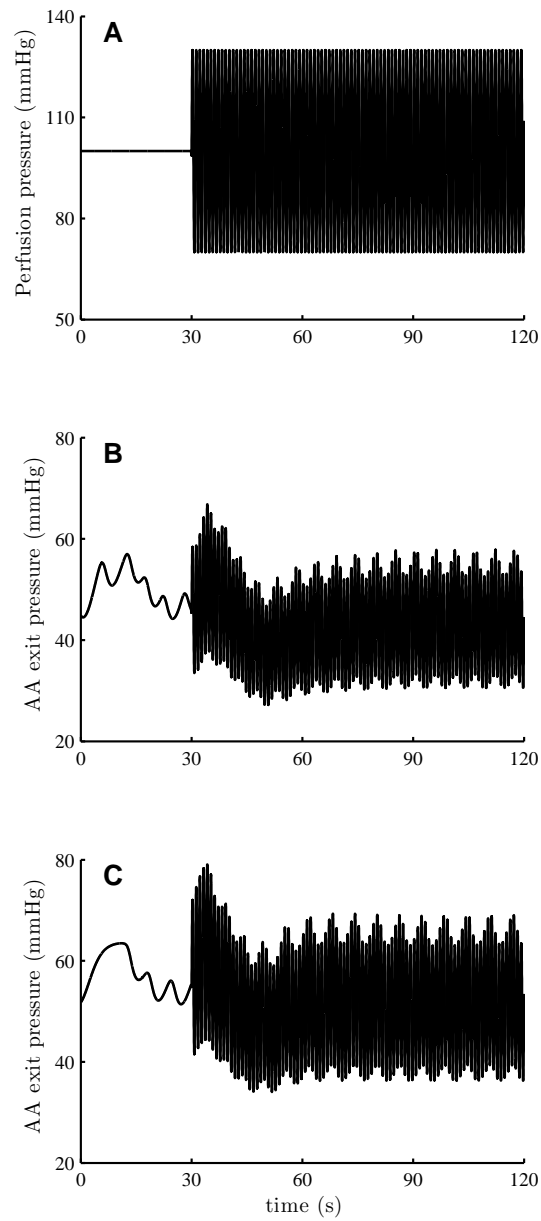


FIGURE 4.13: Simulations of normal and diabetic kidney's response to blood pressure fluctuations. A, perfusion pressure, with sinusoidal oscillations at 1 Hz. B, model response with normal physiological parameters; C, model response with diabetic parameters.

Figs. 4.14C).

Pressure natriuresis affects distal fluid and chloride delivery, thereby has a substantial impact on the TGF signal. Thus, we conduct simulations in which we altered the sensitivity of proximal tubular reabsorption to perfusion pressure (see Fig. 4.15). We observed that the resulting autoregulation plateaus are similar to base case; compare Figs. 4.6 and 4.15. This is not surprising because, as previously noted, TGF has a significant contribution to overall autoregulation over only a narrow band of perfusion pressure. Thus, it would be interesting to study how this pressure range is affected by the sensitivity of pressure natriuresis: To what extent does this range increase when the slope of the pressure natriuresis is halved? As shown in the inset of Fig. 4.15C, reducing the pressure natriuresis slope by half increases the pressure range slightly but does *not* double it. Owing to the nonlinear response of the afferent arteriole smooth muscles, pressure natriuresis has a larger (but still minor) effect on SNGFR at lower perfusion pressure. Indeed, for perfusion pressure higher than 110 mmHg, variations in pressure natriuresis response have negligible impact on overall autoregulation.

Another potentially interesting parameter is the TGF gain, which is proportional to s_{TGF} . As previously noted, TGF mediated oscillations in tubular flow are only predicted with sufficiently large s_{TGF} values. Varying s_{TGF} has little impact on overall autoregulation, measured by time-averaged SNGFR (results not shown).

4.4 Discussion

Given the wide ranges in which blood pressure varies in rat and other mammals, the relative stability of renal blood flow indicates the effectiveness of autoregulation. Multiple roles have been assigned to the importance of autoregulation. By varying the arteriolar muscle tone appropriately as blood pressure fluctuates, the myogenic response functions to maintain an approximately constant renal blood flow

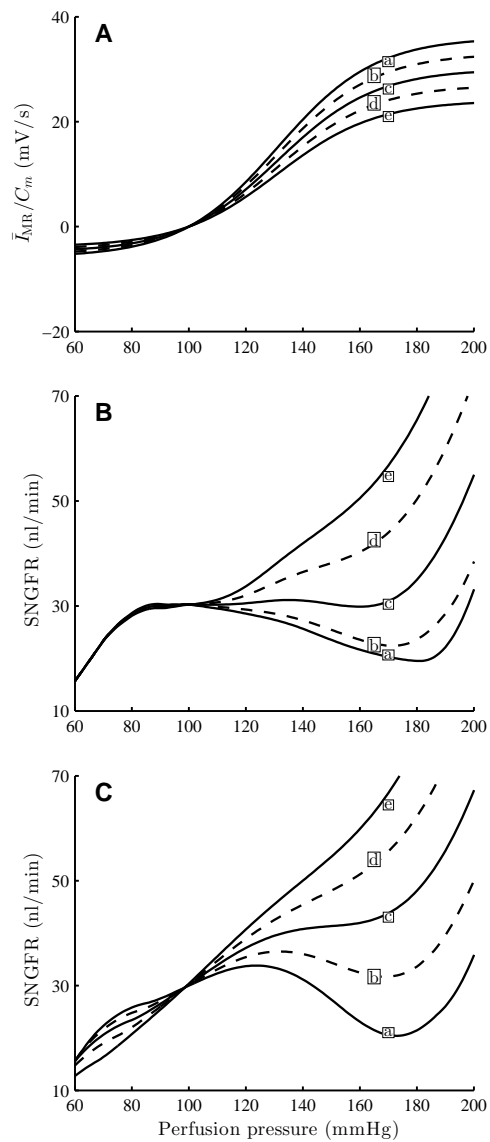


FIGURE 4.14: Sensitivity of model autoregulation effectiveness to variations in target myogenic current \bar{I}_{MR} . Simulations are conducted with \bar{I}_{MR} changed by $\pm 10\%$, $\pm 20\%$, panel A. B, SNGFR for a range of perfusion pressure with both myogenic and TGF intact; C, TGF inhibited.

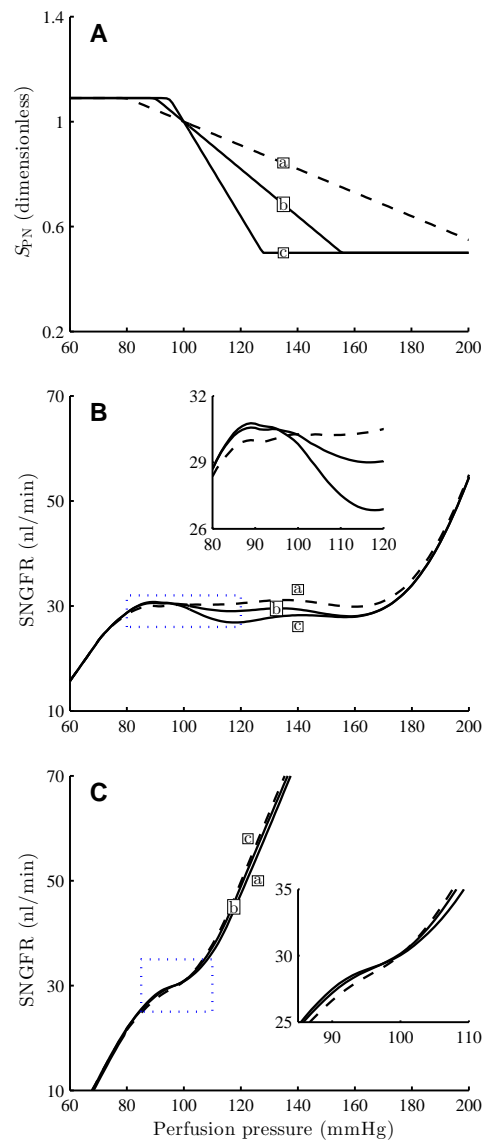


FIGURE 4.15: Sensitivity of TGF contribution to autoregulation to changes in pressure natriuresis response. Simulations were conducted with the slope of the pressure natriuresis response curve, denoted S_{PN} , scaled by 1/2 and 2 (panel A). With both myogenic response and TGF intact, the overall autoregulation is minimally affected by changes in S_{PN} (panel B). With myogenic response inhibited, a 50% reduction in S_{PN} increases, but not doubles, the range of perfusion pressures in which TGF has a significant contribution (panel C).

and glomerular filtration rate [73, 82, 107, 37]. For its part, TGF matches tubular load to the nephron's reabsorptive capability [82, 73, 126]. Together, the myogenic response and TGF regulate filtration and reabsorption, two processes that play a major role in determining the final urine production, and in regulating whole-body salt and water balance.

Another role of autoregulation is to preserve the glomerular structure, which is a high-pressure capillary bed prone to physical injury. Indeed, studies have identified a strong correlation between transmission of high systolic pressure to the glomerulus and renal injury [66]. Loutzenhiser et al. [13, 169, 107, 105, 106] suggested that, owing to the asymmetry in vasoconstriction and vasodilation myogenic response times, the afferent arteriole may sense systolic pressure at heart-beat frequency and respond with a sustained vasoconstriction when systolic pressure is elevated. Model simulations by our group and others agree with the hypothesis [27, 103, 145]. This protective function of autoregulation differs from its other function previously discussed, which regulates filtration rate and which is determined primarily by mean perfusion pressure, and not peak pressure. Under physiological conditions, where mean and systolic blood pressures vary *in tandem*, a myogenic response determined by systolic pressure would also regulate renal blood flow and glomerular filtration rate. However, under some pathophysiological conditions, where changes in systolic and mean blood pressures can be decoupled, an elevation in systolic pressure would result in myogenic vasoconstriction, even if mean perfusion pressure is unchanged or decreased.

The present model predicts that SNGFR is almost perfectly regulated for perfusion pressure within 80–180 mmHg (see Fig. 4.6), in good agreement with Refs. [37, 73]. The contribution of TGF is significant only within a narrow band of perfusion pressures (80–110 mmHg). For pressure variations within this band, TGF contributes to up to $\sim 40\%$ of the overall regulatory response, estimated by changes in vascular

resistance. However for perfusion pressures that deviate substantially from baseline, the sigmoidal response of the TGF response limits the effectiveness of the mechanism.

The present model considers an afferent arteriole and a loop of Henle in isolation. By no means do we wish to suggest that TGF in each nephron operates independently of other nephrons. Indeed, the TGF systems of nephrons whose afferent arterioles arise from a common interlobular artery are known to be coupled [69, 76], with the TGF signal propagating rapidly via the afferent arteriolar endothelium. It has been suggested that this interaction has the potential to augment the contribution of TGF to autoregulation [37]. Given that internephron TGF-mediated vascular cross-talk is generally constructive, it can increase the gain of the TGF response. However, the sigmoidal shape of the TGF response would still limit the contribution of TGF to the same narrow band of perfusion pressures.

The model predicts a biphasic response to a rapid pressure up-step (Fig. 4.8). That response is mediated by both TGF and myogenic mechanisms; indeed, when either is inhibited, the model predicts a monophasic response (Fig. 4.8). This result is consistent with the observations of Just [82], which assessed the time-courses of vascular resistance following a rapid pressure increase, under control conditions and under partial inhibition of TGF using furosemide. One discrepancy between the simulation results and Just's measurements is that the model's response to the pressure up-step is fully completed within 1.5 min, whereas Just observe that after 1.5 min, a small component of the response remains, which requires additional time to complete. The above discrepancy may provide evidence for the presence of other autoregulatory mechanisms, as proposed by Just [82], which are not represented in the present model.

4.4.1 *Comparison with previous modeling studies*

In the past decades, much modeling effort has been directed to investigating the mechanisms that control renal blood flow [113, 114, 120, 54]. Moore and Casellas [120] used a compartment-based integrative model to examine the hypothesis that synergistic interactions might occur between TGF and myogenic autoregulatory mechanisms. A limitation of that model is that it is formulated for steady state and does not predict transient responses. Their simulations predict strong ascending myogenic responses, in which TGF-mediated, locally-induced vasoconstriction raises upstream intravascular pressure and, as a result, triggers a myogenic response in the proximal arteriolar segments. In contrast, a modeling study by Feldberg and Holstein-Rathlou [54], as well as simulations using the present model (results not shown) suggest that the impact of ascending myogenic response is negligible.

Marsh et al. [113, 114, 115] present a detailed and comprehensive model of renal autoregulation that represents the dynamical interactions of TGF and myogenic mechanisms. That model shares several similarities with the present model, such as the representation of the afferent arteriolar smooth muscle intracellular dynamics and glomerular filtration. A major difference between the present work and that of Refs. [113, 114, 115] is that in the present model, the afferent arteriole responds directly to time-varying and time-independent perturbations in intravascular pressure, whereas the myogenic response in the model of Refs. [113, 114] is activated only by time-varying pressure perturbations. Thus, with the present model, we are able to assess the autoregulatory response to different steady-state perfusion pressures (Fig. 4.6). Additionally, pressure natriuresis is not represented in Refs. [113, 114, 115].

Cupples et al. [35] used a model that combines TGF and pressure natriuresis to assess the contribution of TGF to autoregulation. In that model, the sensitivity of

proximal tubule reabsorption to perfusion pressure was assumed to be much higher than the present study. Consequently, the contribution of TGF to autoregulation was found to be important over a range of perfusion pressures that is wider than in the present study. It is noteworthy that the model in Ref. [35] assumes a linear relationship between TGF signal and vascular resistance. In contrast, that relationship is nonlinear and indeed much more complex in the present model. Thus, results of our sensitivity studies indicate that the contribution of TGF may be much less sensitive to pressure natriuresis than previous models indicated.

The present model is an extension of an open-loop model previously developed by us [146]. The open-loop model focuses on signal transduction along the afferent arteriole and the nephron, and does not represent TGF. With the inclusion of both TGF and myogenic mechanisms in the present model, we are able to study the full autoregulatory process, and also to assess and compare their relative contributions under steady and time varying perfusion pressure.

4.4.2 Renal hemodynamics in diabetes mellitus

Alterations in glomerular hemodynamics critically contribute to the pathophysiology of diabetes. Thus, it is important to understand the mechanisms underlying altered autoregulation. Carmines et al. [23] found that depolarization-induced Ca^{2+} influx and the resulting increase in intracellular $[\text{Ca}^{2+}]$ are attenuated in the afferent arteriole of diabetic rats, and that those responses are rapidly restored by the normalization of extracellular glucose levels. Our model predicts that *minor* impairment of VGC function, characterized by a 1.8 mV increase in the half-max voltage associated with the VGCs, leads to significant attenuation in the afferent arteriole's myogenic response, resulting in glomerular hyperfiltration. In addition, fractional reabsorption of fluid and electrolytes in the proximal is increased in the early stages of diabetes in both humans [65] and experimental animals [6, 162]. Such increases

Table 4.1: Autoregulatory current parameters.

parameter	value	units
$I_{\text{MR,min}}$	-4.87	$\text{mV}\cdot\text{s}^{-1}$
$I_{\text{MR,max}}$	30.1	$\text{mV}\cdot\text{s}^{-1}$
s_{MR}	0.24	mmHg^{-1}
$I_{\text{TGF,min}}$	-12.3	$\text{mV}\cdot\text{s}^{-1}$
$I_{\text{TGF,max}}$	9.22	$\text{mV}\cdot\text{s}^{-1}$
s_{TGF}	0.85	mM^{-1}

may lower $[\text{Cl}^-]$ at the macula dense, thereby inducing a TGF signal that increases SNGFR (through vascular dilation), contributing to further alterations in glomerular hemodynamics in diabetes.

Model simulation results indicate that the VGC impairment leads to a substantial reduction in the blood pressure range in which SNGFR can be stabilized. Nonetheless, the diabetic model retains some, if not all, of its ability to buffer blood pressure fluctuations. When fast pressure oscillations are applied, the afferent arteriole smooth muscle cells of the diabetic model generate sustained vasoconstriction, despite the VGC impairment, thereby protecting the downstream glomerular capillaries from the elevated systolic pressure, albeit perhaps not to the same degree as the healthy kidney (Fig. 4.13).

Table 4.2: Model parameters.

parameter	value	units
Afferent arteriole submodel		
L_{AA}	303	μm
μ_{AA}	16.7	cP
Ω_{RA}	1.07	$\text{mmHg}\cdot\text{s}\cdot\text{nl}^{-1}$
Ω_{EA}	12.0	$\text{mmHg}\cdot\text{s}\cdot\text{nl}^{-1}$
τ_c	675	$\text{mmHg}\cdot\text{s}$
k_ψ	0.32	s^{-1}
k_{Ca}	190	s^{-1}
α_{Ca}	96.6	nM/fC
K_d	10^3	nM
B_T	10^5	nM
c_M	400	nM
ψ_M	0.55	-
Glomerulus submodel		
Ht	0.45	-
ΔP_{GL}	3.00	mmHg
K_f	2.14	$\text{nl}\cdot\text{min}^{-1}\cdot\text{mmHg}^{-1}$
α_{GL1}	1.63	$\text{mmHg}\cdot\text{dl}\cdot\text{g}^{-1}$
α_{GL2}	0.29	$\text{mmHg}\cdot\text{dl}^2\cdot\text{g}^{-2}$
Tubule submodel		
L_{TB}	15	mm
$\Omega_{DT,ref}$	42.9	$\text{mmHg}\cdot\text{s}\cdot\text{nl}^{-1}$
μ_{TB}	0.72	cP
K_M	70	mM

Table 4.3: Muscle mechanics parameters.

parameter	value	units
$C_{pass,0}$	18.2	$\text{cm}\cdot\text{mmHg}$
$C_{pass,1}$	9.76	-
$C_{act,0}$	39.7	$\text{cm}\cdot\text{mmHg}$
$C_{act,1}$	1.00	-
$C_{act,2}$	0.54	-
$R_{AA,c}$	13.0	μm

Table 4.4: Tubular parameter profiles.

position	$0 < x < 6$	$6 < x < 8.5$	$8.5 < x < 10$	$10 < x < 15$	mm
α_{TB}	0.23	0.23	0.13	0.13	$\mu\text{m}\cdot\text{mmHg}^{-1}$
$\Phi_{\text{TB,base}}$	22.8	21.2	44.2	0	$\text{nl}\cdot\text{min}^{-1}\cdot\text{cm}^{-1}$
$V_{\text{max,base}}$	8.00	11.5	0	16.2	$\text{nmol}\cdot\text{s}^{-1}\cdot\text{cm}^{-2}$
κ_{TB}	1.00	1.00	0.15	0.15	$\mu\text{m}\cdot\text{s}^{-1}$

position	$x = 0$	$x = 6$	$x = 8.5$	$x = 10$	$x = 15$	mm
β_{TB}	9.60	9.60	9.60	5.50	9.75	μm
$C_{\text{TB,ext}}$	115	127	191	275	115	mM

Table 4.5: Baseline results obtained for steady perfusion pressure 100 mmHg. P , Q , C denote pressure, flow rate, and $[\text{Cl}^-]$, respectively. Subscripts 0, M, D denote afferent arteriole entrance, midpoint, and exit; subscripts F, LB, MD denote proximal tubule entrance, loop bend, and macula densa.

	average	maximum	minimum	amplitude	units
P_0	95.0	95.7	94.1	0.81	mmHg
P_M	72.8	76.6	70.4	3.14	mmHg
P_D	50.2	58.1	44.2	6.96	mmHg
Q_{AA}	281	333	242	45.6	nl/min
P_F	13.2	14.8	11.6	1.58	mmHg
P_{LB}	9.28	10.4	8.22	1.06	mmHg
P_{MD}	7.03	7.50	6.51	0.49	mmHg
Q_F	30.2	43.0	21.4	10.8	nl/min
Q_{LB}	7.31	9.80	5.16	2.32	nl/min
Q_{MD}	7.31	9.74	5.22	2.26	nl/min
C_{LB}	224	251	207	21.7	mM
C_{MD}	35.4	63.8	17.8	23.0	mM

Assessment of Renal Oxygenation in Cardiopulmonary Bypass

5.1 Introduction

A prevalent complication of surgical procedures that require cardiopulmonary bypass (CPB) is acute kidney injury (AKI) [85]. Even mild AKI following CPB surgery is prognostically important, being associated with a more than 4-fold increase in the risk of in-hospital death [85] as well as extended hospital stays through additional complications [85]. When AKI is severe enough to require renal replacement therapy (in 1–2% of CPB surgery patients), mortality rate exceeds 60% [111].

Renal hypoxia might be an important pathway in the development of AKI during CPB surgery, particularly if there is a mis-match between changes in renal oxygen delivery and oxygen consumption [51]. Renal oxygen delivery is mainly determined by renal blood flow (RBF) [51]. Renal oxygen consumption is mainly driven by the metabolic work of tubular sodium reabsorption, which in turn is largely driven by the filtered load of sodium, and thus glomerular filtration rate (GFR) [51]. Arterial pressure is often set to a low level during CPB (50–70 mmHg). Further, autoregula-

tion of RBF and GFR is compromised [1]. Consequently, changes in RBF and GFR during CPB will likely have a major impact on the risk of AKI.

Multiple factors compromise renal autoregulation during CPB. Firstly, the CPB circuit must be primed with a cell free solution, resulting in hemodilution [139]. The potential importance of hemodilution is evidenced by the observation that a hematocrit of less than 21% is an independent risk factor for AKI after cardiac surgery [139]. Secondly, tissue perfusion during CPB is non-pulsatile. The pulsatility of renal arterial pressure is a critical determinant of the myogenic component of the autoregulatory response, as evidenced by experimental findings and simulations from mathematical models [106, 27, 145]. Collectively, these data indicate that oscillations in renal arterial pressure induced by the beating heart lead to sustained vasoconstriction of the afferent arteriole.

Thus, it seems reasonable to hypothesize that renal ischemia and dysfunction of glomerular filtration could arise during CPB as result of complex interactions between the effects of altered blood viscosity due to hemodilution and hypothermia, the absence of pulsatility of blood flow, and hypotension. Clearly, our ability to study these phenomena in the clinical situation is limited. Our ability to study them in intact animals is also limited, because of the number of experimental conditions that would need to be studied in order to allow such interactions to be fully interrogated. Therefore, in the current study we have utilized a computational model to examine how the renal hemodynamic changes during CPB might lead to renal circulatory dysfunction.

5.2 Methods

The model kidney is assumed to consist of identical nephrovascular units, with each consisting of a nephron, and the attached glomerulus, afferent and efferent arterioles. To represent such unit we adopt the model of Chapter 4. In each unit, hemodynamic

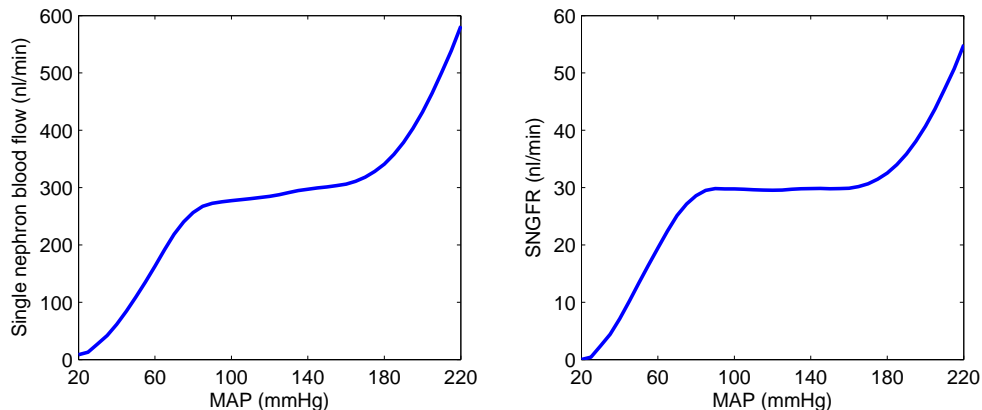


FIGURE 5.1: Single nephron autoregulatory plateaus for pulsatile flow. Plateau values for single nephron blood flow and SNGFR are 280 and 30 nl/min, respectively.

control is provided by the myogenic response and tubuloglomerular feedback. Renal oxygen delivery and oxygen consumption is computed separately for the cortex and medulla. The former is determined by blood flow and the latter by NaCl reabsorption. Details are described in the next sections.

5.2.1 Representative nephrovascular unit

The nephrovascular model presented in Chapter 4 has been adopted with the modifications described below, which concerns heart beat, hypotension, variable hematocrit, and variable temperature.

Perfusion pressure

Perfusion pressure P_{RA} is assumed to be time dependent:

$$P_{RA} = P_m + P_c \sin(2\pi f_c t) \quad (5.1)$$

where P_m is mean arterial pressure (MAP), f_c is heart rate, and P_c is the induced amplitude. For all simulations f_c is set to 6 Hz. Pulse amplitude P_c is either 0 (no pulsation) or 20 mmHg (pulsation). These values are based on data for the rat [62, 16, 5].

Parameters for the myogenic response are chosen such that with pulsation, the model predicts autoregulatory plateaus that fall within 80–180 mmHg (see Figure 5.1), consistent with the generally accepted range e.g. [148, 73, 37]. This is achieved by changing the reference pressure of the activation of the myogenic response \bar{P}_{AA}^i (see Eq. (4.3)) from 95–50 to 104.75–55.51 mmHg (values denote afferent arteriole entrance and exit, respectively).

During CPB, renal perfusion pressure drops below the lower limit of autoregulation. As a result, glomerular pressure and thus efferent arteriole pressure drop significantly below the physiologic levels, which in turn results in vasoconstriction of the post glomerular vasculature. In order to account for the phenomenon, efferent arteriole luminal radius R_{EA} is evaluated in a manner similar to afferent arteriole:

$$\frac{dR_{EA}}{dt} = \frac{1}{\tau_c} \left(T_P - \xi_{EA} T_{wall} \right) \quad (5.2)$$

where $\xi_{EA} = 0.30$. The reference radius $R_{EA,c}$ is set at 9.18 μm . The pressure that induces T_P is evaluated by the average of glomerular capillary pressure and $P_{EA,end}$. Since the efferent arteriole is myogenically inactive, we assumed a constant cross-bridge formation value ω_{EA} of 0.10. The rest of the parameters defining the strength of T_{wall} are the same as in the afferent arteriole (see Eqs. (4.9)–(4.10)).

When perfusion pressure is pulsatile, a portion of the cardiac oscillations reaches the glomerular capillaries [16, 5]. In this case, plasma filtration, determined by Eq. (4.17), is driven by a waveform that consists of 3–4 wavelengths, based on the estimated transit time along the glomerular bed. Thus, glomerular filtration is expected to significantly damp the cardiac oscillations. To account for such damping, blood flow Q_{AA} and glomerular capillary pressure P_D (outputs of the vascular sub-

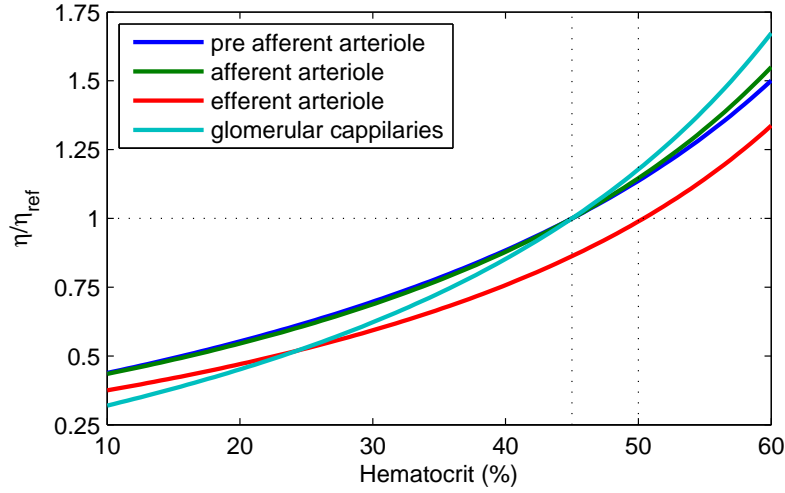


FIGURE 5.2: Blood viscosity η dependence on hematocrit. Pre- and post-glomerular reference blood viscosity η_{ref} equals blood viscosity of the associated segment at hematocrit values of 45% and 50%, respectively.

model) are passed through a linear low pass filter:

$$\frac{dQ_{AA}^*}{dt} = \frac{1}{\tau_{GL}} (Q_{AA} - Q_{AA}^*) \quad (5.3)$$

$$\frac{dP_D^*}{dt} = \frac{1}{\tau_{GL}} (P_D - P_D^*) \quad (5.4)$$

The effect of the above filter is to damp the high frequency oscillations in P_D and Q_{AA} by averaging them over the time interval $(t - \tau_{GL}, t)$. Single nephron glomerular filtration rate is computed by Q_{AA}^* and P_D^* , see Section 4.2.2 of Chapter 4. The time constant $\tau_{GL} = 0.61$ s is chosen according to the estimated transit time along the glomerular bed.

Hematocrit

Besides influencing the glomerular plasma flow, hematocrit also influences blood viscosity [132, 133]. To account for such influence, blood viscosity is evaluated according to the in vivo hematocrit–viscosity relation developed by Pries et al. in Ref. [134] (equation (9) therein). The influence of hematocrit on blood viscosity is shown on

Figure 5.2.

The application of the hematocrit–viscosity relation requires the assumption of luminal radii across the model vasculature. We assume the following: (i) pre afferent arteriole $120\ \mu\text{m}$, (ii) afferent arteriole $10\ \mu\text{m}$, (iii) glomerular capillaries $5\ \mu\text{m}$, and (iv) efferent arteriole $10\ \mu\text{m}$. These choices are based on Refs. [127, 24, 128]. Note that anatomically the pre afferent arteriole vasculature consists of several segments of different radii, all of which are significantly larger than $25\ \mu\text{m}$ [127]. Further, the viscosity law is insensitive to radii for that large vessels. So, the estimate in (i), which assumes a uniform radius for the whole pre afferent arteriole vasculature, likely provides a good description of the phenomenon.

Temperature

Temperature affects plasma viscosity [99, 153]. Due to the similarity in the composition of tubular fluid and plasma, it is natural to expect a similar relationship between temperature and tubular fluid’s viscosity. Further, if we assume that Darcy’s law or similar principles underlies glomerular filtration, it is natural to expect that the ultrafiltration coefficient K_f changes with temperature too. According to measurements in the rat kidney obtained under hypothermic conditions [18], temperature also affects: afferent and efferent arteriolar vascular tones, tubular water reabsorption, and tubular NaCl reabsorption.

Those effects have been incorporated in most cases phenomenologically as described below. Due to the sparsity of available data, temperature effects are modeled by linear functions fitted to data at 37°C (reference temperature) and 28°C (hypothermic temperature).

1. *Effect on afferent arteriole vascular tone.* We assume that afferent arteriole myocyte cytosolic Ca^{2+} increases with decreasing temperature. In particular, this is achieved by assuming that cytosolic Ca^{2+} extrusion rate, see Eq. (4.5),

decreases linearly with temperature. Fitting the model to the data reported in [18], the extrusion rate at 28°C has to be reduced by 20% relative to 37°C.

2. *Effect on efferent arteriole vascular tone.* We assume that efferent arteriole muscle activation increases linearly with temperature. Muscle activation at 28°C is 12% larger than at 37°C, [18].
3. *Plasma viscosity* increases linearly with decreasing temperature [99]. In particular, between 28°C and 37°C plasma viscosity increases by 25%.
4. The *ultrafiltration coefficient* K_f decreases linearly with decreasing temperature. To achieve agreement with [18], K_f at 28°C is decreased by only 5% relative to 37°C, a decrement that is 4 times smaller than what is predicted by Darcy's law, which assumes that K_f is inversely proportional to plasma viscosity.
5. *Tubular fluid viscosity* is assumed to increase more than plasma viscosity. Based on [18], hydrostatic pressure in Bowman's space at 28°C is nearly the same that at 37°C, which demands tubular fluid viscosity increases 3.6 times more than plasma viscosity.
6. *Effect on proximal tubule water reabsorption.* Under physiologic conditions, proximal tubule fractional water reabsorption changes in tandem with SNGFR [158, 156]. In contrast, cooling at 28°C results in almost no change, despite the apparent reduction of SNGFR. This phenomenon is captured by assuming that the efficiency index of glomerotubular balance, see Eq. (4.28), increases linearly with decreasing temperature from 0.70 at 37°C to 1.14 at 28°C.
7. *Effect on proximal tubule NaCl reabsorption.* Proximal tubule is assumed to reabsorb equal quantities of water and NaCl independently of temperature.

8. *Effect on Henle's loop NaCl reabsorption.* Along the thick ascending limb maximum transport rate $V_{max,TAL}$ is assumed to reduce linearly with decreasing temperature. Reference [18] reports GFR, urine flow rate and urine Na^+ concentration at 37°C and 28°C . Assuming that plasma Na^+ concentration is 150 mM independently of temperature, one estimates a reduction of absolute NaCl reabsorption between the temperatures 37°C and 28°C of 49%. To attain that reduction, we reduce $V_{max,TAL}$ by 56%.

5.2.2 Renal oxygen transport

Let Q_{AA} denote the single nephron blood flow as predicted by the nephrovascular model described in the previous section. Assuming that the kidney consists of N identical nephrons, whole kidney blood flow is given by:

$$Q_{blood}^{total} = NQ_{AA} \quad (5.5)$$

A portion of Q_{blood}^{total} is delivered to the cortex and the rest to the medulla. Thus:

$$Q_{blood}^{cortex} = q^{cortex} Q_{blood}^{total} \quad (5.6)$$

$$Q_{blood}^{medulla} = q^{medulla} Q_{blood}^{total} \quad (5.7)$$

Due to conservation $q^{cortex} + q^{medulla} = 1$. Since experimental observations of cortical and medullary blood flow do not give conclusive data of the exact details of regional autoregulation [51, 53, 130, 116], it is assumed that q^{cortex} and $q^{medulla}$ are independent of perfusion pressure. This is equivalent to assuming that medullary blood flow is autoregulated the same way as cortical blood flow, which in turn is autoregulated the same way as Q_{blood}^{total} .

There is agreement that the ratio $Q_{blood}^{medulla}/Q_{blood}^{cortex}$ is in the range 5–20%, for example see Ref. [138, 130, 10] and the references therein. In this study, we assume that $q^{cortex} = 0.90$ and $q^{medulla} = 0.10$.

Oxygen delivery

Let H denote the systemic hematocrit. Similar to blood flow, assume:

$$H^{cortex} = h^{cortex} H \quad (5.8)$$

$$H^{medulla} = h^{medulla} H \quad (5.9)$$

There is consensus that $h^{cortex} = 1$. Assuming that $H^{medulla}$ is approximated by the discharge hematocrit as estimated [174], we get $h^{medulla} = 0.80$.

Let D^{cortex} and $D^{medulla}$ denote cortical and medullary oxygen delivery. By the standard model [131] of oxygen transport:

$$D^{cortex} = C_{free} Q_{plasma}^{cortex} + C_{bound} Q_{RBC}^{cortex} \quad (5.10)$$

$$D^{medulla} = C_{free} Q_{plasma}^{medulla} + C_{bound} Q_{RBC}^{medulla} \quad (5.11)$$

Plasma and red blood cells flows are:

$$Q_{plasma}^{cortex} = (1 - H^{cortex}) Q_{blood}^{cortex} - Q_{filtered}^{cortex} \quad (5.12)$$

$$Q_{RBC}^{cortex} = H^{cortex} Q_{blood}^{cortex} \quad (5.13)$$

$$Q_{plasma}^{medulla} = (1 - H^{medulla}) Q_{blood}^{medulla} - Q_{filtered}^{medulla} \quad (5.14)$$

$$Q_{RBC}^{medulla} = H^{medulla} Q_{blood}^{medulla} \quad (5.15)$$

where $Q_{filtered}^{cortex}$ and $Q_{filtered}^{medulla}$ denote the glomerular filtration rates from the superficial and juxtamedullary nephrons, respectively. For this study are assumed:

$$Q_{filtered}^{cortex} = g^{cortex} N Q_F \quad (5.16)$$

$$Q_{filtered}^{medulla} = g^{medullary} N Q_F \quad (5.17)$$

where Q_F is SNGFR, which is predicted by the single nephron model. The constants $g^{cortex} = 0.84$ and $g^{medulla} = 0.16$ are chosen similar to Ref. [33], according to the estimated fraction of juxtamedullary to superficial nephrons in the rat kidney.

Kidney oxygen delivery is:

$$D^{total} = D^{cortex} + D^{medulla} \quad (5.18)$$

Free and bound oxygen concentrations are given by the standard [131] formulas:

$$C_{free} = \sigma_{plasma} P_{O_2} \quad (5.19)$$

$$C_{bound} = b_{Hb} c_{Hb} s_{Hb} \quad (5.20)$$

where σ_{plasma} is oxygen solubility in plasma, c_{Hb} is concentration of hemoglobin in erythrocytes, b_{Hb} is hemoglobin binding capacity, and s_{Hb} is the saturation modeled by the Hill equation:

$$s_{Hb} = \frac{P_{O_2}^n}{P_{50}^n + P_{O_2}^n} \quad (5.21)$$

The temperature dependence of hemoglobin saturation is estimated experimentally in [140] to be:

$$P_{50} = P_{50,ref} \exp\left(\frac{\alpha_T}{T_{ref} - T_0} - \frac{\alpha_T}{T - T_0}\right) \quad (5.22)$$

It has been experimentally validated that blood and plasma solubility is a constant fraction of water solubility independently of temperature [31, 30]. Therefore the temperature dependence of solubility is captured by assuming that σ_{plasma} scales according to the empirical equation given in [8]. Thus, solubility is evaluated as:

$$\sigma_{plasma} = \sigma_{plasma,ref} \exp\left(\frac{T_{ref} - T}{\beta_T}\right) \quad (5.23)$$

Parameter values are listed in table 5.1. The value of c_{Hb} has been estimated from unpublished data of Roger Evans, Department of Physiology, Monash University.

Oxygen consumption

Let T^{total} and $T^{medulla}$ denote the net rates of NaCl reabsorption from whole kidney and medulla, respectively. Assuming, as above, that the kidney consists of N identical nephrons, we get:

$$T^{total} = N J^{total} \quad (5.24)$$

$$T^{medulla} = N J^{medulla} \quad (5.25)$$

Table 5.1: Oxygen delivery parameter values.

parameter	value	units	reference
b_{Hb}	4	-	[57]
c_{Hb}	4.76	mM	-
n	2.5	-	[57]
$\sigma_{plasma,ref}$	1.34	$\mu\text{M}/\text{mmHg}$	[58]
$P_{50,ref}$	26	mmHg	[57]
T_{ref}	37	$^{\circ}\text{C}$	-
T_0	273	$^{\circ}\text{C}$	[140]
α_T	2146	$^{\circ}\text{C}$	[140]
β_T	53.65	$^{\circ}\text{C}$	[8]

where J^{total} and $J^{medulla}$ denote the corresponding single nephron rates computed for the whole model nephron and only the medullary part of it. In particular, J^{total} and $J^{medulla}$ consist of two parts: active and passive (back leak). In view of Section 4.2.3 of Chapter 4, those are given by the integrals of:

$$j_{act} = 2\pi R_{TB,ss} \frac{V_{max} C_{TB}}{K_M + C_{TB}} \quad (5.26)$$

$$j_{pass} = 2\pi R_{TB,ss} \kappa_{TB} (C_{TB} - C_{TB,ext}) \quad (5.27)$$

over the whole model nephron and only the medullary part of it.

Using a uniform transport efficiency along all nephron segments of 1 mol of O_2 for 28 mol of NaCl, similar to Ref. [52], we get:

$$V^{total} = \frac{T^{total}}{28} + V_{basal}^{total} \quad (5.28)$$

$$V^{medulla} = \frac{T^{medulla}}{28} + V_{basal}^{medulla} \quad (5.29)$$

where V_{basal}^{total} and $V_{basal}^{medulla}$ denote oxygen consumption that takes place independently of NaCl transport. In this study, V_{basal}^{total} and $V_{basal}^{medulla}$ are assumed independent of NaCl reabsorption.

Oxygen fractional extraction is given by:

$$F^{total} = \frac{V^{total}}{D^{total}} \quad (5.30)$$

$$F^{medulla} = \frac{V^{medulla}}{D^{medulla}} \quad (5.31)$$

Total basal oxygen consumption is set at $N \times 350$ pmol/min, which gives a baseline F^{total} of 20%, as it has been estimated experimentally in [52]. Medullary basal oxygen consumption is assumed to consist 4% of total basal consumption, according to modeling estimates of Brendan Fry and Anita Layton, Department of Mathematics, Duke University.

5.3 Results

Motivated by experimental and clinical data, Refs. [18, 1], we used the model to simulate the scenarios: (i) baseline, (ii) normothermia, (iii) hypothermia, (iv) pre CPB, (v) hypothermic CPB, (vi) CPB rewarming, and (vi) post CPB. A summary of the parameter values chosen for each scenario is given in Table 5.2.

The experimental scenarios (ii)–(iii) simulate only the effect of cooling on renal function. These scenarios are used to validate the underlying assumptions of section 5.2.1.

The clinical scenarios (iv)–(vii) are used to assess the renal function during CPB. Specifically, the pre CPB scenario simulates heart driven (pulsatile) flow with moderate hypotension that arises as a result of anesthesia. The hypothermic and rewarming CPB scenarios simulate pump driven (non pulsatile) flow under hemodilution and temperatures of 28°C and 37°C, respectively. The post CPB scenario simulates heart driven flow with moderate hypotension and hemodilution.

Table 5.2: Parameter values for the simulated CPB scenarios. Normothermic and hypothermic scenarios are motivated by [18]. CPB scenarios are motivated by [1].

	base- line	normo- thermia	hypo- thermia	pre- CPB	CPB-hypo- thermic	CPB-re- warming	post- CPB	units
MAP	100	120	120	75	50	50	75	mmHg
P_c	20	20	20	20	0	0	20	mmHg
Hct	45	45	45	45	25	25	25	%
T	37	37	28	37	28	37	37	°C
P_{O_2}	100	100	100	100	400	400	100	mmHg

Table 5.3: Comparison of normothermic and hypothermic scenarios. Values refer to a single nephron. Notation: Q_{AA} blood flow, Q_F SNGFR, FF filtration fraction, P_D glomerular capillary hydrostatic pressure, P_F Bowman’s space hydrostatic pressure, Q_{TAL} flow rate along the thick ascending limb, FPR fractional proximal water reabsorption, J^{total} net NaCl reabsorption.

	normothermia	hypothermia	units
Q_{AA}	285.2	149.8	nl/min
Q_F	29.2	15.1	nl/min
FF	18.9	18.6	%
P_D	50.3	44.3	mmHg
P_F	13.7	13.1	mmHg
Q_{TAL}	8.4	4.3	nl/min
FPR	71.3	71.5	%
J^{total}	3001	1532	pmol/min

5.3.1 Model validation

Model predictions for the normothermic and hypothermic scenarios are summarized on Table 5.3. A comparison of the predicted relative differences between the two scenarios reveals good agreement with the corresponding differences reported in [18], see Table 5.4.

5.3.2 Assessment durring CPB

Table 5.5 shows a summary of predicted values for the baseline and the simulated CPB scenarios. During the hypothermic and rewarming phases of CPB, blood flow and SNGFR are dramatically reduced relative to baseline. The effect of these reduc-

Table 5.4: Comparison of model predictions with experimental data. Notation: Q_{AA} blood flow, Q_F SNGFR, P_D glomerular capillary hydrostatic pressure, P_F Bowman’s space hydrostatic pressure, Q_{TAL} flow rate along the thick ascending limb, J^{total} net NaCl reabsorption. Experimental values are taken from [18], periods 1 and 2. Percentages are evaluated as the relative change between the corresponding normothermic and hypothermic values.

	simulated (%)	experimental (%)
Q_{AA}	-47.5	-44.5
Q_F	-48.2	-49.1
P_D	-11.9	-18.2
P_F	-4.3	-2.5
Q_{TAL}	-48.5	-49.3
J^{total}	-49.2	-49.3

Table 5.5: Summary of renal function during CPB. Values refer to a single nephron. Notation: Q_{AA} blood flow, Q_F SNGFR, FF filtration fraction.

	base-line	pre-CPB	CPB-hypothermic	CPB-re-warming	post-CPB	units
Q_{AA}	280.5	251.4	134.2	180.9	420.7	nl/min
Q_F	29.8	28.0	11.7	17.1	30.9	nl/min
FF	19.6	21.1	11.6	12.6	10.1	%
J^{total}	3196	3172	1303	1958	3441	pmol/min
J_{act}^{total}	3529	3593	2527	2710	3798	pmol/min
$J_{medulla}$	264	292	92	341	282	pmol/min
$J_{act}^{medulla}$	287	295	124	300	293	pmol/min

tions on renal oxygenation is further investigated below.

Figure 5.3 shows the rates of net and active NaCl reabsorption. Whole kidney reabsorption is reduced during the hypothermic and rewarming CPB phases. The low perfusion pressure in these phases causes vasoconstriction in the afferent arteriole, thereby lowering SNGFR. As a result of glomerulotubular balance, proximal tubule reabsorption, as well as overall NaCl reabsorption, are reduced accordingly.

In contrast, medullary reabsorption is reduced only during the hypothermic phase, whereas it appears slightly increased relative to baseline at the rewarming phase. The former is a consequence of the reduction of reabsorption along the TAL

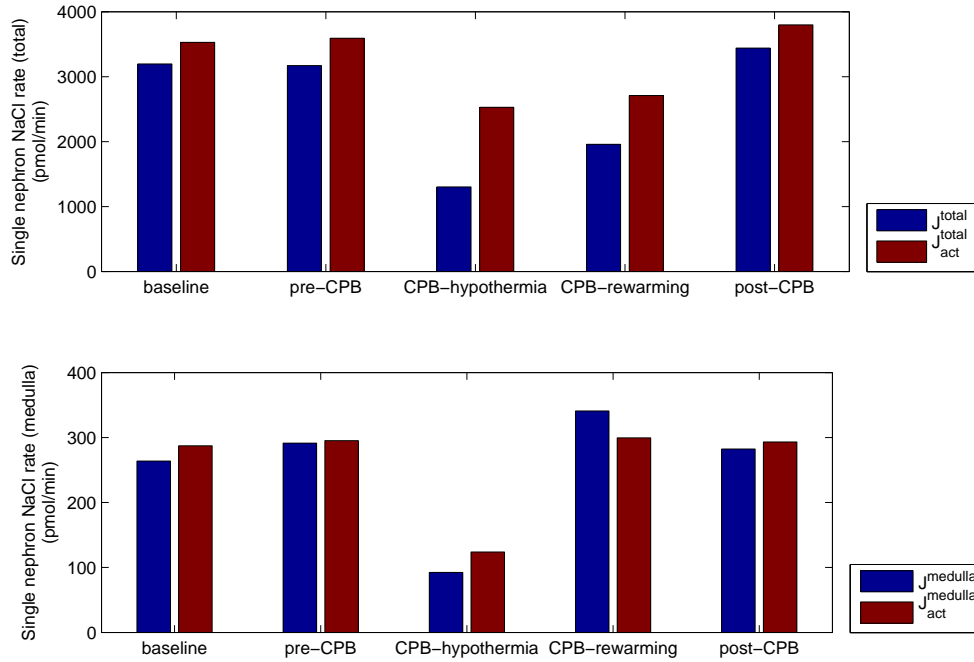


FIGURE 5.3: Rates of NaCl reabsorption during CPB. Rates refer to a single nephron. J and J_{act} denote net and active reabsorption.

induced by cooling.

Figure 5.4 illustrates the oxygen delivery and consumption rates for the simulated CPB scenarios. As is expected, the low NaCl reabsorption rate during the hypothermic and rewarming CPB phases leads to reduced oxygen consumption. However, hemodilution combined with the predicted reduction of blood flow (Table 5.5) results in a dramatic reduction in oxygen delivery rate, which exceeds the reduction in oxygen consumption. As a result, medullary oxygen availability during the hypothermic and rewarming CPB phases is predicted to fall nearly 5 times below the baseline level.

Fractional oxygen extraction for the whole kidney and the medulla is summarized in Figure 5.5. The model predicts that whole kidney oxygen fractional extraction achieves its maximum during the hypothermic phase, whereas medullary fractional

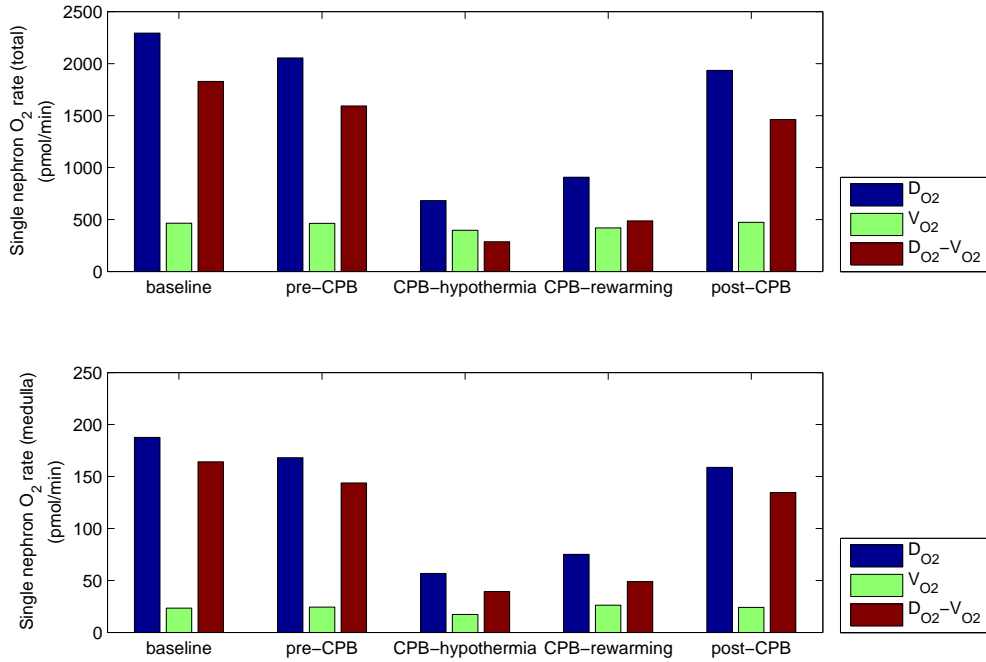


FIGURE 5.4: Oxygen delivery and oxygen consumption rates during the simulated CPB periods. Rates have been scaled down to the single nephron level. Corresponding quantities for the whole kidney can be retrieved by multiplying with N .

extraction achieves its maximum during the rewarming phase. In large part because of the low medullary oxygen consumption during the hypothermic phase.

5.3.3 CPB oxygenation sensitivity studies

The model have been used to estimate the effects and relative contributions of the factors affecting oxygenation during CPB. Namely, total and medullary fractional oxygen extraction have been estimated by varying MAP, hematocrit, and temperature. For all simulations P_{O_2} is set at 400 mmHg and blood flow is assumed to be non pulsatile. Results are shown on Figure 5.6. The reference state is set at MAP of 50 mmHg, hematocrit of 25%, and temperature of 37°C. Simulations with the reference state at a temperature of 28°C give qualitatively similar results (not shown).

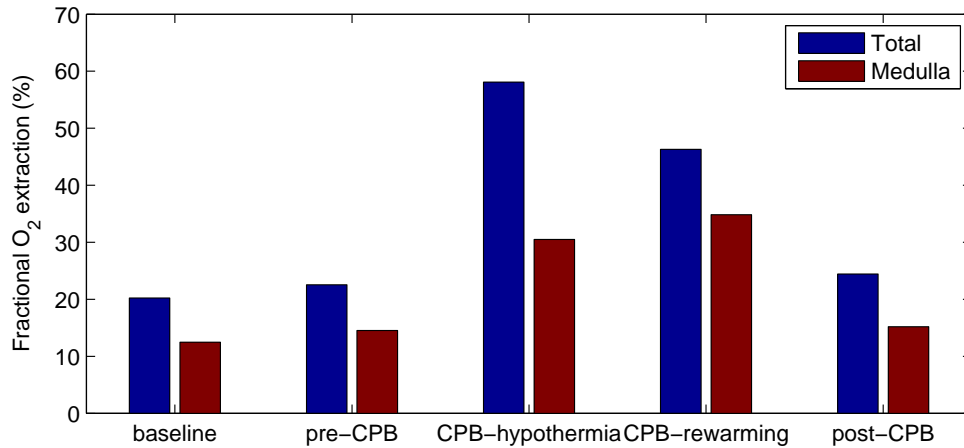


FIGURE 5.5: Renal oxygenation during CPB. Model predicts significantly reduced whole kidney oxygenation during both the hypothermic and rewarming phases of CPB. Medullary oxygenation is reduced only during the rewarming phase.

In all cases, fractional oxygen extraction increases with reduced MAP, hematocrit, and temperature, at least for the values obtained during CPB. The only apparent mismatch is the medullary oxygenation which slightly increases with temperatures that are above 26°C, Fig. 5.6C. This reflects the strong influence of cooling on reducing TAL active reabsorption, which in turn reduces medullary oxygen consumption.

Simulation results suggest that hypotension has the most prominent effect on oxygenation. Both total and medullary fractional extraction increase to 100% at sufficiently low MAP. This can be explained by two factors. First, low MAP nearly stops renal blood flow. As a consequence, oxygen supply is reduced nearly to zero. Second, oxygen consumption does not reduce below the basal level.

A similar behavior is observed also at low hematocrit values. In this case, oxygen supply is reduced due to the apparent reduction of erythrocyte flow. However, the oxygen dissolved in plasma is sufficient to balance oxygen consumption, at least up to a degree, so fractional extraction stays below 100%.

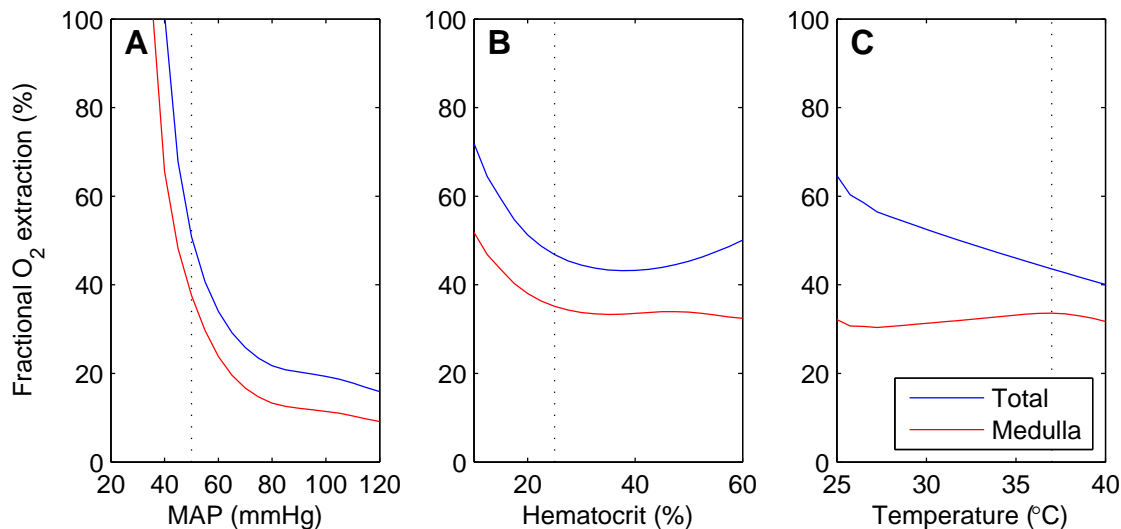


FIGURE 5.6: Renal oxygenation sensitivity during normothermic CPB. For all simulations it is assumed $P_{O_2} = 400$ mmHg and no pulsation. Reference state is at MAP of 50 mmHg, hematocrit of 25%, and temperature 37°C (denoted by dotted lines).

5.4 Discussion

5.4.1 Development of hypoxia

As can be seen from the results on Fig. 5.5, the simulated CPB predicts the development of conditions that favor renal hypoxia. From the total oxygen fractional extraction shown on Fig. 5.5, it may appear that the kidney is endangered mostly during the hypothermic phase. However, a closer examination indicates that the biggest threat occurs during rewarming, where medullary oxygenation is at its minimum.

During CPB surgery, control over perfusion pressure is limited. Results shown on Fig. 5.6 indicate that a perfusion pressure close or below 40 mmHg leads to dramatic increase in oxygen extraction, for both the whole kidney and the medulla. Thus, poor control of renal perfusion pressure during CPB has the potential of significantly increasing the risk of hypoxia.

5.4.2 Model limitations

The incorporation of the temperature effects on vascular tone of the arterioles is phenomenological. Nonetheless, the model predicts hemodynamics that are in good agreement with the available observations Ref. [18], Table 5.4.

The model of the nephron used in this study represents the minimum tubular processes necessary for the closure of the TGF loop. Water and NaCl transport downstream of the site of macula densa are not represented. Oxygen consumption associated with NaCl reabsorption by the distal nephron and collecting duct system is included in the basal consumption, which is assumed independent of the rest of NaCl reabsorption and temperature.

The nephrovascular model represents a short loop nephron. Therefore, medullary NaCl reabsorption as well as medullary blood flow concern only the outer medulla and no prediction for the inner medulla is made.

Conclusions and future directions

6.1 Conclusions

The work presented in this dissertation focuses mainly on the development and the mathematical analysis of a model of renal hemodynamics in which both autoregulatory mechanisms, i.e. myogenic response and tubuloglomerular feedback, are represented [27, 145, 147, 146]. The developed model is the only currently available dynamic model that represents renal autoregulation by combining both mechanisms. Other proposed models are time-independent [120], incorporate only the myogenic response [105] or only tubuloglomerular feedback [115]. Therefore, their applicability in clinical scenarios is limited.

Under baseline conditions the model predicts two interacting oscillations. Afferent arteriolar smooth muscle membrane potential fluctuates spontaneously due to periodic calcium and potassium fluxes, resulting in the faster of the observed oscillations (Chapters 1–4). The time between an increase in distal nephron salt and its subsequent reduction due to tubuloglomerular feedback gives rise to the slower oscillations (Chapter 4).

Increased or reduced systemic arterial pressure, due to activation of the autoregulatory mechanisms, leads to compensatory adjustments of afferent arteriole diameter that keep time average blood flow nearly constant (Chapters 3–4). In contrast, complete or partial inhibition of the autoregulatory mechanisms fails to predict or drastically limits such adjustments. As a consequence, autoregulation is missing (Chapter 4).

Due to its ability to regulate downstream pressure, the model is successful in capturing the asymmetry in the propagation direction of the vasomotor responses that is seen experimentally [154] to decay faster in the downstream than in the upstream direction (Chapter 3). Such asymmetric propagation is speculated to influence kidney activity in the organ level. Its exact role remains to be elucidated by further studies.

6.2 Future directions

The model developed in this thesis can be utilized as the basis for the development of a computational model of renal hemodynamics in the organ level. The resulting model, that will fill the apparent gap of dynamical renal models, will provide an integrated model of renal autoregulation that can be combined with systemic models, e.g. [64], to study long and short term organ behavior. The resulting model can be also utilized to model the underlying pathophysiology causing renal damage that is clinically and experimentally inaccessible [107]. Cases of particular importance include hypertension and diabetes, as they are the most common causes of end-stage renal disease. An analysis of the contributions of the autoregulatory mechanisms and the interactions developed among them under these conditions can elucidate the progression stages with a potential impact on treatment and prevention.

Such an extension requires the following steps: (i) construction of a nephrovascular network, (ii) representation of modulating effects, and (iii) detailed representation

of vascular blood flow. These steps are briefly analyzed in the next sections.

6.2.1 Construction of nephrovascular network

The current model represents phenomena within a single nephron and the attached afferent arteriole. There is evidence of phenomena taking place within larger regions that include the coordinated operation of multiple nephrons fed by the same interlobular artery, as well as, to an even larger extent, phenomena arising by the coordination of such regions that may influence hemodynamics at the organ level [69, 76].

The proposed nephrovascular model can be extended by combining several instances into a network of realistic size and architecture [127]. With such a model, the investigation of the role of the aforementioned interactions in enhancing or blunting renal autoregulation at the organ level, and the determination of the extent to which the asymmetry of vasomotor responses affects network behavior can be elucidated.

6.2.2 Representation of modulating effects

A majority of phenomena operating in slow time scales modulate renal autoregulation and play a prominent role in kidney and whole body physiology [37, 82]. The proposed model can be extended to such time scales with the inclusion of at least the renin-angiotensin system, which is a hormone system capable of exercising powerful influence on systemic pressure and renal autoregulation [86]. Such an extension demands the appropriate representation of systemic and intrarenal inputs such as angiotensinogen and renin levels secreted by liver and juxtaglomerular cells, etc.

6.2.3 Detailed representation of vascular blood flow

Nitric oxide (NO) is a plasma substance with known vasorelaxant effects [37, 82]. In the renal circulation, NO is secreted by the endothelium in response to increased shear stress. It is then carried downstream by the bloodstream where it acts upon

the surrounding smooth muscles by reducing the vascular tone, causing dilation and partial inhibition of the myogenic response.

For the incorporation of these effects to the afferent arteriole component of the proposed model, it is needed the replacement of the Poiseuille flow, that is currently utilized, with a representation provided by the Navier-Stokes equations that accounts for the accurate evaluation of shear stress and transport along the vascular lumen. The vasorelaxant effect of NO, as well as the activation of the myogenic response, under this set up, results in a fluid-structure interaction problem. Such problems are commonly difficult and challenging to compute.

For the numerical solution of the model equations that concern blood flow, an extended version of the immersed interface method developed for the incompressible axis-symmetric Navier-Stokes in [98] could be adopted. Such extension needs to consider the case of interfaces separating fluids of different viscosity. In the specific case of the renal afferent arteriole, the interface will represent the vascular walls, while the separating fluids will represent blood and interstitial fluid. The forces driving the interface movement will be provided by the mechanical stresses developed across the vascular wall, which in turn depend on local transmural pressure and muscle activation.

Appendix A

Complete set of smooth muscle model equations

In this chapter, is presented the complete set of model equations concerning the single vascular smooth muscle (VSM) representation. In the combined nephrovascular model (see next chapter) are contained a total of N_{AA} VSM, that are linearly arranged between $i = 1$ (VSM proximate to the cortical radial artery) and $i = N_{AA}$ (VSM proximate to the glomerulus). The axial center of each VSM is located at:

$$z_m^i = \left(i - \frac{1}{2}\right)h_m$$

where $h_m = L_{AA}/N_{AA}$ is the axial length occupied by each VSM, and L_{AA} is the total AA length.

A.1 Electrophysiology

Muscle and associated endothelial compartment membrane potentials are given by:

$$C_m \frac{dv_m^i}{dt} = -I_L^i - I_K^i - I_{Ca}^i - I_{m-e}^i + I_{m-m}^i + I_{TGF}^i + I_{MR}^i$$
$$C_e \frac{dv_e^i}{dt} = I_{m-e}^i + I_{e-e}^i$$

For simplicity, the above equation are cast into the normalized forms:

$$\begin{aligned}\frac{dv_m^i}{dt} &= -\tilde{I}_L^i - \tilde{I}_K^i - \tilde{I}_{Ca}^i - \tilde{I}_{m-e}^i + \tilde{I}_{m-m}^i + \tilde{I}_{TGF}^i + \tilde{I}_{MR}^i \\ \frac{dv_e^i}{dt} &= C_{m-e} \left(\tilde{I}_{m-e}^i + \tilde{I}_{e-e}^i \right)\end{aligned}$$

where $C_{m-e} = C_m/C_e$. Ion currents:

$$\begin{aligned}\tilde{I}_L^i &= \tilde{g}_L(v_m^i - v_L) \\ \tilde{I}_K^i &= \tilde{g}_K n_g^i (v_m^i - v_K) \\ \tilde{I}_{Ca}^i &= \tilde{g}_{Ca} m_g^i (v_m^i - v_{Ca})\end{aligned}$$

Electrical communication:

$$\begin{aligned}\tilde{I}_{m-e}^i &= \tilde{g}_{m-e} (v_m^i - v_e^i) \\ \tilde{I}_{m-m}^i &= \tilde{g}_{m-m} (v_m^{i-1} - 2v_m^i + v_m^{i+1}) \\ \tilde{I}_{e-e}^i &= \tilde{g}_{e-e} (v_e^{i-1} - 2v_e^i + v_e^{i+1})\end{aligned}$$

For the smooth muscle-to-smooth muscle and endothelium-to-endothelium currents are used leaky boundary conditions, which are implemented through the ghost values:

$$\begin{aligned}v_m^0 &= v_m^1 + \frac{v_m^1 - v_m^2}{N_{AA}}, & v_m^{N_{AA}+1} &= v_m^{N_{AA}} + \frac{v_m^{N_{AA}} - v_m^{N_{AA}-1}}{N_{AA}} \\ v_e^0 &= v_e^1 + \frac{v_e^1 - v_e^2}{N_{AA}}, & v_e^{N_{AA}+1} &= v_e^{N_{AA}} + \frac{v_e^{N_{AA}} - v_e^{N_{AA}-1}}{N_{AA}}\end{aligned}$$

Calcium and potassium ion channel gating and equilibrium gating:

$$\begin{aligned}\frac{dn_g^i}{dt} &= \phi_n (n_{g,\infty}^i - n_g^i) \cosh \frac{v_m^i - v_{m,3}^i}{2v_{m,4}} \\ m_g^i &= m_{g,\infty}^i \\ m_\infty^i &= \frac{1}{2} \left(1 + \tanh \frac{v_m^i - v_{m,1}^i}{v_{m,2}} \right) \\ n_\infty^i &= \frac{1}{2} \left(1 + \tanh \frac{v_m^i - v_{m,3}^i}{v_{m,4}} \right)\end{aligned}$$

The dependence of n_g^i upon c^i (see below) is captured by setting:

$$v_{m,3}^i = v_{m,6} - \frac{v_{m,5}}{2} \tanh\left(\frac{c^i - c_3}{c_4}\right)$$

A.2 Autoregulatory mechanisms

A.2.1 Myogenic response

The electrical current mediating the myogenic response depends on local blood pressure $P_{AA}^i = P_{AA}(z_m^i)$ (see next chapter) according to the delay differential equation:

$$\frac{d\tilde{I}_{MR}^i}{dt} = \begin{cases} k_{inc} \left(\tilde{I}_{MR}^\infty(P_{MR}^i(t - \tau_m)) - \tilde{I}_{MR}^i \right), & \text{triggered by pressure rise} \\ k_{dec} \left(\tilde{I}_{MR}^\infty(P_{MR}^i(t - \tau_m)) - \tilde{I}_{MR}^i \right), & \text{triggered by pressure drop} \end{cases}$$

The pressure activating the myogenic response and the associated reference are:

$$P_{MR}^i(t - \tau_m) = P_{AA}^i(t - \tau_m) - P_{AA,ref}^i$$

$$P_{AA,ref}^i = \left(1 - \frac{1 + 2i}{2N_{AA}}\right)(P_0^{ref} + \Delta P_0^{ref}) + \frac{(1 + 2i)}{2N_{AA}} \left(P_D^{ref} + \frac{P_D^{ref}}{P_0^{ref}} \Delta P_0^{ref}\right)$$

The target current \tilde{I}_{MR}^∞ is given by a simple sigmoidal curve:

$$\tilde{I}_{MR}^\infty(p) = \tilde{I}_{MR}^{min} + \frac{\tilde{I}_{MR}^{max} - \tilde{I}_{MR}^{min}}{1 - b_{MR}(p)}$$

$$b_{MR}(p) = \frac{\tilde{I}_{MR}^{max}}{\tilde{I}_{MR}^{min}} \exp\left(\frac{\tilde{I}_{MR}^{max} - \tilde{I}_{MR}^{min}}{\tilde{I}_{MR}^{min} \tilde{I}_{MR}^{max}} s_{MR} p\right)$$

A.2.2 Tubuloglomerular feedback

The electrical current mediating the tubuloglomerular feedback depends on macula densa luminal Cl^- concentration $C_{MD} = C_{TB}(L_{TB})$ (see next chapter) according to:

$$\tilde{I}_{TGF}^i = \begin{cases} 0, & i < N_{AA} - N_{AA}^{TGF} \\ \tilde{I}_{TGF}^\infty, & i \geq N_{AA} - N_{AA}^{TGF} \end{cases}$$

The target current \tilde{I}_{TGF}^∞ is given by a simple sigmoidal curve:

$$\tilde{I}_{TGF}^\infty = \tilde{I}_{TGF}^{min} + \frac{\tilde{I}_{TGF}^{max} - \tilde{I}_{TGF}^{min}}{1 - b_{TGF}}$$

$$b_{TGF} = \frac{\tilde{I}_{TGF}^{max}}{\tilde{I}_{TGF}^{min}} \exp\left(\frac{\tilde{I}_{TGF}^{max} - \tilde{I}_{TGF}^{min}}{\tilde{I}_{TGF}^{min} \tilde{I}_{TGF}^{max}} s_{TGF} (C_{MD} - C_{MD}^\infty)\right)$$

A.3 Cytosolic Ca^{2+} regulation

Cytosolic free Ca^{2+} concentration is evaluated assuming the reaction with the buffer is at equilibrium:

$$\frac{dc^i}{dt} = \frac{(K_d + c^i)^2}{(K_d + c^i)^2 + K_d B_T} \left(-\tilde{\alpha}_{Ca} \tilde{I}_{Ca}^i - k_{Ca} c^i \right)$$

A.4 Cross-bridge cycling

The formation of crossbridges and the phosphorylation of myosin light chain are governed by:

$$\frac{dw_f^i}{dt} = k_\psi \left(\frac{\psi^i}{\psi_m + \psi^i} - w_f^i \right)$$

$$\psi^i = \frac{(c^i)^3}{(c_m)^3 + (c^i)^3}$$

A.5 Muscle mechanics

Muscle luminal radius is obtained by the balance of tensions developed across the muscle's cross-section:

$$\tau_c \frac{dR_{AA}^i}{dt} = T_P(R_{AA}^i, P_{AA}^i) - T_{wall}(\xi_{AA}^i, w_f^i, R_{AA}^i/R_{AA}^c)$$

Interval viscosity is set at $\tau_c = R_{AA}^c (P_c^{ref} - P_{ext})$. The developed tensions depend on local blood pressure P_{AA}^i , formed crossbridges w_f^i (i.e. muscle activation), and muscle

length (which is proportional to R_{AA}^i):

$$T_P(r, p) = (p - P_{ext})r$$

$$T_{wall}(\xi, w, r) = \xi \left(T_{pass}(r) + wT_{act}(r) \right)$$

$$T_{pass}(r) = C_{pass} \exp \left(C_{pass}^P (r - 1) \right) - \left(\frac{C_{pass}^{PP}}{r} \right)^2$$

$$T_{act}(r) = C_{act} \exp \left(- \left(\frac{r - C_{act}^P}{C_{act}^{PP}} \right)^2 \right)$$

The scaling ξ_{AA}^i is assumed to decrease linearly along the vascular axis:

$$\xi_{AA}^i = \frac{(P_D^{ref} - P_0^{ref})(i + 1/2) + (P_0^{ref} - P_{ext})N_{AA}}{(P_c^{ref} - P_{ext})N_{AA}}$$

and the reference is set at $P_c^{ref} = (P_0^{ref} + P_D^{ref})/2$.

A.6 Glossary and parameter values

In the following sections, time and space dependence is denoted explicitly. In contrast, dependence only on parameters is not denoted.

A.6.1 Variables

t , time • i , index indicating VSM position in AA • z_m^i , VSM axial location • h_m , VSM axial length • $v_m^i(t)$, VSM membrane potential • $v_e^i(t)$, endothelium compartment membrane potential • $I_L^i(t)$, leak membrane current • $I_K^i(t)$, potassium membrane current • $I_{Ca}^i(t)$, calcium membrane current • $I_{m-e}^i(t)$, smooth muscle-to-endothelium current • $I_{m-m}^i(t)$, smooth muscle-to-smooth muscle current • $I_{e-e}^i(t)$, endothelium-to-endothelium current • $I_{MR}^i(t)$, MR mediating current • $I_{TGF}^i(t)$, TGF mediating current • $\tilde{I}_L^i(t)$, normalized leak membrane current • $\tilde{I}_K^i(t)$, normalized potassium membrane current • $\tilde{I}_{Ca}^i(t)$, normalized calcium membrane current • $\tilde{I}_{m-e}^i(t)$, normalized smooth muscle-to-endothelium current • $\tilde{I}_{m-m}^i(t)$, normalized

smooth muscle-to-smooth muscle current • $\tilde{I}_{e-e}^i(t)$, normalized endothelium-to-endothelium current • $\tilde{I}_{MR}^i(t)$, normalized MR mediating current • $\tilde{I}_{TGF}^i(t)$, normalized TGF mediating current • $\tilde{I}_{MR}^\infty(t)$, normalized target MR current • $\tilde{I}_{TGF}^\infty(t)$, normalized target TGF current • $n_g^i(t)$, potassium channels gating • $m_g^i(t)$, calcium channels gating • $n_{g,\infty}^i(t)$, potassium channels equilibrium gating • $m_{g,\infty}^i(t)$, calcium channels equilibrium gating • $v_m^0(t)$ and $v_e^0(t)$, left ghosts • $v_m^{N_{AA}+1}(t)$ and $v_e^{N_{AA}+1}(t)$, right ghosts • $v_{m,3}^i(t)$, potassium channels gating sensitivity • $c^i(t)$, free cytosolic Ca^{2+} concentration • $P_{AA}^i(t)$, VSM blood pressure • $P_{AA}(t, z)$, blood pressure profile (see next chapter) • $P_{MR}^i(t)$, VSM pressure activating MR • $P_{AA,ref}^i$, reference pressure for MR activation • $b_{MR}(t)$, auxiliary MR activation function • $b_{TGF}(t)$, auxiliary TGF activation function • $C_{MD}(t)$, luminal macula densa Cl^- concentration (see next chapter) • $C_{TB}(t, x)$, TB Cl^- concentration profile (see next chapter) • L_{TB} , TB length (see next chapter) • $w_f^i(t)$, fraction of formed to total available crossbridges • $\psi^i(t)$, myosin light chain phosphorylation • $R_{AA}^i(t)$, VSM luminal radius • $T_P(\cdot)$, Laplace tension • $T_{wall}(\cdot)$, wall tension • $T_{pass}(\cdot)$, passive component of wall tension • $T_{act}(\cdot)$, active component of wall tension • ξ_{AA}^i , wall tension scaling • P_c^{ref} , reference Laplace pressure • τ_c , VSM internal viscosity.

A.6.2 Parameters

$N_{AA} = 101$, total number of VSM in AA • $N_{AA}^{TGF} = 20$, number of VSM directly affected by TGF • $L_{AA} = 303 \mu\text{m}$, total AA length (see next chapter) • $C_m = 6.5 \text{ pF}$, VSM membrane capacitance • $C_{m-e} = 16$, VSM to endothelium membrane capacitances ratio • $\tilde{g}_{m-e} = 85 \text{ Hz}$, smooth muscle-to-endothelium normalized conductance • $\tilde{g}_{m-m} = 950 \text{ Hz}$, smooth muscle-to-smooth muscle normalized conductance • $\tilde{g}_{e-e} = 2\tilde{g}_{m-m}$, endothelium-to-endothelium normalized conductance • $\tilde{g}_L = 1 \text{ Hz}$, leak current normalized conductance • $\tilde{g}_K = 4 \text{ Hz}$, potassium current normalized conductance • $\tilde{g}_{Ca} = 2 \text{ Hz}$, calcium current normalized conductance • $v_L = -70 \text{ mV}$,

leak current reversal potential • $v_K = -95$ mV, potassium current reversal potential • $v_{Ca} = 80$ mV, calcium current reversal potential • $\phi_n = 0.925$ Hz, potassium channels opening rate • $v_{m,1} = -22.5$ mV, calcium channels gating sensitivity • $v_{m,2} = 25$ mV, calcium channels gating sensitivity • $v_{m,4} = 14.5$ mV, potassium channels gating sensitivity • $v_{m,5} = 8$ mV, potassium channels gating sensitivity • $v_{m,6} = -15$ mV, potassium channels gating sensitivity • $c_3 = 400$ nM, potassium channels gating sensitivity • $c_4 = 150$ nM, potassium channels gating sensitivity • $k_{inc} = 0.550$ Hz, MR activation rate constant for pressure increase • $k_{dec} = 0.125$ Hz, MR activation rate constant for pressure decrease • $\tau_m = 0.3$ or 1.0 s, MR activation delay • $P_0^{ref} = 95$ mmHg, reference AA inflow pressure (see next chapter) • $P_D^{ref} = 50$ mmHg, reference AA outflow pressure (see next chapter) • $\Delta P_0^{ref} = 11$ mmHg, pulse amplitude MR activation correction (see next chapter) • $\tilde{I}_{MR}^{min} = -4.872$ mV/s, normalized minimum MR target current • $\tilde{I}_{MR}^{max} = 30.049$ mV/s, normalized maximum MR target current • $\tilde{I}_{TGF}^{min} = -12.327$ mV/s, normalized minimum TGF target current • $\tilde{I}_{TGF}^{max} = 9.215$ mV/s, normalized maximum TGF target current • $s_{MR} = 0.245$ mmHg⁻¹, MR activation sensitivity • $s_{TGF} = 0.847$ mM⁻¹, TGF activation sensitivity • $C_{MD}^\infty = 32$ mM, reference luminal macula densa Cl⁻ concentration (i.e. TGF target value) • $K_d = 10^3$ nM, free cytosolic Ca²⁺ regulation • $B_T = 10^5$ nM, free cytosolic Ca²⁺ regulation • $\tilde{\alpha}_{Ca} = 628$ mV⁻¹, calcium current to mass conversion • $k_{Ca} = 190$ Hz, cytosolic Ca²⁺ extrusion rate • $k_\psi = 0.318$ Hz, crossbridges cycling rate • $\psi_m = 0.55$, crossbridges cycling sensitivity • $c_m = 400$ nM, myosin light chain phosphorylation sensitivity • $R_{AA}^c = 13$ μ m, reference AA radius • $P_{ext} = 5$ mmHg, interstitial hydrostatic pressure • $C_{act} = 3970$ μ m·mmHg, active wall stress • $C_{act}^P = 1$, active wall stress • $C_{act}^{PP} = 0.535$, active wall stress • $C_{pass} = 1822$ μ m·mmHg, passive wall stress • $C_{pass}^P = 9.759$, passive wall stress • $C_{pass}^{PP} = 1$, passive wall stress.

Appendix B

Complete set of nephrovascular model equations

In this chapter, are listed the model equations used in the formulation of the latest version (i.e. Chapter 5) of the combined nephrovascular model. A simplified representation of the model's components and the interactions developed among them is shown on Fig. B.1.

B.1 Vasculature

The model vasculature consists of three segments: pre-AA, AA, and post-AA. In particular, the post-AA segment is comprised by GL and EA. For all simulations, systemic arterial pressure is prescribed:

$$P_{RA}(t) = P_m + P_p \sin(2\pi f_p t)$$

where P_m is mean arterial pressure, P_p is the pulse amplitude that reaches the AA entrance, and f_p is the heart rate.

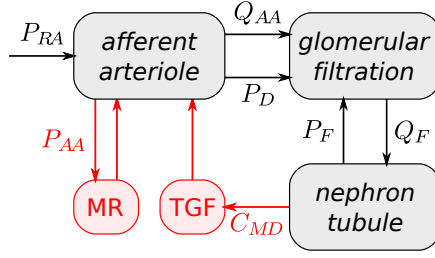


FIGURE B.1: Simplified representation of the model’s components and the developed interactions. The autoregulatory mechanisms are marked in red. For the notation used, see the main text.

B.1.1 Blood flow

Blood flow along the model vasculature is computed by total arterial-to-venous pressure drop and vascular resistance. Assuming quasi-steady Poiseuille flow of uniform volumetric rate, this is equivalent to:

$$Q_{AA} = \frac{P_D - P_{EA,end}}{\Omega_{EA}} + Q_F$$

where Q_F accounts for the lost of plasma ultrafiltrate in the GL (see below). The resistance of the post-AA segment is given by:

$$\Omega_{EA} = \Omega_{EA}^{ref} \left(\frac{R_{EA}^{ref}}{R_{EA}} \right)^4$$

where R_{EA} is EA luminal radius (see below). Note that because of GL resistance being significantly lower than the resistance of any of the other vascular segments, it is assumed $\Omega_{GL} = 0$.

B.1.2 Afferent arteriole

The model AA extents from $z = 0$ (i.e. connection with cortical radial artery) to $z = L_{AA}$ (i.e. connection with GL capillaries). Pressure profile along the AA is computed by the Poiseuille equation:

$$\frac{\partial P_{AA}}{\partial z} = -\frac{8\mu_{AA}}{\pi R_{AA}^4} Q_{AA}$$

The boundary condition is provided by AA inflow pressure $P_{AA}(0) = P_0$, where:

$$P_0 = P_{RA} - Q_{AA}\Omega_{RA}$$

For completeness, it is also noted that AA outflow pressure is $P_D = P_{AA}(L_{AA})$. To avoid the difficulties arising from the estimation of blood's viscosity, the above equation is cast into the equivalent form:

$$\frac{\partial P_{AA}}{\partial z} = -\Omega_{AA}^{ref} \left(\frac{R_{AA}^{ref}}{R_{AA}} \right)^4 Q_{AA}$$

The radius profile is determined by the luminal radii of each individual VSM (see previous chapter) R_{AA}^i , in a piecewise manner, as follows:

$$R_{AA} = \begin{cases} R_{AA}^1, & 0 \leq z \leq z_m^1 + \frac{h_m}{2} \\ R_{AA}^i, & z_m^i - \frac{h_m}{2} < z \leq z_m^i + \frac{h_m}{2} \\ R_{AA}^{N_{AA}}, & z_m^{N_{AA}} - \frac{h_m}{2} < z \leq L_{AA} \end{cases}$$

B.1.3 Efferent arteriole

Luminal radius along the EA is assumed uniform and is computed similarly to the AA one:

$$\tau_c \frac{dR_{EA}}{dt} = T_P(R_{EA}, P_{EA}) - T_{wall}(\xi_{EA}, w_f^{EA}, R_{EA}/R_{EA}^c)$$

$$P_{EA} = \frac{P_D + P_{EA,end}}{2}$$

$$\xi_{EA} = \frac{P_{EA}^{ref} - P_{ext}}{P_c^{ref} - P_{ext}}$$

where, in contrast to AA, the muscle activation of the smooth muscles (i.e. w_f^{EA}) is kept constant. The tensions T_P and T_{wall} are the same as in AA (see previous chapter). The reference pressure is set at $(P_D^{ref} + P_{EA,end})/2$.

B.1.4 Structural resistances and hematocrit dependence

The reference resistances of the vascular segments are given by:

$$\Omega_{RA} = \frac{P_{RA}^{ref} - P_0^{ref}}{Q_{AA}^{ref}} \frac{\mu_{RA}}{\mu_{RA}^{ref}}$$

$$\Omega_{AA}^{ref} = \frac{P_0^{ref} - P_D^{ref}}{Q_{AA}^{ref}} \frac{\mu_{AA}}{\mu_{AA}^{ref}}$$

$$\Omega_{EA}^{ref} = \frac{P_D^{ref} - P_{EA,end}}{Q_{EA}^{ref}} \frac{\mu_{EA}}{\mu_{EA}^{ref}}$$

and $Q_{EA}^{ref} = Q_{AA}^{ref} - Q_F^{ref}$. Apparent blood viscosity dependence on the hematocrit value is given by:

$$\frac{\mu_{RA}}{\mu_{RA}^{ref}} = \frac{1.07}{(1 - Ht_{RA})^{0.80}} - 0.73$$

$$\frac{\mu_{AA}}{\mu_{AA}^{ref}} = \frac{0.77}{(1 - Ht_{AA})^{1.02}} - 0.43$$

$$\frac{\mu_{EA}}{\mu_{EA}^{ref}} = \frac{0.67}{(1 - Ht_{EA})^{1.02}} - 0.37$$

Hematocrit values are given by:

$$Ht_{RA} = Ht$$

$$Ht_{AA} = Ht_{RA}$$

$$Ht_{EA} = Ht_{AA} \frac{Q_{AA}}{Q_{AA} - Q_F}$$

where Ht denotes the systemic hematocrit.

B.2 Glomerulus

The model GL, idealized as a single capillary, extends from $y = 0$ (i.e. connection with AA) to $y = L_{GL}$ (i.e. connection with EA). Blood pressure and plasma flow at

the GL entrance are given by:

$$\begin{aligned}\tau_{gl} \frac{dP_{gl}}{dt} &= P_D - P_{gl} \\ \tau_{gl} \frac{dQ_{gl}}{dt} &= (1 - Ht_{AA})Q_{AA} - Q_{gl}\end{aligned}$$

Pressure and plasma flow profiles, along GL, are given by:

$$\begin{aligned}P_{GL} &= P_{gl} - \frac{y}{L_{GL}} \Delta P_{GL} \\ \frac{\partial Q_{GL}}{\partial y} &= -K_f (P_{GL} - P_F - \pi_{GL})\end{aligned}$$

For the latter, the boundary condition is $Q_{GL}(0) = Q_{gl}$. Hydrostatic pressure in the Bowman space is $P_F = P_{TB}(0)$ (see below). Total blood pressure drop, along GL, is:

$$\begin{aligned}\Delta P_{GL} &= \frac{\mu_{GL}}{\mu_{GL}^{ref}} \Delta P_{GL}^{ref} \\ \frac{\mu_{GL}}{\mu_{GL}^{ref}} &= \frac{0.88}{(1 - Ht_{GL})^{1.07}} - 0.67\end{aligned}$$

where $Ht_{GL} = Ht_{AA}$. Colloid osmotic pressure is given by protein concentration:

$$\pi_{GL} = a_{GL,1} C_{GL} + a_{GL,2} C_{GL}^2$$

In turn, protein concentration is given by:

$$C_{GL} = C_{gl} \frac{Q_{gl}}{Q_{GL}}$$

Single nephron glomerular filtration rate (SNGFR) is given by:

$$Q_F = \max\left(0, Q_{GL}(0) - Q_{GL}(L_{GL})\right)$$

B.3 Nephron tubule

The model TB extends from $x = 0$ (i.e. connection with Bowman space) to $x = L_{TB}$ (i.e. site of macula densa and connection with distal tubule). For the definition of

the parameter profiles, the following sites are used:

$$\begin{aligned} x_0 &= 0, & x_1 &= x_0 + L_{PCT}, & x_2 &= x_1 + L_{PST} \\ x_3 &= x_2 + L_{DL}, & x_4 &= x_3 + L_{TAL}, & x_w &= 0.4x_2 + 0.6x_3 \end{aligned}$$

For completeness, it is noted that $L_{TB} = L_{PCT} + L_{PST} + L_{DL} + L_{TAL}$. In the following, subscripts 0–4 and w are used to denote the associated values at the above x_0 – x_4 and x_w sites, respectively. Further, the following abbreviations have been used: • PT, proximal tubule; • LH, loop of Henle; • PCT, proximal convoluted tubule; • PST, proximal strait tubule; • DL, descending limb; • TAL, thick ascending limb. Finally, to simplify the expressions, the following smoothed step function is used:

$$\Lambda_{TB}(s_{par}, x_{par}) = \frac{1}{2} \left(1 + \tanh \left(s_{par} \frac{x - x_{par}}{L_{TAL}} \right) \right)$$

B.3.1 Tubular water transport

Tubular volumetric rate profile is given by conservation of water:

$$\frac{\partial Q_{TB}}{\partial x} = -2\pi R_{TB} \frac{\partial R_{TB}}{\partial t} - \Phi_{TB}$$

The boundary condition is $Q_{TB}(0) = Q_F$. Water efflux is determined by glomero-tubular balance and pressure natriuresis:

$$\Phi_{TB} = S_{GTB} S_{PN} \Phi_{TB}^{base}$$

The scaling profiles are given by:

$$S_{PN} = 1 - PN_{sc} \Lambda_{TB}(-30, x_2)$$

$$S_{GTB} = 1 + (GTB_{sc} - 1) \Lambda_{TB}(-30, x_3)$$

and the actual scalings by:

$$PN_{sc} = \min \left(0.5, s_{PN} \frac{\max(P_m, P_{PN, cut}) - P_{PN, base}}{P_{PN, base}} \right)$$

$$GTB_{sc} = \frac{1}{1 - \kappa_{GTB} (1 - Q_F^\infty / Q_F)}$$

The base water efflux profile is given by:

$$\begin{aligned}\Phi_{TB,base} = & (\Phi_{PCT} - \Phi_{PST})\Lambda_{TB}(-30, x_1) + \\ & + (\Phi_{PST} - \Phi_{DL})\Lambda_{TB}(-30, x_2) + \Phi_{DL}\Lambda_{TB}(-30, x_w)\end{aligned}$$

The reference values are:

$$\Phi_{PCT} = \frac{Q_0^{ref} - Q_1^{ref}}{x_1 - x_0}$$

$$\Phi_{PST} = \frac{Q_1^{ref} - Q_2^{ref}}{x_2 - x_1}$$

$$\Phi_{DL} = \frac{Q_2^{ref} - Q_w^{ref}}{x_w - x_2}$$

B.3.2 Tubular radius

Tubular radius profile depends passively on transmural pressure:

$$R_{TB} = \alpha_{TB}(P_{TB} - P_{ext}) + \beta_{TB}$$

The tubular compliance and unpressurized radius profiles are given by:

$$\alpha_{TB} = (\alpha_{PT} - \alpha_{LH})\Lambda_{TB}(-30, x_2) + \alpha_{LH}$$

$$\begin{aligned}\beta_{TB} = & \beta_2 + (\beta_3 - \beta_2)\Lambda_{TB}(35, 0.65x_2 + 0.35x_3) \\ & + (\beta_4 - \beta_3)\Lambda_{TB}(3.5, 0.65x_3 + 0.35x_4)\end{aligned}$$

B.3.3 Tubular pressure

Pressure profile is obtained by the Poiseuille equation:

$$\frac{\partial P_{TB}}{\partial x} = -\frac{8\mu_{TB}}{\pi R_{TB}^4} Q_{TB}$$

The boundary condition is provided by outflow pressure $P_{TB}(L_{TB}) = P_{MD}$, where:

$$P_{MD} = P_{DT,end} + Q_{MD}\Omega_{DT}$$

and $Q_{MD} = Q_{TB}(L_{TB})$. Distal tubule pressure and resistance are:

$$P_{DT} = \frac{P_{MD} + P_{DT,end}}{2}$$

$$\Omega_{DT} = \left(1 - \tanh\left(s_{DT}(P_{DT} - P_{DT}^{ref})\right)\right) \frac{P_{MD}^{ref} - P_{DT,end}}{Q_{MD}^{ref}}$$

and the reference pressure is set at: $P_{DT}^{ref} = (P_{MD}^{ref} + P_{DT,end})/2$.

B.3.4 Tubular Cl^- transport

Luminal Cl^- concentration profile is obtained by conservation of mass:

$$\frac{\partial}{\partial t}(\pi R_{TB}^2 C_{TB}) = -\frac{\partial}{\partial x}(Q_{TB} C_{TB}) - 2\pi R_{TB}^{ss} \left(\frac{V_{max} C_{TB}}{K_M + C_{TB}} + \kappa_{TB}(C_{TB} - C_{TB}^{ext}) \right)$$

The boundary condition is given by plasma Cl^- concentration $C_{TB}(0) = C_F$. Interstitial Cl^- concentration depends on the depth along the corticomedullary axis:

$$C_{TB}^{ext} = C_{LB}^{ref} - \frac{C_{LB}^{ref} - C_F}{1 - \exp(-C_{TB}^A h_{TB}/L_{TAL})} \left(1 - \exp(-C_{TB}^A h_{TB}/L_{TAL})\right)$$

Depth is given by:

$$h_{TB} = \left(\frac{h_0(x - x_1) + h_1(x_0 - x)}{x_0 - x_1} + x - x_3 \right) \Lambda_{TB}(-15, x_1)$$

$$+ (x_3 - x) \Lambda_{TB}(-15, x_3) + (x - x_3) \Lambda_{TB}(15, x_3)$$

The following definitions have been used:

$$h_0 = L_{TAL}, \quad h_1 = L_{PST} + L_{DL}, \quad h_3 = 0, \quad h_4 = L_{TAL}$$

The permeability profile is given by:

$$\kappa_{TB} = (\kappa_{PT} - \kappa_{LH}) \Lambda_{TB}(-30, x_2) + \kappa_{LH}$$

Maximum transport rate profile:

$$\begin{aligned}
V_{max} &= \left(1 + PN_{rat}PN_{sc}\Lambda_{TB}(-30, x_2)\right) \times \\
&\quad \times \left(1 + GTB_{rat}(1 - GTB_{sc})\Lambda_{TB}(-30, x_2)\right) V_{max}^{base} \\
V_{max}^{base} &= (V_{max}^{PCT} - V_{max}^{PST})\Lambda_{TB}(-30, x_1) + \\
&\quad + (V_{max}^{PST} - V_{max}^{DL})\Lambda_{TB}(-30, x_2) + \\
&\quad + (V_{max}^{DL} - V_{max}^{TAL})\Lambda_{TB}(-30, x_3) + V_{max}^{TAL}
\end{aligned}$$

Steady state radius profile is approximated by:

$$\begin{aligned}
R_{TB}^{ss} &= R_0^{ss} + (R_2^{ss} - R_0^{ss})\Lambda_{TB}(0.8, x_1) + \\
&\quad + (R_3^{ss} - R_2^{ss})\Lambda_{TB}(28, 0.65x_2 + 0.35x_3) + \\
&\quad + (R_4^{ss} - R_3^{ss})\Lambda_{TB}(3.6, 0.65x_3 + 0.35x_4)
\end{aligned}$$

B.4 Glossary and parameter values

In the following sections, time and space dependence is denoted explicitly. In contrast, dependence only on parameters is not denoted.

B.4.1 Variables

z , position along AA • y , position along GL • x , position along TB • $P_{RA}(t)$, perfusion pressure (i.e. systemic arterial pressure) • P_m , mean arterial pressure • P_p , pulse amplitude reaching AA entrance • f_p , heart rate • $Q_{AA}(t)$, AA volumetric blood flow • $P_D(t)$, AA outflow pressure • $Q_F(t)$, single nephron glomerular filtration rate (SNGFR) • $\Omega_{EA}(t)$, EA vascular resistance • Ω_{EA}^{ref} , reference EA vascular resistance • $R_{EA}(t)$, EA luminal radius • $\mu_{RA}(t)$, RA blood apparent viscosity • $\mu_{AA}(t)$, AA blood apparent viscosity • $\mu_{GL}(t)$, GL blood apparent viscosity • $\mu_{EA}(t)$, EA blood apparent viscosity • $R_{AA}(t, z)$, AA luminal radius • $P_0(t)$, AA inflow pressure • $P_D(t)$, AA outflow pressure • $P_{EA}(t)$, EA blood pressure • P_{EA}^{ref} , reference EA blood

pressure • ξ_{EA} , EA wall tension scaling • Q_{EA}^{ref} , reference EA blood flow • $\Omega_{RA}(t)$, pre-AA vascular resistance • Ω_{AA}^{ref} , reference AA vascular resistance • Ht_{RA} , pre-AA hematocrit • Ht_{AA} , AA hematocrit • Ht_{GL} , GL hematocrit • $Ht_{EA}(t)$, EA hematocrit • L_{TB} , total TB length (also see previous chapter) • $P_{gl}(t)$, GL inflow blood pressure • $Q_{gl}(t)$, GL plasma inflow rate • $P_{GL}(t, y)$, GL blood pressure profile • $Q_{GL}(t, y)$, GL plasma flow profile • $\Delta P_{GL}(t)$, total blood pressure drop along GL • $P_F(t)$, Bowman space hydrostatic pressure • $\pi_{GL}(t, y)$, GL blood colloid osmotic pressure • $P_{TB}(t, x)$, TB fluid pressure • $C_{GL}(t, x)$, GL protein concentration profile • x_0 , site of TB entrance (i.e. beginning of model TB) • x_1 , site of proximal convoluted and straight tubule connection • x_2 , site of proximal straight tubule and loop of Henle connection • x_3 , site of loop bend • x_4 , site of macula densa (i.e. end of model TB) • x_w , site of beginning of loop of Henle water impermeable segment • $\Lambda_{TB}(\cdot, x)$, smoothed step function • $Q_{TB}(t, x)$, TB water flow profile • $R_{TB}(t, x)$, TB luminal radius profile • $C_{TB}(t, x)$, TB Cl^- concentration profile (also see previous chapter) • $\Phi_{TB}(t, x)$, TB water efflux profile • Φ_{PCT} , reference proximal convoluted tubule water efflux • Φ_{PST} , reference proximal straight tubule water efflux • Φ_{DL} , reference descending limb water efflux • $S_{GTB}(t, x)$, glomerotubular balance scaling profile. • $S_{PN}(t, x)$, pressure natriuresis scaling profile • $GTB_{sc}(t)$, glomerotubular balance scaling • $PN_{sc}(t)$, pressure natriuresis scaling • $\Phi_{TB}^{base}(x)$, reference TB water efflux profile • $\alpha_{TB}(x)$, TB compliance profile • $\beta_{TB}(x)$, TB unpressurized radius profile • $P_{MD}(t)$, TB luminal pressure at site of macula densa (i.e. end of model TB) • $P_{DT}(t)$, distal tubule luminal pressure • $R_{TB}^{ss}(x)$, steady-state TB luminal radius • $V_{max}(t, x)$, TB maximum transport rate • $\kappa_{TB}(x)$, TB permeability of Cl^- profile • $C_{TB}^{ext}(x)$, interstitial Cl^- concentration profile • $\Omega_{DT}(t)$, distal tubule resistance • $Q_{MD}(t)$, flow rate at macula densa site (i.e. end of TB) • $h_{TB}(x)$, TB depth profile • h_0 , depth of proximal tubule's entrance • h_1 , depth of proximal convoluted tubule end • $V_{max}^{base}(x)$, TB maximum transport rate reference profile • P_{DT}^{ref} , reference

distal tubule pressure • $P_{AA}(t, z)$, blood pressure profile (also see previous chapter)
 • $C_{MD}(t)$, TB luminal Cl^- concentration at site of macula densa (also see previous chapter).

B.4.2 Parameters

$L_{AA} = 303 \mu\text{m}$, total AA length (also see previous chapter) • $P_{EA, \text{end}} = 0 \text{ mmHg}$, blood pressure at the end of EA (i.e. venous pressure) • $R_{EA}^{\text{ref}} = 10.89 \mu\text{m}$, reference EA luminal radius • $\Omega_{GL} = 0 \text{ mmHg}\cdot\text{min}/\text{nl}$, GL vascular resistance • μ_{RA}^{ref} , reference RA blood apparent viscosity (i.e. at diameter $240 \mu\text{m}$ and hematocrit 0.45) • μ_{AA}^{ref} , reference AA blood apparent viscosity (i.e. at diameter $20 \mu\text{m}$ and hematocrit 0.45) • μ_{GL}^{ref} , reference GL blood apparent viscosity (i.e. at diameter $10 \mu\text{m}$ and hematocrit 0.45) • μ_{EA}^{ref} , reference EA blood apparent viscosity (i.e. at diameter $20 \mu\text{m}$ and hematocrit 0.50) • $w_f^{EA} = 0.10$, EA muscle activation level • $R_{EA}^c = R_{AA}^c$, EA reference luminal radius • $P_{RA}^{\text{ref}} = 100 \text{ mmHg}$, reference perfusion pressure • $Q_{AA}^{\text{ref}} = 280 \text{ nl}/\text{min}$, reference AA blood flow • $R_{AA}^{\text{ref}} = 10.02 \mu\text{m}$, reference AA luminal radius • $Q_F^{\text{ref}} = 30 \text{ nl}/\text{min}$, reference SNGFR • $Ht = 0.45$, systemic hematocrit • $L_{GL} = 1$, GL length • $\tau_{gl} = 0.61 \text{ s}$, GL time constant • $K_f = 2.14 \text{ nl}/(\text{min}\cdot\text{mmHg})$, GL ultrafiltration coefficient • $\Delta P_{GL}^{\text{ref}} = 3 \text{ mmHg}$, reference total GL blood pressure drop • $\alpha_{GL,1} = 1.6290 \text{ mmHg}/(\text{g}/\text{dl})$, first Pappenheimer quadratic coefficient • $\alpha_{GL,2} = 0.2935 \text{ mmHg}/(\text{g}/\text{dl})^2$, second Pappenheimer quadratic coefficient • $C_{gl} = 5.5 \text{ g}/\text{dl}$, GL inflow protein concentration • $L_{PCT} = 0.60 \text{ cm}$, proximal convoluted tubule length • $L_{PST} = 0.25 \text{ cm}$, proximal straight tubule length • $L_{DL} = 0.15 \text{ cm}$, descending limb length • $L_{TAL} = 0.50 \text{ cm}$, thick ascending limb length • $\kappa_{GTB} = 70$, glomerotubular balance efficiency index • $Q_F^\infty = 30 \text{ nl}/\text{min}$, glomerotubular balance target SNGFR (i.e. glomerotubular balance operating point), • $Q_0^{\text{ref}} = 30.0 \text{ nl}/\text{min}$, reference TB flow at proximal tubule entrance • $Q_1^{\text{ref}} = 16.3 \text{ nl}/\text{min}$, reference TB flow at proximal convoluted tubule end • $Q_2^{\text{ref}} = 11.0 \text{ nl}/\text{min}$, reference TB flow at

proximal straight tubule end • $Q_w^{ref} = 7.0$ nl/min, reference TB flow at loop bend
 (i.e. thick ascending limb flow) • $P_{PN,cut} = 80$ mmHg, pressure natriuresis cut-off
 pressure • $P_{PN,base} = 100$ mmHg, reference pressure for natriuresis (i.e. at $PN_{sc} = 0$)
 • $s_{PN} = 0.45$ mmHg⁻¹, sensitivity of pressure natriuresis • $\alpha_{PT} = 0.225$ $\mu\text{m}/\text{mmHg}$,
 proximal tubule compliance • $\alpha_{LH} = 0.133$ $\mu\text{m}/\text{mmHg}$, loop of Henle compliance •
 $\beta_2 = 9.6$ μm , TB luminal radius at end of proximal tubule • $\beta_3 = 5.1$ μm , TB luminal
 radius at loop bend • $\beta_4 = 9.8$ μm , TB luminal radius at end of thick ascending limb
 • $\mu_{TB} = 72$ dyn·s/m², TB luminal fluid viscosity • $s_{DT} = 0.86$ mmHg⁻¹, distal tubule
 compliance sensitivity • $P_{MD}^{ref} = 7$ mmHg, reference macula densa pressure • $Q_{MD}^{ref} =$
 7 nl/min, reference macula densa water flow • $K_M = 70$ mM, TB Michaelis constant
 of Cl⁻ reabsorption • $P_{DT,end} = 2$ mmHg, distal tubule end pressure • $C_F = 115$ mM,
 plasma Cl⁻ concentration • $C_{LB}^{ref} = 275$ mM, loop bend Cl⁻ reference concentration
 • $C_{TB}^A = 2$, interstitial Cl⁻ concentration shape parameter • $\kappa_{PT} = 1$ $\mu\text{m}/\text{s}$, proximal
 tubule Cl⁻ permeability • $\kappa_{LH} = 0.15$ $\mu\text{m}/\text{s}$, loop of Henle Cl⁻ permeability (i.e. thick
 ascending limb entrance) • $V_{max}^{PCT} = 8$ nmol/(cm²·s), reference proximal convoluted
 tubule maximum transport rate • $V_{max}^{PST} = 11.5$ nmol/(cm²·s), reference proximal
 straight maximum transport rate • $V_{max}^{DL} = 0$ nmol/(cm²·s), reference descending limb
 maximum transport rate • $V_{max}^{TAL} = 16.18$ nmol/(cm²·s), reference thick ascending
 limb maximum transport rate • $PN_{rat} = 2$, pressure natriuresis transform parameter
 • $GTB_{rat} = 0.65$, glomerotubular transform parameter • $R_0^{ss} = 11.5$ μm , steady-state
 radius at TB entrance • $R_2^{ss} = 10.4$ μm , steady-state radius at proximal tubule end •
 $R_3^{ss} = 5.4$ μm , steady-state radius at loop bend • $R_4^{ss} = 10.0$ μm , steady-state radius
 at thick ascending limb end • $P_0^{ref} = 95$ mmHg, reference AA inflow pressure (also
 see previous chapter) • $P_D^{ref} = 50$ mmHg, reference AA outflow pressure (also see
 previous chapter) • $\Delta P_0^{ref} = 11$ mmHg, pulse amplitude MR activation correction
 (also see previous chapter).

Appendix C

Complete set of temperature dependent equations

In this chapter, is presented the complete set of equations that model the impact of temperature on the equations that formulate the combined nephrovascular model in its latest form (i.e. Chapter 5). From this description, have been excluded the equations modeling the impact on temperature on blood's oxygen carrying capacity that can be found in Chapter 5.

Temperature effects are modeled by linear curves that are fitted to the available data at temperatures $T_{ref} = 37^{\circ}\text{C}$ (reference temperature) and $T_{hyp} = 28^{\circ}\text{C}$ (hypothermic temperature). In the following, temperature is denoted by T .

- Efferent arteriole muscle activation:

$$w_f^{EA} = w_f^{EA,ref} \left(1 + 0.12 \frac{T - T_{ref}}{T_{hyp} - T_{ref}} \right)$$

- Plasma viscosity:

$$\mu_{plasma} = \mu_{plasma,ref} \left(1 + 0.25 \frac{T - T_{ref}}{T_{hyp} - T_{ref}} \right)$$

- Tubular fluid viscosity:

$$\mu_{TB} = \mu_{TB,ref} \left(1 + 0.90 \frac{T - T_{ref}}{T_{hyp} - T_{ref}} \right)$$

- Smooth muscle Ca²⁺ extrusion rate:

$$k_{Ca} = k_{Ca,ref} \left(1 - 0.20 \frac{T - T_{ref}}{T_{hyp} - T_{ref}} \right)$$

- Ultrafiltration coefficient:

$$K_f = K_{f,ref} \left(1 - 0.05 \frac{T - T_{ref}}{T_{hyp} - T_{ref}} \right)$$

- Glomerotubular balance efficiency index:

$$\kappa_{GTB} = \kappa_{GTB,ref} \left(1 + 0.63 \frac{T - T_{ref}}{T_{hyp} - T_{ref}} \right)$$

Bibliography

- [1] L G Andersson, L E Bratteby, R Ekroth, S Hallhagen, P O Joachimsson, J van der Linden, and O Wesslén. Renal function during cardiopulmonary bypass: influence of pump flow and systemic blood pressure. *Eur J Cardiothorac Surg*, 8(11):597–602, 1994.
- [2] JC Arciero, BE Carlson, and TW Secomb. Theoretical model of metabolic blood flow autoregulation: roles of atp release by red blood cells and conducted responses. *Am J Physiol Heart Circ Physiol*, 295:H1562–H1571, 2008.
- [3] Julia C Arciero, Brian E Carlson, and Timothy W Secomb. Theoretical model of metabolic blood flow regulation: roles of atp release by red blood cells and conducted responses. *Am J Physiol Heart Circ Physiol*, 295(4):H1562–71, Oct 2008.
- [4] W J Arendshorst and C W Gottschalk. Glomerular ultrafiltration dynamics: historical perspective. *Am J Physiol*, 248(2 Pt 2):F163–74, Feb 1985.
- [5] K Aukland, K Heyeraas Tonder, and G Naess. Capillary pressure in deep and superficial glomeruli of the rat kidney. *Acta Physiol Scand*, 101(4):418–27, Dec 1977.
- [6] N Bank and HS Aynedjian. Progressive increases in luminal glucose stimulate proximal sodium absorption in normal and diabetic rats. *J Clin Invest*, 86:309–316, 1990.
- [7] N Bank, P Mower, H S Aynedjian, B M Wilkes, and S Silverman. Sorbinil prevents glomerular hyperperfusion in diabetic rats. *Am J Physiol*, 256(6 Pt 2):F1000–6, Jun 1989.
- [8] Rubin Battino, Timothy R Rettich, and Toshihiro Tominaga. The solubility of oxygen and ozone in liquids. *Journal of physical and chemical reference data*, 12(2):163–178, 1983.

- [9] R Beeuwkes, 3rd. The vascular organization of the kidney. *Annu Rev Physiol*, 42:531–42, 1980.
- [10] William H Beierwaltes, Lisa M Harrison-Bernard, Jennifer C Sullivan, and David L Mattson. Assessment of renal function; clearance, the renal microcirculation, renal blood flow, and metabolic balance. *Compr Physiol*, 3(1):165–200, Jan 2013.
- [11] JL Beny. Electrical coupling between smooth muscle cells and endothelial cells in pig coronary arteries. *Pflügers Arch*, 433:364–367, 1997.
- [12] JL Beny and F Girbi. Dye and electrical coupling of endothelial cells in situ. *Tissue Cell*, 21:797–802, 1989.
- [13] Anil K Bidani, Karen A Griffin, Geoffrey Williamson, Xuemei Wang, and Rodger Loutzenhiser. Protective importance of the myogenic response in the renal circulation. *Hypertension*, 54(2):393–8, Aug 2009.
- [14] B M Brenner, C Baylis, and W M Deen. Transport of molecules across renal glomerular capillaries. *Physiol Rev*, 56(3):502–34, Jul 1976.
- [15] B M Brenner, J L Troy, and T M Daugharty. The dynamics of glomerular ultrafiltration in the rat. *J Clin Invest*, 50(8):1776–80, Aug 1971.
- [16] B M Brenner, J L Troy, and T M Daugharty. Pressures in cortical structures of the rat kidney. *Am J Physiol*, 222(2):246–51, Feb 1972.
- [17] P R Brink. Gap junctions in vascular smooth muscle. *Acta Physiol Scand*, 164(4):349–56, Dec 1998.
- [18] M Broman and O Källskog. The effects of hypothermia on renal function and haemodynamics in the rat. *Acta Physiol Scand*, 153(2):179–84, Feb 1995.
- [19] BE Carlson, JC Arciero, and TW Secomb. Theoretical model of blood flow autoregulation: roles of myogenic, shear-dependent, and metabolic responses. *Am J Physiol Heart Circ Physiol*, 295:H1572–H1579, 2008.
- [20] Brian E Carlson, Julia C Arciero, and Timothy W Secomb. Theoretical model of blood flow autoregulation: roles of myogenic, shear-dependent, and metabolic responses. *Am J Physiol Heart Circ Physiol*, 295(4):H1572–9, Oct 2008.

- [21] Brian E Carlson and Timothy W Secomb. A theoretical model for the myogenic response based on the length-tension characteristics of vascular smooth muscle. *Microcirculation*, 12(4):327–38, Jun 2005.
- [22] P K Carmines, E W Inscho, and R C Gensure. Arterial pressure effects on preglomerular microvasculature of juxtamedullary nephrons. *Am J Physiol*, 258(1 Pt 2):F94–102, Jan 1990.
- [23] P K Carmines, K Ohishi, and H Ikenaga. Functional impairment of renal afferent arteriolar voltage-gated calcium channels in rats with diabetes mellitus. *J Clin Invest*, 98(11):2564–71, Dec 1996.
- [24] D Casellas and L C Moore. Autoregulation and tubuloglomerular feedback in juxtamedullary glomerular arterioles. *Am J Physiol*, 258(3 Pt 2):F660–9, Mar 1990.
- [25] Alejandro R Chade. Renal vascular structure and rarefaction. *Compr Physiol*, 3(2):817–31, Apr 2013.
- [26] J Chen, I Sgouralis, LC Moore, HE Layton, and AT Layton. A mathematical model of the myogenic response to systolic pressure in the afferent arteriole. *Am J Physiol Renal Physiol*, 300:F669–F681, 2011.
- [27] Jing Chen, Ioannis Sgouralis, Leon C Moore, Harold E Layton, and Anita T Layton. A mathematical model of the myogenic response to systolic pressure in the afferent arteriole. *Am J Physiol Renal Physiol*, 300(3):F669–81, Mar 2011.
- [28] Y-M Chen, K-P Yip, DJ Marsh, and N-H Holstein Rathlou. Magnitude of TGF-initiated nephron-nephron interaction is increased in SHR. *Am J Physiol (Renal Fluid Electrolyte Physiol)* 38, 269:F198–F204, 1995.
- [29] KH Chon, R Raghavan, Y-M Chen, DJ Marsh, and K-P Yip. Interactions of TGF-dependent and myogenic oscillations in tubular pressure. *Am J Physiol—Renal Physiol*, 288:F298–F307, 2005.
- [30] C Christoforides and J Hedley-Whyte. Effect of temperature and hemoglobin concentration on solubility of o₂ in blood. *J Appl Physiol*, 27(5):592–6, Nov 1969.
- [31] C Christoforides, L H Laasberg, and J Hedley-Whyte. Effect of temperature on solubility of o₂ in human plasma. *J Appl Physiol*, 26(1):56–60, Jan 1969.

- [32] S Cortell, F J Gennari, M Davidman, W H Bossert, and W B Schwartz. A definition of proximal and distal tubular compliance. practical and theoretical implications. *J Clin Invest*, 52(9):2330–9, Sep 1973.
- [33] W A Cupples. Renal medullary blood flow: its measurement and physiology. *Can J Physiol Pharmacol*, 64(7):873–80, Jul 1986.
- [34] W A Cupples, P Novak, V Novak, and F C Salevsky. Spontaneous blood pressure fluctuations and renal blood flow dynamics. *Am J Physiol*, 270(1 Pt 2):F82–9, Jan 1996.
- [35] W A Cupples, A S Wexler, and D J Marsh. Model of tgf-proximal tubule interactions in renal autoregulation. *Am J Physiol*, 259(4 Pt 2):F715–26, Oct 1990.
- [36] WA Cupples and B Braam. Assessment of renal autoregulation. *Am J Physiol-Renal Physiol*, 292:F1105–F1123, 2007.
- [37] William A Cupples and Branko Braam. Assessment of renal autoregulation. *Am J Physiol Renal Physiol*, 292(4):F1105–23, Apr 2007.
- [38] M J Davis. Myogenic response gradient in an arteriolar network. *Am J Physiol*, 264(6 Pt 2):H2168–79, Jun 1993.
- [39] M J Davis and M A Hill. Signaling mechanisms underlying the vascular myogenic response. *Physiol Rev*, 79(2):387–423, Apr 1999.
- [40] MJ Davis and MA Hill. Signal mechanisms underlying the vascular myogenic response. *Physiol Rev*, 79:387–423, 1999.
- [41] W M Deen, C R Robertson, and B M Brenner. A model of glomerular ultrafiltration in the rat. *Am J Physiol*, 223(5):1178–83, Nov 1972.
- [42] WM Deen, CR Robertson, and BM Brenner. A model of glomerular ultrafiltration in the rat. *Am J Physiol*, 223(5):1178–1183, 1972.
- [43] PF Dillon, MO Askoy, SP Driska, and RA Murphy. Myosin phosphorylation and the cross-bridge cycle in arterial smooth muscle. *Science*, 211:495–497, 1981.
- [44] PF Dillon and RA Murphy. Tonic force maintenance with reduced shortening velocity in arterial smooth muscle. *Am J Physiol*, 242:C102–C108, 1982.

- [45] PB Dobrin. Vascular mechanics. In JT Shepperd, FM Abboud, and SR Geiger, editors, *Handbook of Physiology, Vol III*, pages 65–102. Waverly Press, Baltimore, MD, 1983.
- [46] PB Dobrin and TR Canfield. Identification of smooth muscle series elastic component in intact carotid artery. *Am J Physiol*, 232:H122–H130, 1977.
- [47] SP Driska, DM Damon, and RA Murphy. Estimates of cellular mechanics in arterial smooth muscle. *Biophys J*, 24:525–540, 1978.
- [48] Aurélie Edwards and Thomas L Pallone. Ouabain modulation of cellular calcium stores and signaling. *Am J Physiol Renal Physiol*, 293(5):F1518–32, Nov 2007.
- [49] RM Edwards. Segmental effects of norepinephrine and angiotensin II on isolated renal microvessels. *Am J Physiol (Renal Fluid Electrolyte Physiol 13)*, 244:F526–F534, 1983.
- [50] G Ehrenstein and H Lecar. Electrically gated ionic channels in lipid bilayers. *Q Rev Biophys*, 10:1–34, 1977.
- [51] Roger G Evans, Gabriela A Eppel, Warwick P Anderson, and Kate M Denton. Mechanisms underlying the differential control of blood flow in the renal medulla and cortex. *J Hypertens*, 22(8):1439–51, Aug 2004.
- [52] Roger G Evans, Gerard K Harrop, Jennifer P Ngo, Connie P C Ow, and Paul Michael O’Connor. Basal renal oxygen consumption and the efficiency of oxygen utilization for sodium reabsorption. *Am J Physiol Renal Physiol*, Jan 2014.
- [53] Roger G Evans, Can Ince, Jaap A Joles, David W Smith, Clive N May, Paul M O’Connor, and Bruce S Gardiner. Haemodynamic influences on kidney oxygenation: clinical implications of integrative physiology. *Clin Exp Pharmacol Physiol*, 40(2):106–22, Feb 2013.
- [54] R Feldberg, M Colding-Jørgensen, and N H Holstein-Rathlou. Analysis of interaction between tgf and the myogenic response in renal blood flow autoregulation. *Am J Physiol*, 269(4 Pt 2):F581–93, Oct 1995.
- [55] B Flemming, N Arenz, E Seeliger, T Wronski, K Steer, and P B Persson. Time-dependent autoregulation of renal blood flow in conscious rats. *J Am Soc Nephrol*, 12(11):2253–62, Nov 2001.

- [56] KENICHIRO Fujii, DONALD D Heistad, and FRANK M Faraci. Ionic mechanisms in spontaneous vasomotion of the rat basilar artery in vivo. *The Journal of physiology*, 430(1):389–398, 1990.
- [57] Bruce S Gardiner, David W Smith, Paul M O’Connor, and Roger G Evans. A mathematical model of diffusional shunting of oxygen from arteries to veins in the kidney. *Am J Physiol Renal Physiol*, 300(6):F1339–52, Jun 2011.
- [58] Bruce S Gardiner, Sarah L Thompson, Jennifer P Ngo, David W Smith, Amany Abdelkader, Brad R S Broughton, John F Bertram, and Roger G Evans. Diffusive oxygen shunting between vessels in the preglomerular renal vasculature: anatomic observations and computational modeling. *Am J Physiol Renal Physiol*, 303(5):F605–18, Sep 2012.
- [59] KH Gertz, JA Mangos, G Braun, and HD Paget. On the glomerular tubular balance in the rat kidney. *Pflügers Archiv Eur J Physiol*, 285:360–372, 1965.
- [60] J M Gonzalez-Fernandez and B Ermentrout. On the origin and dynamics of the vasomotion of small arteries. *Math Biosci*, 119(2):127–67, Feb 1994.
- [61] JM Gonzalez-Fernandez and B Ermentrout. On the origin and dynamics of the vasomotion of small arteries. *Math Biosci*, 119:127–167, 1994.
- [62] Karen A Griffin, Rifat Hacıoglu, Isam Abu-Amarah, Rodger Loutzenhiser, Geoffrey A Williamson, and Anil K Bidani. Effects of calcium channel blockers on “dynamic” and “steady-state step” renal autoregulation. *Am J Physiol Renal Physiol*, 286(6):F1136–43, Jun 2004.
- [63] F Gustafsson and N-H Holstein-Rathou. Conducted vasomotor responses in arterioles: characteristics, mechanisms and physiological significance. *Acta Physiol Scand*, 167:11–21, 1999.
- [64] A C Guyton, T G Coleman, and H J Granger. Circulation: overall regulation. *Annu Rev Physiol*, 34:13–46, 1972.
- [65] TP Hannedouche, AG Delgado, DA Gnionsahe, C Boitard, and JP Grünfeld. Renal hemodynamics and segmental tubular sodium reabsorption in early type I diabetes. *Kidney Int*, 37:1126–1133, 1990.
- [66] J He and PK Whelton. Elevated systolic blood pressure and risk of cardiovascular and renal disease: overview of evidence from observational epidemiologic studies and randomized controlled trials. *Am Heart J*, 138:211–219, 1999.

- [67] GD Hirst, FR Edwards, DJ Gould, SL Sandow, and CE Hill. Electrical properties of iridial arterioles of the rat. *Am J Physiol*, 273:H2465–H2472, 1997.
- [68] A L HODGKIN and A F HUXLEY. A quantitative description of membrane current and its application to conduction and excitation in nerve. *J Physiol*, 117(4):500–44, Aug 1952.
- [69] N H Holstein-Rathlou. Synchronization of proximal intratubular pressure oscillations: evidence for interaction between nephrons. *Pflugers Arch*, 408(5):438–43, May 1987.
- [70] N H Holstein-Rathlou. A closed-loop analysis of the tubuloglomerular feedback mechanism. *Am J Physiol*, 261(5 Pt 2):F880–9, Nov 1991.
- [71] N-H Holstein-Rathlou and PP Leyssac. TGF-mediated oscillations in the proximal intratubular pressure: Differences between spontaneously hypertensive rats and Wistar-Kyoto rats. *Acta Physiol Scand*, 126:333–339, 1986.
- [72] N H Holstein-Rathlou and D J Marsh. Oscillations of tubular pressure, flow, and distal chloride concentration in rats. *Am J Physiol*, 256(6 Pt 2):F1007–14, Jun 1989.
- [73] N H Holstein-Rathlou and D J Marsh. Renal blood flow regulation and arterial pressure fluctuations: a case study in nonlinear dynamics. *Physiol Rev*, 74(3):637–81, Jul 1994.
- [74] N-H Holstein-Rathlou and DJ Marsh. Renal blood flow regulation and arterial pressure fluctuations: a case study in nonlinear dynamics. *Physiol Rev*, 74:637–681, 1994.
- [75] NH Holstein-Rathlou and DJ Marsh. Oscillations of tubular pressure, flow, and distal chloride concentration in rats. *American Journal of Physiology-Renal Physiology*, 256(6):F1007–F1014, 1989.
- [76] Niels-Henrik Holstein-Rathlou, Olga V Sosnovtseva, Alexey N Pavlov, William A Cupples, Charlotte Mehlin Sorensen, and Donald J Marsh. Nephron blood flow dynamics measured by laser speckle contrast imaging. *Am J Physiol Renal Physiol*, 300(2):F319–29, Feb 2011.
- [77] A Horowitz, C B Menice, R Laporte, and K G Morgan. Mechanisms of smooth muscle contraction. *Physiol Rev*, 76(4):967–1003, Oct 1996.

- [78] R E Huss, D J Marsh, and R E Kalaba. Two models of glomerular filtration rate and renal blood flow in the rat. *Ann Biomed Eng*, 3(1):72–99, Mar 1975.
- [79] A Just. Mechanisms of renal blood flow autoregulation: dynamics and contributions. *Am J Physiol Regul Integr Comp Physiol*, 292:R1–17, 2007.
- [80] A Just and WJ Arendshorst. Dynamics and contribution of mechanisms mediating renal blood flow autoregulation. *Am J Physiol Regul Integr Comp Physiol*, 285:R619–R631, 2002.
- [81] A Just, H Ehmke, L Toktomambetova, and HR Kirchheim. Dynamic characteristics and underlying mechanisms of renal blood flow autoregulation in the conscious dog. *Am J Physiol Renal Physiol*, 280:F1062–F1071, 2001.
- [82] Armin Just. Mechanisms of renal blood flow autoregulation: dynamics and contributions. *Am J Physiol Regul Integr Comp Physiol*, 292(1):R1–17, Jan 2007.
- [83] O Källskog, L O Lindbom, H R Ulfendahl, and M Wolgast. Kinetics of the glomerular ultrafiltration in the rat kidney. a theoretical study. *Acta Physiol Scand*, 95(2):191–200, Oct 1975.
- [84] KE Kamm and JT Stull. The function of myosin and myosin light chain kinase phosphorylation in smooth muscle. *Ann Rev Pharmacol Toxicol*, 25:593–620, 1985.
- [85] Keyvan Karkouti, Duminda N Wijeysondera, Terrence M Yau, Jeannie L Calum, Davy C Cheng, Mark Crowther, Jean-Yves Dupuis, Stephen E Fremes, Blaine Kent, Claude Laflamme, Andre Lamy, Jean-Francois Legare, C David Mazer, Stuart A McCluskey, Fraser D Rubens, Corey Sawchuk, and W Scott Beattie. Acute kidney injury after cardiac surgery: focus on modifiable risk factors. *Circulation*, 119(4):495–502, Feb 2009.
- [86] Hiroyuki Kobori, Masaomi Nangaku, L Gabriel Navar, and Akira Nishiyama. The intrarenal renin-angiotensin system: from physiology to the pathobiology of hypertension and kidney disease. *Pharmacol Rev*, 59(3):251–87, Sep 2007.
- [87] W Kriz. Structural organization of the renal medulla: comparative and functional aspects. *Am J Physiol*, 241(1):R3–16, Jul 1981.
- [88] W Kriz and L Bankir. A standard nomenclature for structures of the kidney. the renal commission of the international union of physiological sciences (iups). *Kidney Int*, 33(1):1–7, Jan 1988.

- [89] A Krogh, GA Harrop, and P Brandt-Rehberg. Studies on the physiology of capillaries III. The innervation of the blood vessels in the hind legs of the frog. *J Physiol (London)*, 56:179–189, 1922.
- [90] Anita T Layton, Philip Pham, and Hwa-Yeon Ryu. Signal transduction in a compliant short loop of henle. *Int j numer method biomed eng*, 28(3):369–383, Mar 2012.
- [91] AT Layton. Feedback-mediated dynamics in a model of a compliant thick ascending limb. *Math Biosci*, 228:185–194, 2010.
- [92] AT Layton, LC Moore, and HE Layton. Tubuloglomerular feedback signal transduction in a compliant thick ascending limb. *Am J Physiol Renal Physiol*, submitted, 2009.
- [93] AT Layton, P Pham, and H Ryu. Signal transduction in a compliant short loop of Henle. *Int J Numer Methods Biomed Eng*, 28(3):369–380, 2012.
- [94] H E Layton, E B Pitman, and L C Moore. Bifurcation analysis of tgf-mediated oscillations in sngfr. *Am J Physiol*, 261(5 Pt 2):F904–19, Nov 1991.
- [95] H E Layton, E B Pitman, and L C Moore. Instantaneous and steady-state gains in the tubuloglomerular feedback system. *Am J Physiol*, 268(1 Pt 2):F163–74, Jan 1995.
- [96] H Lecar, G Ehrenstein, and R Latorre. Mechanism for channel gating in excitable bilayers. *Ann NY Acad Sci*, 264:304–313, 1975.
- [97] PP Leyssac and NH Holstein-Rathlou. Effects of various transport inhibitors on oscillating tgf pressure responses in the rat. *Pflügers Archiv European Journal of Physiology*, 407(3):285–291, 1986.
- [98] Y Li, I Sgouralis, and AT Layton. Computing viscous flow in an elastic tube. *Numer Math* submitted, 2013.
- [99] Hyun-Jung Lim, Yong-Jin Lee, Jeong-Hun Nam, Seok Chung, and Sehyun Shin. Temperature-dependent threshold shear stress of red blood cell aggregation. *J Biomech*, 43(3):546–50, Feb 2010.
- [100] TL Little, J Xia, and BR Duling. Dye tracers define differential endothelial and smooth muscle coupling patterns within the arteriolar wall. *Circ Res*, 76:498–504, 1995.

- [101] K Loutzenhiser and R Loutzenhiser. Angiotensin ii-induced $ca(2+)$ influx in renal afferent and efferent arterioles: differing roles of voltage-gated and store-operated $ca(2+)$ entry. *Circ Res*, 87(7):551–7, Sep 2000.
- [102] Kathy Loutzenhiser and Rodger Loutzenhiser. Angiotensin ii-induced $ca2+$ influx in renal afferent and efferent arterioles differing roles of voltage-gated and store-operated $ca2+$ entry. *Circulation research*, 87(7):551–557, 2000.
- [103] R Loutzenhiser, A Bidani, and L Chilton. Renal myogenic response: kinetic attributes and physiologic role. *Circ Res*, 90:1316–1324, 2002.
- [104] R Loutzenhiser, A Bidani, and X Wang. Systolic pressure and the myogenic response of the renal afferent arteriole. *Acta Physiol Scand*, 181:404–413, 2004.
- [105] R Loutzenhiser, A K Bidani, and X Wang. Systolic pressure and the myogenic response of the renal afferent arteriole. *Acta Physiol Scand*, 181(4):407–13, Aug 2004.
- [106] Rodger Loutzenhiser, Anil Bidani, and Lisa Chilton. Renal myogenic response: kinetic attributes and physiological role. *Circ Res*, 90(12):1316–24, Jun 2002.
- [107] Rodger Loutzenhiser, Karen Griffin, Geoffrey Williamson, and Anil Bidani. Renal autoregulation: new perspectives regarding the protective and regulatory roles of the underlying mechanisms. *Am J Physiol Regul Integr Comp Physiol*, 290(5):R1153–67, May 2006.
- [108] Rodger Loutzenhiser, Karen Griffin, Geoffrey Williamson, and Anil Bidani. Renal autoregulation: new perspectives regarding the protective and regulatory roles of the underlying mechanisms. *American Journal of Physiology-Regulatory, Integrative and Comparative Physiology*, 290(5):R1153–R1167, 2006.
- [109] DJ Lush and JCS Fray. Steady-state autoregulation of renal blood flow: a myogenic model. *Am J Physiol Reg Int Comp Physiol*, 247:R89–R99, 1984.
- [110] David A Maddox, William M Deen, and Barry M Brenner. Glomerular filtration. *Comprehensive Physiology*, 1992.
- [111] C M Mangano, L S Diamondstone, J G Ramsay, A Aggarwal, A Herskowitz, and D T Mangano. Renal dysfunction after myocardial revascularization: risk factors, adverse outcomes, and hospital resource utilization. the multicenter study of perioperative ischemia research group. *Ann Intern Med*, 128(3):194–203, Feb 1998.

- [112] DJ Marsh, OV Sosnovtseva, KH Chon, and N-H Holstein-Rathlou. Nonlinear interactions in renal blood flow regulation. *Am J Physiol Regul Integr Comp Physiol*, 288:R1143–R1159, 2005.
- [113] Donald J Marsh, Olga V Sosnovtseva, Ki H Chon, and Niels-Henrik Holstein-Rathlou. Nonlinear interactions in renal blood flow regulation. *Am J Physiol Regul Integr Comp Physiol*, 288(5):R1143–59, May 2005.
- [114] Donald J Marsh, Olga V Sosnovtseva, Alexey N Pavlov, Kay-Pong Yip, and Niels-Henrik Holstein-Rathlou. Frequency encoding in renal blood flow regulation. *Am J Physiol Regul Integr Comp Physiol*, 288(5):R1160–7, May 2005.
- [115] Donald J Marsh, Ildiko Toma, Olga V Sosnovtseva, Janos Peti-Peterdi, and Niels-Henrik Holstein-Rathlou. Electrotonic vascular signal conduction and nephron synchronization. *Am J Physiol Renal Physiol*, 296(4):F751–61, Apr 2009.
- [116] David L Mattson. Importance of the renal medullary circulation in the control of sodium excretion and blood pressure. *Am J Physiol Regul Integr Comp Physiol*, 284(1):R13–27, Jan 2003.
- [117] G A Meininger and M J Davis. Cellular mechanisms involved in the vascular myogenic response. *Am J Physiol*, 263(3 Pt 2):H647–59, Sep 1992.
- [118] F Mekata. Current spread in the smooth muscle of the rabbit aorta. *Am J Physiol*, 272:143–155, 1974.
- [119] D Mink, A Schiller, W Kriz, and R Taugner. Interendothelial junctions in kidney vessels. *Cell Tissue Res*, 236:567–576, 1984.
- [120] L C Moore, A Rich, and D Casellas. Ascending myogenic autoregulation: interactions between tubuloglomerular feedback and myogenic mechanisms. *Bull Math Biol*, 56(3):391–410, May 1994.
- [121] Leon C Moore, Adam Rich, and Daniel Casellas. Ascending myogenic autoregulation: interactions between tubuloglomerular feedback and myogenic mechanisms. *Bulletin of mathematical biology*, 56(3):391–410, 1994.
- [122] C Morris and H Lecar. Voltage oscillations in the barnacle giant muscle fiber. *Biophys J*, 35:193–213, 1981.
- [123] C Morris and H Lecar. Voltage oscillations in the barnacle giant muscle fiber. *Biophys J*, 35(1):193–213, Jul 1981.

- [124] RA Murphy. Mechanics of vascular smooth muscles. In DF Bohr, AT Somlyo, HV Sparks Jr, and SR Geiger, editors, *Handbook of Physiology, Vol II*, pages 325–442. Waverly Press, Baltimore, MD, 1980.
- [125] RA Murphy. Muscle cells of hollow organs. *News Physiol Sci*, 3:124–128, 1988.
- [126] L G Navar. Renal autoregulation: perspectives from whole kidney and single nephron studies. *Am J Physiol*, 234(5):F357–70, May 1978.
- [127] David A Nordsletten, Shane Blackett, Michael D Bentley, Erik L Ritman, and Nicolas P Smith. Structural morphology of renal vasculature. *Am J Physiol Heart Circ Physiol*, 291(1):H296–309, Jul 2006.
- [128] J R Nyengaard. Number and dimensions of rat glomerular capillaries in normal development and after nephrectomy. *Kidney Int*, 43(5):1049–57, May 1993.
- [129] GEORGE Osol and WILLIAM Halpern. Spontaneous vasomotion in pressurized cerebral arteries from genetically hypertensive rats. *American Journal of Physiology-Heart and Circulatory Physiology*, 254(1):H28–H33, 1988.
- [130] Thomas L Pallone, Aurélie Edwards, and David L Mattson. Renal medullary circulation. *Compr Physiol*, 2(1):97–140, Jan 2012.
- [131] A S Popel. Theory of oxygen transport to tissue. *Crit Rev Biomed Eng*, 17(3):257–321, 1989.
- [132] A R Pries, D Neuhaus, and P Gaehtgens. Blood viscosity in tube flow: dependence on diameter and hematocrit. *Am J Physiol*, 263(6 Pt 2):H1770–8, Dec 1992.
- [133] A R Pries and T W Secomb. Rheology of the microcirculation. *Clin Hemorheol Microcirc*, 29(3-4):143–8, 2003.
- [134] A R Pries, T W Secomb, T Gessner, M B Sperandio, J F Gross, and P Gaehtgens. Resistance to blood flow in microvessels in vivo. *Circ Res*, 75(5):904–15, Nov 1994.
- [135] R Raghavan, X Chen, K-P Yip, DJ Marsh, and KH Chon. Interactions between TGF-dependent and myogenic oscillations in tubular pressure and whole kidney blood flow in both SDR and SHR. *Am J Physiol Renal Physiol*, 290:F720–F732, 2006.

- [136] CM Rembold and RA Murphy. Latch-bridge model in smooth muscle: $[Ca^{2+}]_i$ can quantitatively predict stress. *Am J Physiol*, 259:C251–C237, 1990.
- [137] Y Ren, J L Garvin, R Liu, and O A Carretero. Crosstalk between the connecting tubule and the afferent arteriole regulates renal microcirculation. *Kidney Int*, 71(11):1116–21, Jun 2007.
- [138] R J Roman, D L Mattson, and A W Cowley, Jr. Measurement of regional blood flow in the kidney using laser-doppler flowmetry. *Methods Mol Med*, 51:407–26, 2001.
- [139] Mitchell H Rosner, Didier Portilla, and Mark D Okusa. Cardiac surgery as a cause of acute kidney injury: pathogenesis and potential therapies. *J Intensive Care Med*, 23(1):3–18, 2008.
- [140] M Samaja, D Melotti, E Rovida, and L Rossi-Bernardi. Effect of temperature on the p50 value for human blood. *Clin Chem*, 29(1):110–4, Jan 1983.
- [141] J Schnermann and JP Briggs. Function of the juxtaglomerular apparatus: Control of glomerular hemodynamics and renin secretion. In Alpern RJ and Hebert SC, editors, *Seldin and Giebisch's The Kidney: Physiology and Pathophysiology*, pages 589–626. Elsevier Academic Press, Amsterdam; Boston, 4th edition, 2008.
- [142] SS Segal and JL Beny. Intracellular recording and dye transfer in arterioles during blood flow control. *Am J Physiol*, 264:H1–H7, 1992.
- [143] SS Segal and BR Duling. Conduction of vasomotor responses in arterioles: a role for cell-to-cell coupling? *Am J Physiol*, 256:H838–H845, 1989.
- [144] I Sgouralis and AT Layton. Autoregulation and conduction of vasomotor responses in a mathematical model of the rat afferent arteriole. *Am J Physiol Renal Physiol* (*in press*), 2012.
- [145] Ioannis Sgouralis and Anita T Layton. Autoregulation and conduction of vasomotor responses in a mathematical model of the rat afferent arteriole. *Am J Physiol Renal Physiol*, 303(2):F229–39, Jul 2012.
- [146] Ioannis Sgouralis and Anita T Layton. Control and modulation of fluid flow in the rat kidney. *Bull Math Biol*, Oct 2013.
- [147] Ioannis Sgouralis and Anita T Layton. Theoretical assessment of renal autoregulatory mechanisms. *Am J Physiol Renal Physiol* submitted, 2013.

- [148] R E Shipley and R S Study. Changes in renal blood flow, extraction of inulin, glomerular filtration rate, tissue pressure and urine flow with acute alterations of renal artery blood pressure. *Am J Physiol*, 167(3):676–88, Dec 1951.
- [149] G Siegel, BJ Ebeling, HW Hofer, J Nolte, H Roedel, and D Klubendorf. Vascular smooth muscle rhythmicity. *Mechanisms of blood pressure waves*, pages 319–338, 1984.
- [150] K L Siu, B Sung, W A Cupples, L C Moore, and K H Chon. Detection of low-frequency oscillations in renal blood flow. *Am J Physiol Renal Physiol*, 297(1):F155–62, Jul 2009.
- [151] KL Siu, B Sung, WA Cupples, LC Moore, and KH Chon. Detection of low-frequency oscillations in renal blood flow. *Am J Physiol Renal Physiol*, 297:F155–F162, 2009.
- [152] JA Sosa-Melgarejo and CL Berry. Effects of hypertension on the intercellular contacts between smooth muscle cells in the rat thoracic aorta. *J Hypertension*, 9:475–480, 1991.
- [153] Alfred H Stammers, See N Vang, Brian L Mejak, and Eric D Rauch. Quantification of the effect of altering hematocrit and temperature on blood viscosity. *J Extra Corpor Technol*, 35(2):143–51, Jun 2003.
- [154] M Steinhausen, K Endlich, R Nobiling, N Parekh, and F Schütt. Electrically induced vasomotor responses and their propagation in rat renal vessels in vivo. *J Physiol*, 505 (Pt 2):493–501, Dec 1997.
- [155] M Steinhausen, K Endlich, R Nobiling, N Rarekh, and F Schütt. Electrically induced vasomotor responses and their propagation in rat renal vessels in vivo. *J Physiol*, 505:493–501, 1997.
- [156] S C Thomson, A Deng, D Bao, J Satriano, R C Blantz, and V Vallon. Ornithine decarboxylase, kidney size, and the tubular hypothesis of glomerular hyperfiltration in experimental diabetes. *J Clin Invest*, 107(2):217–24, Jan 2001.
- [157] S C Thomson, V Vallon, and R C Blantz. Resetting protects efficiency of tubuloglomerular feedback. *Kidney Int Suppl*, 67:S65–70, Sep 1998.
- [158] Scott C Thomson and Roland C Blantz. Glomerulotubular balance, tubuloglomerular feedback, and salt homeostasis. *J Am Soc Nephrol*, 19(12):2272–5, Dec 2008.

- [159] Scott C Thomson and Roland C Blantz. Biophysics of glomerular filtration. *Compr Physiol*, 2(3):1671–99, Jul 2012.
- [160] K Thureau and K Kramer. Weitere Untersuchungen zur myogenic Natur der Autoregulation des Nierenkreislaufes. *Pflügers Arch.*, 269:77–93, 1959.
- [161] V Vallon. The proximal tubule in the pathophysiology of the diabetic kidney. *Am J Physiol Regul Integr Comp Physiol*, 300:R1009–R1022, 1996.
- [162] V Vallon, R C Blantz, and S Thomson. Homeostatic efficiency of tubuloglomerular feedback is reduced in established diabetes mellitus in rats. *Am J Physiol*, 269(6 Pt 2):F876–83, Dec 1995.
- [163] Volker Vallon and Scott C Thomson. Renal function in diabetic disease models: the tubular system in the pathophysiology of the diabetic kidney. *Annu Rev Physiol*, 74:351–75, 2012.
- [164] R P van Dokkum, C W Sun, A P Provoost, H J Jacob, and R J Roman. Altered renal hemodynamics and impaired myogenic responses in the fawn-hooded rat. *Am J Physiol*, 276(3 Pt 2):R855–63, Mar 1999.
- [165] AJ Wagner, N-H Holstein-Rathou, and DJ Marsh. Internephron coupling by conducted vasomotor responses in normotensive and spontaneously hypertensive rats. *Am J Physiol (Renal Physiol 41)*, 272:F372–F379, 1997.
- [166] Xuemei Wang, Rodger D Loutzenhiser, and William A Cupples. Frequency modulation of renal myogenic autoregulation by perfusion pressure. *Am J Physiol Regul Integr Comp Physiol*, 293(3):R1199–204, Sep 2007.
- [167] DG Welsh and SS Segal. Endothelial and smooth muscle cell conduction in arterioles controlling blood flow. *Am J Physiol*, 274:H178–H186, 1998.
- [168] GA Williamson, R Loutzenhiser, X Wang, K Griffin, and AK Bidani. Systolic and mean blood pressures and afferent arteriolar myogenic response dynamics: a modeling approach. *Am J Physiol Regul Integr Comp Physiol*, 295:R1502–R1511, 2008.
- [169] Geoffrey A Williamson, Rodger Loutzenhiser, Xuemei Wang, Karen Griffin, and Anil K Bidani. Systolic and mean blood pressures and afferent arteriolar myogenic response dynamics: a modeling approach. *Am J Physiol Regul Integr Comp Physiol*, 295(5):R1502–11, Nov 2008.

- [170] U Wittmann, B Nafz, H Ehmke, H R Kirchheim, and P B Persson. Frequency domain of renal autoregulation in the conscious dog. *Am J Physiol*, 269(3 Pt 2):F317–22, Sep 1995.
- [171] J Xia and BR Duling. Electromechanical coupling and the conducted vasomotor response. *Am J Physiol*, 269:H2022–H2030, 1995.
- [172] J Xia, TL Little, and BR Duling. Cellular pathways of the conducted electrical response in arterioles of hamster cheek pouch in vitro. *Am J Physiol*, 269:H2031–H2038, 1995.
- [173] K-P Yip, N-H Holstein-Rathlou, and DJ Marsh. Chaos in blood flow control in genetic and renovascular hypertensive rats. *Am J Physiol (Renal Fluid Electrolyte Physiol 30)*, 261:F400–F408, 1991.
- [174] B Zimmerhackl, R Dussel, and M Steinhausen. Erythrocyte flow and dynamic hematocrit in the renal papilla of the rat. *Am J Physiol*, 249(6 Pt 2):F898–902, Dec 1985.

Biography

Ioannis Sgouralis was born in 1986 in Kalampaka, Greece. He attended the School of Applied Mathematical and Physical Sciences at the National Technical University of Athens, Athens, Greece. He graduated in 2009 with a Diploma in Applied Mathematics, with a major in Applied Analysis and Engineering. He completed his diploma thesis in the Department of Mathematics under the supervision of Professor Drossos Gintides. Ioannis Sgouralis joined the Graduate School of Duke University, Durham, North Carolina, United States of America in 2009, and received a Master of Science in Mathematics in 2011. Ioannis Sgouralis received the Doctor of Philosophy from the Department of Mathematics of Duke University in 2014. His research, conducted under the supervision of Professor Anita T. Layton, is in the area of Mathematical Physiology.